Master's thesis

NTNU
Norwegian University of Science and Technology
Faculty of Natural Sciences
Department of Physics

Erlend Hektoen Johansen

Modeling, calibration and aberration correction for Fourier Ptychography within the paraxial approximation

Master's thesis in Nanotechnology
Supervisor: Dag Werner Breiby
June 2024

NTNU
Norwegian University of
Science and Technology

Erlend Hektoen Johansen

Modeling, calibration and aberration correction for Fourier Ptychography within the paraxial approximation

Master's thesis in Nanotechnology
Supervisor: Dag Werner Breiby
June 2024

Norwegian University of Science and Technology
Faculty of Natural Sciences
Department of Physics

NTNU
Norwegian University of
Science and Technology

ABSTRACT

Fourier Ptychography (FP) is a method of computationally enhanced microscopy based on iterative recovery of the Fourier spectrum of a complex sample, from a number of low-resolution intensity images obtained using a standard light microscope under coherent illumination at varying angles. Through FP, the benefits of a large field of view and depth of field obtained by using a low magnification microscope objective may be maintained, while simultaneously allowing for increased resolution and quantitative phase recovery. For optimal recovery within the FP framework, the correctness of the underlying diffraction model used during recovery is important. The main contributions in this thesis are the derivation of a generalized imaging model based on paraxial optics, the proposal of a system calibration scheme based on the origin of the bright-field region within the derived imaging model and an initial investigation into the detrimental effects of imaging through a window. In the derived imaging model, the placement of the defining aperture of the system was used to define an effective object to aperture distance. Based on this value, the appearance of a variable quadratic phase term at the object plane and a spatial variation of the frequency shift under angled illumination was derived. Upon imaging through a window, it was found that using a high numerical aperture objective results in severe aberrations. To avoid the aberrations, a low numerical aperture objective must be used, playing into the strengths of FP.

SAMMENDRAG

Fourierptykografi (FP) er en metode for numerisk forbedret mikroskopi basert på iterativ rekonstruksjon av Fourier spekteret til en kompleks prøve, fra et antall lavoppløste intensitet bilder tatt med et vanlig lys mikroskop under koherent belysning med variable vinkel. Gjennom FP, beholder man fordelene av et stort synsfelt og stor dybdeskarphet fra bruken av et mikroskop objektiv med lav forstørrelse, samtidig som det er mulig å oppnå økt oppløsning og kvantitativ fase-rekonstruksjon. For optimal rekonstruksjon innenfor FP rammeverket, er korrektheten til den underliggende avbildningsmodellen som benyttes under rekonstruksjonen viktig. De hovedbidragene i denne oppgaven er utledningen av en generell avbildningsmodell basert på paraksial optikk, presentasjonen av en kalibreringsprosedyre basert på opprinnelsen av direktelys regionen i den utledede modellen og en innledende undersøkelse av de negative konsekvensene ved å avbilde gjennom et vindu. I den utledede avbildningsmodellen, benyttes plasseringen av den definerende blenderåpningen i et linsesystem til å definere en effektiv avstand fra objektet til blenderåpningen. Basert på denne verdien, utledes behovet for å inkludere et kvadratisk fase-ledd i objekt planet, samtidig som frekvens skiftet under vinklet belysning blir posisjons avhengig. Ved avbildning gjennom et vindu, ble det demonstrert at bruken av et objektiv med høy numerisk aperture resulterer i kraftige aberrasjoner. For å unngå disse aberrasjonene, må et objektiv med lav numerisk aperture benyttes, hvilket samsvarer med styrkene til FP.

PREFACE

This thesis was written by the author as the cap stone of the five-year master's program in Nanotechnology at NTNU. Under the supervision and guidance of professor Dag Werner Breiby, I have spent the last year delving into the field of applied optics, first through a project this fall, and while working on this thesis over the last five months. As the thesis is probably long enough, the reader will be expected to have a general understanding of mathematics at the university level and a basic understanding of optics and optical microscopes. In particular, I am grateful to Prof. Breiby for the discussions we have had throughout the last year, for offering the project which resulted in this thesis and for allowing me the independence to investigate the nuances of Fourier Ptychography and paraxial imaging at my own pace, and while delving into an untold number of rabbit holes along the way. Further, I would like to thank Muhammed Nadeem Akram for his helpful explanations and suggestions in the initial phases of this thesis. Finally, I would like to thank my fellow nanotechnology students, whom I have shared these last five years as a student with, for fostering and maintaining my joy of learning throughout my stay at NTNU.

CONTENTS

LIST OF FIGURES

LIST OF TABLES

ABBREVIATIONS

AS Aperture Stop

BF Bright-Field

DF Dark-Field

DoF Depth of Field

EnP Entrance Pupil

EPRY Embedded Pupil Function Recovery

FoV Field of View

FP Fourier Ptychography

LED Light-Emitting Diode

NA Numerical Aperture

NBFL Non-linear Bright-Field Localization

PSO Particle Swarm Optimization

R&D Results and Discussion

RANSAC Random Sample Consensus

CHAPTER 1

INTRODUCTION

The concept of Fourier Ptychography (FP) was proposed in 2013 by Zheng et al.[1], demonstrating a method of computationally enhanced microscopy through iterative recovery of the Fourier spectrum of a complex sample, based on a number of low-resolution intensity images obtained using a standard light microscope while varying the angle of the sample illumination. Through FP, the benefits of a large Field of View (FoV) and Depth of Field (DoF) obtained by using a low magnification microscope objective may be maintained, while simultaneously allowing for increased resolution and quantitative phase recovery. During the 10 years since its introduction, the technique has been further enhanced to allow for correction of lens aberrations[2] and three-dimensional imaging, among numerous other improvements[3]. To date, FP shows great promise as a technique for a multitude of applications, including but not limited to, quantitative phase imaging in 2D and 3D, digital pathology and cytometry, aberration metrology, surface inspection, long-range imaging and x-ray nanoscopy[3].

In the initial article proposing the concept of FP by Zheng et al.[1], three simplifications are stated in terms of the imaging model. First, the LED illumination is modelled as coherent and oblique plane waves. Second, the illumination of the complex object o by an oblique plane wave is assumed to be equivalent to a shift $\boldsymbol{f_i}$ of the sample spectrum S in the Fourier domain, originating from application of the Fourier shift theorem. Third, the lens is assumed to filter the shifted sample spectrum through multiplication by a circular pupil, $\mathcal{P}$. Disregarding the magnification of the system, these assumptions yield an imaging model where the intensity I_i at the detector under illumination by the i-th LED is given by the relation

$$I_i(\boldsymbol{r}) = |\mathcal{F}\left\{\mathcal{P}(\boldsymbol{f})S(\boldsymbol{f}-\boldsymbol{f_i})\right\}|^2, \tag{1.1}$$

where the sample spectrum equals the Fourier transform of the complex object as given by

$$S(\boldsymbol{f}) = \mathcal{F}\left\{o(\boldsymbol{r})\right\} \tag{1.2}$$

for spatial coordinates $\boldsymbol{r}$ and spatial frequencies $\boldsymbol{f}$. To achieve the inverse of Equation 1.1 and recover the sample spectrum based on captured intensity images I_i^c, FP relies on iterative phase retrieval[1]. This process is based on the idea that for the recovered spectrum $S_r(\boldsymbol{f})$, the imaging procedure in Equation 1.1 should produce the same intensity images as those that were captured, while an overlap of the intensity images in terms of their frequency content allows for the phase to be recovered.

Improvements upon this model, accounting for the spherical nature of the LED illumination and the derived behavior of a single, thin lens system within the paraxial approximation, have previously been considered by Konda[4] and others[5, 6]. However, the preceding project[7] conducted by the author showed that the resulting thin lens model works poorly for systems where the original assumptions made by Zheng[1] appear to be upheld. Further, the existence of systems adhering to neither of the two models was observed.

Four goals will be pursued throughout this thesis. The first goal will be to develop a generalized imaging model within the confines of the paraxial approximation, consisting of two lenses and a defining aperture, which should be applicable to a wider span of imaging systems than the existing models. The second goal will be to develop a calibration scheme from which any inaccuracies in the model parameters may be corrected for. A secondary purpose for this calibration scheme will additionally be to verify the validity of the generalized model, and illustrate whether use of the generalized model allows for better recovery quality. The third goal will be to investigate the complications of imaging through a sapphire glass window and the ability of FP to correct for said complications. If sufficient correction is achieved, this investigation may open up the door to a number of novel FP based experiments. For instance, it would be possible to use FP to image into a controlled environment, such as a vacuumized or pressurized container. Finally, the fourth goal will be to investigate whether it is possible to perform FP with a camera objective, as compared to the specially designed microscope objectives and single-lens systems which have been considered in previous works.

To this extent, chapter 2, chapter 3 and chapter 4 will provide the theoretical foundation for the remainder of the project, including the derivation of a generalized imaging model within the confines of paraxial optics, an overview of the algorithms and experimental considerations necessary to perform state-of-the-art 2D FP recovery and an introduction to aberration theory. In chapter 5, a novel calibration scheme based on a derived expression for the origin of the Bright-Field (BF) region will be presented. Subsequently, chapter 6 and chapter 7 will respectively describe the experimental implementation and procedures used to obtain the results of this work, which will be displayed and discussed in chapter 8, chapter 9 and chapter 10. Finally, chapter 11 will cover the conclusions that may be drawn from this thesis and how it may be used to guide future work.

1.1 Disclosures

It should be noted that this thesis is a direct continuation of a preparatory project conducted this previous fall as part of the NTNU course "TFY4520 Nanotechnology, Specialization Project". As such, certain parts of the project thesis[7] submitted at the end of that project have been reused in this work. Some sections are reused with minimal changes, while others have been heavily modified to be consistent with the derivations and experimental work performed in this thesis. Affected sections include parts of the abstract, the first two paragraphs of the introduction, parts of the theory and the experimental implementation, and the entirety of Appendix C. In chapter 2, this is the case for most of section 2.1 and section 2.3 up to and including subsection 2.3.1. Most of chapter 3 is reused from the preparatory project with minor modifications, except for section 3.5 and section 3.9. Finally, most of chapter 6 is reused with minor changes corresponding to various modifications of the microscope setup and the implementation of the recovery algorithm, with the exception of subsubsection 6.3.1.3 and subsection 6.3.2.

All figures in this thesis were either made in Inkscape or Matplotlib, or, in a few cases, reused from other works. The reused figures are licensed under various Creative Commons licenses as referenced in the figure texts, with one exception for which written permission was obtained.

CHAPTER 2

DERIVATION OF GENERALIZED IMAGING MODEL

In the following chapter, we shall derive a generalized, theoretical model for the image formation process within a FP microscope. The imaging system considered in FP consists of four main components: a LED array providing variable-angle illumination, a sample, a detector, and a lens system with a defining aperture, which will be referred to as the Aperture Stop (AS). Moving beyond the simplifications made by Zheng[1] covered in the introduction, later works[4, 5, 6] have considered the necessary modifications to account for spherical illumination and derived the paraxial behavior of a thin lens system, consisting of a single lens located in the same plane as the AS. In addition to the results for the thin lens system, the generalized model derived in this work will consider how the position of the AS affects single- and two-lens systems. Using the theoretical foundation presented in section 2.1, the properties of four idealized lens systems will be generalized in section 2.2 followed by a wave-optical derivation of the impact of angled illumination in section 2.3. Further, the impact of discretization, as is necessary for computational treatment, will be considered in section 2.4. Finally, section 2.5 will place the contributions made in this chapter within the context of previous works. In general, the derivations will be rooted in the field of Fourier optics as covered by Goodman in "Introduction to Fourier Optics"[8].

2.1 Wave optical foundation of the imaging process

In the following section, the necessary theoretical foundation for the further derivations will be covered. This includes a description of wave propagation between two parallel planes in the Fresnel approximation and the transmission models which will be used to describe the lenses and apertures.

The discussion will be limited to the scalar theory of monochromatic, optical waves. As such, the waves will be described interchangeably by their frequency f, wavelength $\lambda = c/f$ and wavenumber $k = 2\pi/\lambda$, while the optical wavefield for a point $\boldsymbol{r}$ at a time t is described by[8, p.50]

$$u(\boldsymbol{r}, t) = \mathrm{Re}\{U(\boldsymbol{r}) \exp[-i2\pi f t]\} \tag{2.1}$$

where $U(\boldsymbol{r})$ is the complex wavefield which will be considered further. Notably, upon imaging only the intensity[8, p.77]

$$I(\boldsymbol{r}) = |U(\boldsymbol{r})|^2 \tag{2.2}$$

is measured, resulting in a loss of information about the phase.

2.1.1 Wave propagation in the Fresnel approximation

The Fresnel approximation originates from the Huygens-Fresnel principle, which describes the diffraction between two planes (ζ, η) and (x, y) under illumination along the positive direction of a z-axis piercing both planes at their origins[8, p.77-78]. If the planes are separated by a distance z along the z-axis, the relation becomes

$$U(x, y) = \frac{z}{i\lambda} \iint U(\zeta, \eta) \frac{\exp\{ikr\}}{r^2} d\zeta d\eta \tag{2.3}$$

where the distance r is given by

$$r = \sqrt{z^2 + (x - \zeta)^2 + (y - \eta)^2} \tag{2.4}$$

and the integral is taken over all space.

To arrive at the Fresnel approximation, the relation in Equation 2.3 is simplified by applying the Taylor expansion of $\sqrt{1 + x} \approx 1 + \frac{1}{2}x + ...$ to Equation 2.4. This yields the expression[8, p.78-79]

$$r \approx z \left[1 + \frac{1}{2} \left(\frac{x - \zeta}{z} \right)^2 + \frac{1}{2} \left(\frac{y - \eta}{z} \right)^2 + ... \right] \tag{2.5}$$

where the higher order terms may be dropped upon making the paraxial approximation $x, y << z$. Due to a difference in the susceptibility to small changes between the

terms $1/r^2$ and $\exp(r)$, it is deemed sufficient to retain only the first term of the Taylor expansion in the first case, $1/r^2$, while the first two terms are retained in the second, $\exp(r)$. Inserting these two approximate expressions for r into Equation 2.3 and rewriting, the Fresnel integral[8, p.79]

$$U(x,y) = \frac{e^{ikz}}{i\lambda z} \iint U(\zeta,\eta) \exp\left\{\frac{ik}{2z}\left[(x-\zeta)^2 + (y-\eta)^2\right]\right\} d\zeta d\eta \tag{2.6}$$

is obtained.

The Fresnel integral, Equation 2.6, may either be recognized as a convolution relation

$$U(x,y) = \iint U(\zeta,\eta) h(x-\zeta, y-\eta) d\zeta d\eta \,, \tag{2.7a}$$

$$h(x,y) = \frac{e^{ikz}}{i\lambda z} \exp\left\{\frac{ik}{2z}\left[x^2 + y^2\right]\right\} \tag{2.7b}$$

where $h(x,y)$ is the convolution kernel, or rewritten as

$$U(x,y) = \frac{e^{ikz}}{i\lambda z} \exp\left[\frac{ik}{2z}\left(x^2+y^2\right)\right] \mathcal{F}\left\{U(\zeta,\eta) \exp\left[\frac{ik}{2z}\left(\zeta^2+\eta^2\right)\right]\right\} \tag{2.8}$$

with the Fourier transform $\mathcal{F}$ evaluated at $(f_x, f_y) = (x/\lambda z, y/\lambda z)$. For the purposes of the further derivations both the above formulations will be necessary, expressing the Fresnel integral interchangeably either as a convolution or by means of a Fourier transform. Notably, these two formulations are equally valid, requiring no additional approximations.

2.1.2 Wave propagation in the Fraunhofer approximation

A further simplification referred to as the Fraunhofer approximation is obtained when considering either larger propagation distances or smaller FoVs satisfying

$$z >> \frac{k(\zeta^2+\eta^2)_{max}}{2} \,. \tag{2.9}$$

To move from the Fresnel approximation to the Fraunhofer approximation, the quadratic phase factor at the first plane, within the integral, is assumed equal to unity so that Equation 2.8 becomes[8, p.88-89]

$$U(x,y) = \frac{e^{ikz}}{i\lambda z} \exp\left[\frac{ik}{2z}\left(x^2+y^2\right)\right] \mathcal{F}\left\{U(\zeta,\eta)\right\} \tag{2.10}$$

with the Fourier transform evaluated at $(f_x, f_y) = (x/\lambda z, y/\lambda z)$. While this approximation will not be used in this work, it is included here to provide context for the discussion in section 2.5.

2.1.3 Apertures and the generalized pupil function

In the sequel, the generalized pupil function $\mathcal{P}$ will be used to model the properties of the most limiting aperture within a lens system. The generalized pupil function $\mathcal{P}$ is defined as[8, p.205]

$$\mathcal{P}(x, y) = P(x, y) \exp[ikW(x, y)] \tag{2.11}$$

and is reliant on the pupil function P and the wavefront aberration function W. The pupil function describes the finite area from which light is transmitted by the aperture depending on its radius R and is defined by

$$P(x, y) = \begin{cases} 1, & x^2 + y^2 \leq R^2 \\ 0, & x^2 + y^2 > R^2 \, . \end{cases} \tag{2.12}$$

Conversely, the wavefront aberration function is not a property of an ideal aperture, but rather an addition to model the presence of optical aberrations as will be covered further in chapter 4.

2.1.4 Phase shift of a simple lens

Transmission through a lens can be described by a phase change[8, p.158]

$$L(x, y, f_L) = \exp\left[-\frac{ik}{2f_L}\left(x^2 + y^2\right)\right] \, , \tag{2.13}$$

where f_L is the focal length of the lens, as is valid within the paraxial approximation and upon ignoring the finite extent of the lens and the global phase shift. Additionally, one may note that the absence of a lens is equivalent to a lens of focal length $f_L = \infty$ at which point the exponential in Equation 2.13 becomes unity.

2.2 Image-forming lens systems

In this section, we derive the behavior of four idealized lens systems, each consisting of a single aperture, the Aperture Stop (AS) and either a single or two lenses. Defining the object, aperture, and detector planes as the planes containing the respective components, the further derivations will be performed with the intent of relating the complex wavefields at four locations U_1, U_2, U_3 and U_4 as illustrated in Figure 2.2.1. For the sake of a generalized treatment, the lens systems will be considered as special cases of the generalized two-lens system illustrated in Figure 2.2.2.

The generalized two-lens system is defined by propagation through the lens in the front half of the system relating U_1 and U_2, transmission through the AS as described by

$$U_3(x, y) = \mathcal{P}(x, y)U_2(x, y) \tag{2.14}$$

and propagation through the lens in the back half relating U_3 and U_4. For the purposes of FP, an additional requirement is that the field U_2 just before the AS must be related to the field U_1 at the object plane by means of a single Fourier transform, and likewise for the field U_3 just after the AS and the field U_4 at the detector. This is necessary to later define an expression for the sample spectrum, which FP aims to recover. Since only the intensity $I = |U_4|^2$ of the complex wavefield at the detector plane U_4 contributes to the captured images, any phase terms which are constant or only varying across the detector plane may be ignored[8, p.170]. For the present purposes, only the relative intensity is of interest, allowing any constant amplitude scaling factors to be ignored.

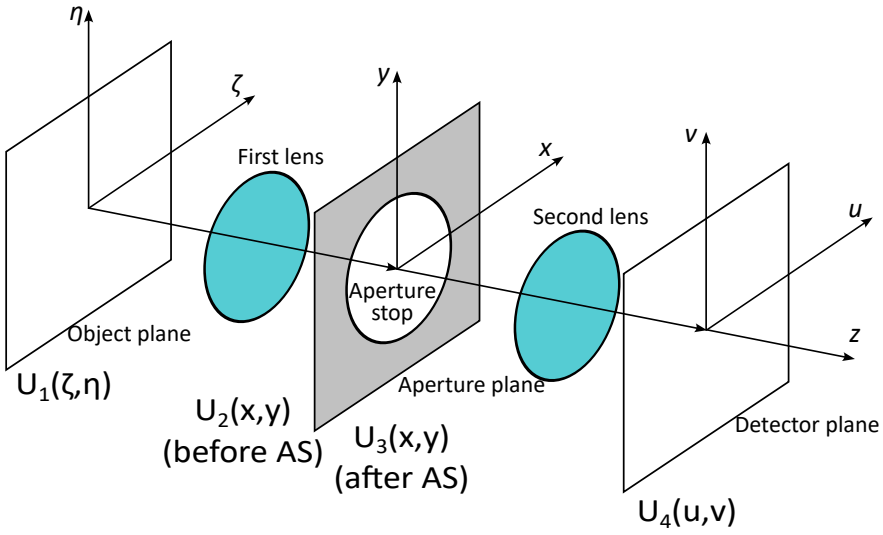

Figure 2.2.1: The three planes of interest in the image formation model. Light is assumed to propagate from left to right along the z-axis. The complex wavefield takes on the values; $U_1(\zeta, \eta)$ in the object plane, $U_2(x, y)$ immediately before transmission through the AS, $U_3(x, y)$ immediately after transmission through the AS and $U_4(u, v)$ at the detector plane. Inspired by figure 2 in [6].

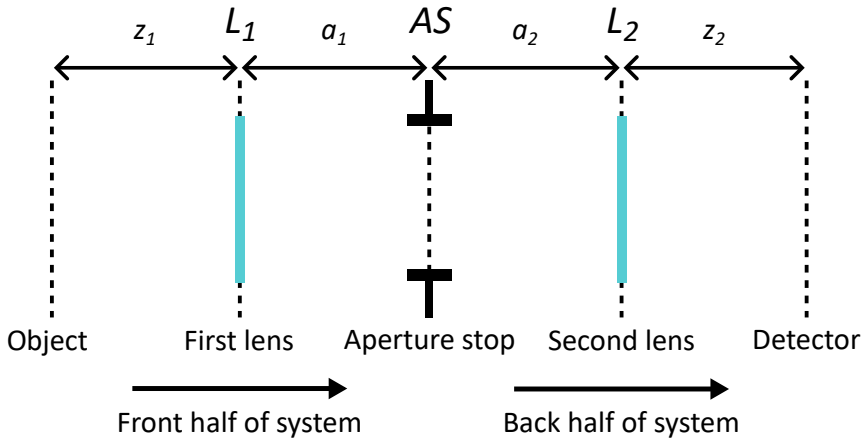

Figure 2.2.2: The generalized imaging system which will be considered further, containing two lenses L_1, L_2 and an aperture stop AS. The front half of the system is defined by the first lens L_1 whose focal length will be denoted f_{L1}, the distance z_1 from the object to the first lens and the distance a_1 from the first lens to the AS. Likewise, the second half of the system is defined by the second lens L_2 whose focal length will be denoted f_{L2}, the distance a_2 from the AS to the second lens and the distance z_2 from the second lens to the detector. Note that the indices of the four propagation distances denote whether the distance is related to the front or back half of the system.

2.2.1 Propagation through front and back halves

To describe the subsystems corresponding to the front and back halves of the generalized system in Figure 2.2.2, a single Fourier transform relationship between the field at a distance d_1 in front of a lens and the field at a distance d_2 behind said lens is required. To solve this problem within the Fresnel approximation, one must account for free space propagation over the first distance, transmission through the lens as described by Equation 2.13 and propagation over the second distance, with the two propagation steps being described by the Fresnel integral as outlined in subsection 2.1.1. Accounting for the fact that the Fresnel integral may be written by means of either a convolution, Equation 2.7, or a Fourier transform, Equation 2.8, there are four alternatives as to how the two propagation steps may be performed. However, only the two alternatives where one of the propagation steps are performed by means of the convolution formulation of the Fresnel integral, Equation 2.7, and the other is performed by means of the Fourier transform formulation, Equation 2.8, are considered further in this work, as the resulting relations then contain only a single Fourier transform.

A complete derivation of the two relations of interest between the field U_F at a distance d_1 in front of a lens and the field U_B at a distance d_2 behind the lens may be found in Appendix B, while only the results will be given below. The relations disregard any constant prefactors and denote the focal length of the lens by f'_L, with the prime added solely to distinguish the focal length from other focal lengths considered in

the following derivations. Applying the Fourier transform formulation of the Fresnel integral for the first distance and the convolution formulation for the second distance yields the relation

$$U_B(u,v) = \exp\left[\frac{ik}{2}\left(\frac{1}{d_1} - \frac{1}{f'_L}\right)\left(u^2+v^2\right)\right] \cdot \mathcal{F}\left\{U_F(x,y)\exp\left[\frac{ik}{2}\left(\frac{1}{d_1} - \frac{d_2}{d_1^2}\right)\left(x^2+y^2\right)\right]\right\} \quad (2.15)$$

where the Fourier transform is to be evaluated at $(f_u, f_v) = (u/\lambda d_1, u/\lambda d_1)$. Applying the convolution formulation first and the Fourier transform formulation second yields the relation

$$U_B(u,v) = \exp\left[\frac{ik}{2}\left(\frac{1}{d_2} - \frac{d_1}{d_2^2}\right)\left(u^2+v^2\right)\right] \cdot \mathcal{F}\left\{U_F(x,y)\exp\left[\frac{ik}{2}\left(\frac{1}{d_2} - \frac{1}{f'_L}\right)\left(x^2+y^2\right)\right]\right\} \quad (2.16)$$

where the Fourier transform is to be evaluated at $(f_u, f_v) = (u/\lambda d_2, u/\lambda d_2)$. An important distinction between these two relations is the scaling of the frequencies (f_u, f_v) at which the Fourier transform is evaluated. This is directly related to the magnification of the system as will be covered in subsection 2.2.3.

2.2.2 Generalized expression relating the wavefields at the object and detector planes

As each half of the system may be described by either Equation 2.15 or Equation 2.16 there are four alternative expressions which may describe the generalized imaging system under consideration. However, the physically interesting combinations may be limited based on the telecentric properties of the system, as will be considered in subsection 2.2.4, and by only considering descriptions of the system which eliminate the phase terms at the aperture plane, corresponding to the system being at focus. Furthermore, the phase term at the detector plane is ignored according to the previously presented argument regarding intensity imaging.

Under these assumptions, we will show that the wavefield at the detector for all the lens systems considered in this work can be reduced to the form

$$U_4(u,v) = \mathcal{F}\left\{\mathcal{P}(x,y)\mathcal{F}\left\{U_1(\zeta,\eta)Q(\zeta,\eta)\right\}\right\} \ , \quad (2.17)$$

with $Q(\zeta,\eta)$ being a quadratic phase term at the object plane and with the inner and outer Fourier transforms being evaluated at respectively $(f_x, f_y) = (x/\lambda z_a, y/\lambda z_a)$ and $(f_u, f_v) = (u/\lambda z_b, u/\lambda z_b)$, with $z_a \in \{z_1, a_1\}$ and $z_b \in \{a_2, z_2\}$ depending on which of Equation 2.15 and Equation 2.16 are used for the front and back halves of the system.

For a further generalization, one may write Q in terms of an effective distance z_q such that

$$Q(\zeta, \eta) = \frac{1}{z_q}(\zeta^2 + \eta^2) \,, \tag{2.18}$$

resulting in the behavior of the lens system being defined fully by the distances z_a, z_b and z_q in addition to the AS size R and the aberrations W contained in the generalized pupil function $\mathcal{P}$ according to Equation 2.11. Since the value of z_q is given directly by the object to AS distance for the thin lens system which will be considered in subsection 2.2.5, it will be referred to as the effective object to AS distance.

2.2.3 Magnification

Following a more extensive argument by Goodman[8, p.170-172], under the assumption that neither $Q(\zeta, \eta)$ nor $\mathcal{P}(x, y)$ substantially impact the image formation process over a small region, the magnification may be found as the negative of the ratio between the scaling factors of the frequencies at which the two Fourier transforms in Equation 2.17 are evaluated. That is, the magnification is given by $K = -|K|$ and

$$|K| = \frac{\lambda z_b}{\lambda z_a} = \frac{z_b}{z_a} \tag{2.19}$$

with the minus sign implying that the image is inverted as compared to the object, originating from the duality property of the Fourier transform according to

$$\mathcal{F}\left\{\mathcal{F}\left\{U(x, y)\right\}\right\} = \mathcal{F}\left\{\mathcal{F}^{-1}\left\{U(-x, -y)\right\}\right\} = U(-x, -y) \tag{2.20}$$

as shown at unity magnification.

2.2.4 Telecentricity

Defining the properties of object-side and image-side telecentricity as invariance of the magnification upon a change in the location of the object and detector planes[9], one would expect that the properties are dependent on whether Equation 2.15 or Equation 2.16 are used for respectively the front and back half of the lens system. In terms of the generalized lens system in Figure 2.2.2, this would affect whether the evaluation frequencies of the Fourier transform used in the description of the front half of the system depends on a_1 rather than z_1 and whether the evaluation frequencies of the Fourier transform used in the description of the back half of the system depends on a_2 rather than z_2. Based on whether a system is expected to display telecentricity, this may serve to guide the choice between application of Equation 2.15 or Equation 2.16 for each half of the generalized imaging system. According to Born and Wolf[10, p.186-187], object-side telecentricity is expected when the defining AS is at the back focal plane of the preceding subsystem, that is $a_1 = f_{L1}$, while image-side telecentricity is expected if the defining AS is at the front focal plane of the succeeding subsystem,

that is $a_2 = f_{L2}$. Systems which are both object-side and image-side telecentric are referred to as bi-telecentric.

2.2.5 Single-lens system with the aperture stop at the lens

The first lens system which will be considered is illustrated in Figure 2.2.3, and is defined by a single lens of focal length f_L in the same plane as the AS and the distances z_1 and z_2 from the AS to respectively the object and detector planes. Conventionally, the system may be analyzed by modeling the two free space propagation steps with the Fourier transform formulation of the Fresnel integral, Equation 2.8, and the transmission through the AS and lens by multiplication with $\mathcal{P}(x, y)$ and $L(x, y)$ as respectively defined by Equation 2.11 and Equation 2.13. This procedure is covered by for instance Goodman[8, p.168-174], Hazanzade[6] and was considered in the preceding project conducted by the author[7]. This system will be referred to as a thin lens system.

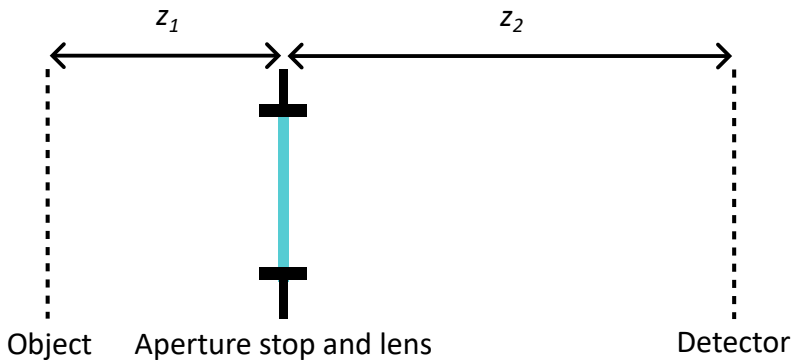

Figure 2.2.3: Illustration of a single lens system with the AS at the same plane as the lens. In terms of the generalized lens system in Figure 2.2.2, the system may be described by the parameters $a_1 = a_2 = 0$, and by attributing the entirety of the lens to one half of the system. If the lens is attributed to the front half of the system, the behavior of the back half may equivalently be described Equation 2.16 and by free space propagation over the distance z_2 utilizing the Fourier transform formulation of the Fresnel integral.

To arrive at the same result within the confines of the generalized two-lens system illustrated in Figure 2.2.2, one may set $a_1 = a_2 = 0$ and attribute the entirety of the lens to one half of the system. For instance, one may set $f_{L1} = f_L$ and $f_{L2} = \infty$, the latter of which is synonymous with the absence of a focusing element. Considering the back half of the system, inserting the values of a_2 and $f_{L2} = \infty$ into Equation 2.16 reduces the equation to be identical to free space propagation as described by the Fourier transform formulation of the Fresnel integral, that is Equation 2.8.

To describe the front half of the system one may then insert $d_1 = z_1$, $f'_L = f_{L1}$ and $d_2 = a_1 = 0$ into Equation 2.15 yielding the relation

$$U_2(x, y) = \exp\left[\frac{ik}{2}\left(\frac{1}{z_1} - \frac{1}{f_{L1}}\right)\left(x^2 + y^2\right)\right] \cdot \mathcal{F}\left\{U_1(\zeta, \eta) \exp\left[\frac{ik}{2z_1}\left(\zeta^2 + \eta^2\right)\right]\right\} \quad (2.21)$$

where the Fourier transform is to be evaluated at $(f_x, f_y) = (x/\lambda z_1, y/\lambda z_1)$.

For the back half, applying either Equation 2.8 to describe free space propagation over the distance z_2 or Equation 2.16 with $d_1 = a_2 = 0$, $f'_L = f_{L2} = \infty$ and $d_2 = z_2$ would equivalently yield the relation

$$U_4(u,v) = \exp\left[\frac{ik}{2z_2}\left(u^2+v^2\right)\right]\mathcal{F}\left\{U_3(x,y)\exp\left[\frac{ik}{2z_2}\left(x^2+y^2\right)\right]\right\} \tag{2.22}$$

where the Fourier transform is to be evaluated at $(f_u, f_v) = (u/\lambda z_2, u/\lambda z_2)$.

For the phase terms at the aperture plane to cancel, that is the terms depending on (x, y), one may observe that the values of z_1 and z_2 must satisfy the thin lens equation from geometrical optics[8, p.170]

$$\frac{1}{f_L} = \frac{1}{z_1} + \frac{1}{z_2}\,. \tag{2.23}$$

If this relation is not satisfied the system would be out of focus, with the ideal focus being defined by the cancellation of the quadratic phase at the aperture plane, which would otherwise have a blurring effect on the final image[8, p.170].

Combining the above equations with Equation 2.14, relating U_2 and U_3, and ignoring the phase at the detector yields the final result

$$U_4(u,v) = \mathcal{F}\left\{\mathcal{P}(x,y)\mathcal{F}\left\{U_1(\zeta,\eta)\exp\left[\frac{ik}{2z_1}\left(\zeta^2+\eta^2\right)\right]\right\}\right\} \tag{2.24}$$

with the inner and outer Fourier transforms evaluated at respectively $(f_x, f_y) = (x/\lambda z_1, y/\lambda z_1)$ and $(f_u, f_v) = (u/\lambda z_2, u/\lambda z_2)$. This derivation yields the same result as the derivation performed by Goodman[8, p.168-174].

For the generalized expression in Equation 2.17, the three defining distances become

$$z_a = z_1, \qquad z_b = z_2, \qquad z_q = z_1 \tag{2.25}$$

from which the magnification of the system can be found as

$$|K| = \frac{z_2}{z_1} \tag{2.26}$$

by applying Equation 2.19. Additionally, for a given magnification $|K|$ and focal length f_L, the required values of z_1 and z_2 are given by

$$z_1 = f_L(1 + 1/|K|) \tag{2.27a}$$

$$z_2 = f_L(1 + |K|) \tag{2.27b}$$

as found by application of Equation 2.23 and Equation 2.26.

2.2.6 Object-side telecentric single-lens system

The second lens system we will consider is illustrated in Figure 2.2.4, and differs from the previously considered system in subsection 2.2.5 by the fact that the AS is placed in the back focal plane of the lens, rather than at the lens. Following the discussion in subsection 2.2.4, one expects this system to exhibit the property of object-side telecentricity. In relation to the generalized two-lens system, Figure 2.2.2, this system may be modelled by setting $f_{L1} = a_1 = f_L$, $a_2 = 0$ and $f_{L2} = \infty$.

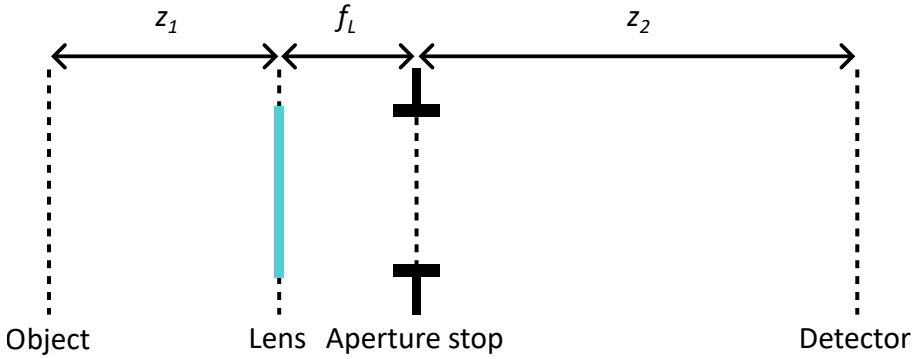

Figure 2.2.4: Illustration of a single lens system with the AS at the back focal plane of the lens. In terms of the generalized lens system in Figure 2.2.2, the system may be described by the parameters $f_{L1} = a_1 = f_L$, $a_2 = 0$ and $f_{L2} = \infty$.

Applying Equation 2.16 to describe the front half of the system in line with the expected object side telecentricity then yields the relation

$$U_2(x,y) = \exp\left[\frac{ik}{2}\left(\frac{1}{f_L} - \frac{z_1}{f_L^2}\right)\left(x^2+y^2\right)\right]\mathcal{F}\left\{U_1(\zeta,\eta)\right\} \tag{2.28}$$

where the Fourier transform is to be evaluated at $(f_x, f_y) = (x/\lambda f_L, y/\lambda f_L)$.

As for the previous system, applying either Equation 2.8 to describe free space propagation over the distance z_2 or Equation 2.16 with $d_1 = a_2 = 0$, $f_L' = f_{L2} = \infty$ and $d_2 = z_2$ would equivalently yield the relation

$$U_4(u,v) = \exp\left[\frac{ik}{2z_2}\left(u^2+v^2\right)\right]\mathcal{F}\left\{U_3(x,y)\exp\left[\frac{ik}{2z_2}\left(x^2+y^2\right)\right]\right\} \tag{2.29}$$

where the Fourier transform is to be evaluated at $(f_u, f_v) = (u/\lambda z_2, u/\lambda z_2)$.

For the quadratic phase at the aperture plane to disappear at focus, the requirement

$$\frac{1}{f_L} + \frac{1}{z_2} = \frac{z_1}{f_L^2} \tag{2.30}$$

must be imposed on z_1 and z_2.

Combining the above equations with Equation 2.14 and ignoring the phase at the detector then yields the final result

$$U_4(u,v) = \mathcal{F}\left\{\mathcal{P}(x,y)\mathcal{F}\left\{U_1(\zeta,\eta)\right\}\right\} \tag{2.31}$$

with the inner and outer Fourier transforms evaluated at respectively $(f_x, f_y) = (x/\lambda f_L, y/\lambda f_L)$ and $(f_u, f_v) = (u/\lambda z_2, u/\lambda z_2)$, noting that $Q(\zeta, \eta)$ is equal to unity and thus vanishes.

In the generalized expression, Equation 2.17, the three defining distances become

$$z_a = f_L, \qquad z_b = z_2, \qquad z_q = \infty \tag{2.32}$$

based on the evaluation frequencies of the two Fourier transforms and the fact that the quadratic phase term vanishes. Recognizing that z_q was given directly by the distance from the objective plane to the AS for the simpler preceding system, one may consider the value of $z_q = \infty$ to be in line with the argumentation by Born and Wolf[10, p.186-187] stating that the effective distance from the object plane to the AS is infinite for an object-side telecentric system.

Applying Equation 2.19 yields

$$|K| = \frac{z_2}{f_L} \tag{2.33}$$

from which one may note that the object side telecentric nature of the system is reflected in that the magnification is independent of z_1. Further, by combining Equation 2.30 and Equation 2.33 the required values of z_1 and z_2 may be found as

$$z_1 = f_L(1 + 1/|K|) \tag{2.34a}$$

$$z_2 = f_L|K| \tag{2.34b}$$

for a given magnification $|K|$ and focal length f_L.

2.2.7 Bi-telecentric 4f-system

The third lens system to be considered is illustrated in Figure 2.2.5, and may be defined by two lenses of focal lengths f_{L1} and f_{L2} with the propagation distances equal to the focal lengths of the lenses. This places the object in the front focal plane of the first lens, the detector in the back focal plane of the second lens, and the AS simultaneously in both the back focal plane of the first lens and the front focal plane of the second lens. For an alternative derivation of the behavior of this system, the interested reader may consult Gaskill[11, p.474] or Mertz[12, p.59-61]. Conventionally, this system is often referred to as a 4f-system[12, 13, 14] and has previously been proposed as a model system for infinity-corrected microscope systems within the context of FP[13]. In line with the discussion of telecentricity in subsection 2.2.4, the system would be expected to be both object- and image-side telecentric.

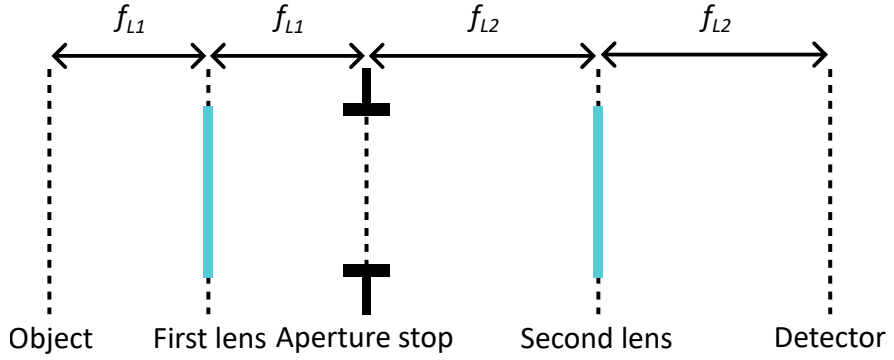

Figure 2.2.5: Illustration of a two-lens system with all distances corresponding to the focal lengths of the lenses, which for respectively the first and second lenses are given as f_{L1} and f_{L2}. In terms of the generalized lens system in Figure 2.2.2, the system may be described by the parameters $z_1 = a_1 = f_{L1}$, $z_2 = a_2 = f_{L2}$.

Within the confines of the generalized two-lens system in Figure 2.2.2 the system may be described by setting $z_1 = a_1 = f_{L1}$, $z_2 = a_2 = f_{L2}$. At focus, both halves of the system may be equivalently considered through either Equation 2.15 or Equation 2.16 with $d_1 = d_2 = f'_L$, at which point both equations reduce to precise Fourier transform relations

$$U_B(u, v) = \mathcal{F}\{U_F(x, y)\} \tag{2.35}$$

evaluated at $(f_u, f_v) = (u/\lambda f'_L, v/\lambda f'_L)$.

For the front half of the system, the evaluation of the Fourier transform may be considered to be dependent on the distance a_1 rather than z_1, in line with the expected object-side telecentricity. The front half of the system is then described by

$$U_2(x, y) = \mathcal{F}\{U_1(\zeta, \eta)\} \tag{2.36}$$

where the Fourier transform is to be evaluated at $(f_x, f_y) = (x/\lambda f_{L1}, y/\lambda f_{L1})$.

For the back half of the system, the evaluation of the Fourier transform may similarly be considered to be dependent on the distance a_2 rather than z_2, in line with the

expected image-side telecentricity. The back half of the system is then described by

$$U_4(u,v) = \mathcal{F}\{U_3(x,y)\} \tag{2.37}$$

where the Fourier transform is to be evaluated at $(f_u, f_v) = (u/\lambda f_{L2}, v/\lambda f_{L2})$.

Combining the two above equations with Equation 2.14 and ignoring the phase at the detector yields the final result

$$U_4(u,v) = \mathcal{F}\{\mathcal{P}(x,y)\mathcal{F}\{U_1(\zeta,\eta)\}\} \tag{2.38}$$

with the inner and outer Fourier transforms evaluated at respectively $(f_x, f_y) = (x/\lambda f_{L1}, y/\lambda f_{L1})$ and $(f_u, f_v) = (u/\lambda f_{L2}, u/\lambda f_{L2})$.

In terms of the generalized model, the system is defined by

$$z_a = a_1 = f_{L1}, \qquad z_b = a_2 = f_{L2}, \qquad z_q = \infty \tag{2.39}$$

consistent with the system being bi-telecentric and having a magnification

$$|K| = \frac{f_{L2}}{f_{L1}} \tag{2.40}$$

as given by application of Equation 2.19.

2.2.8 Two-lens system with arbitrary aperture stop placement

The fourth and final lens system which will be considered is illustrated in Figure 2.2.6, and will serve to demonstrate the need to account for a variable z_q. The system is similar to the previously considered 4f-system, except that the location of the AS is allowed to vary. Notably, the object is assumed to be in the front focal plane of the first lens, while the image is assumed to be formed at the back focal plane of the second lens. With the variable AS placement, this would generally be consistent with the system being non-telecentric.

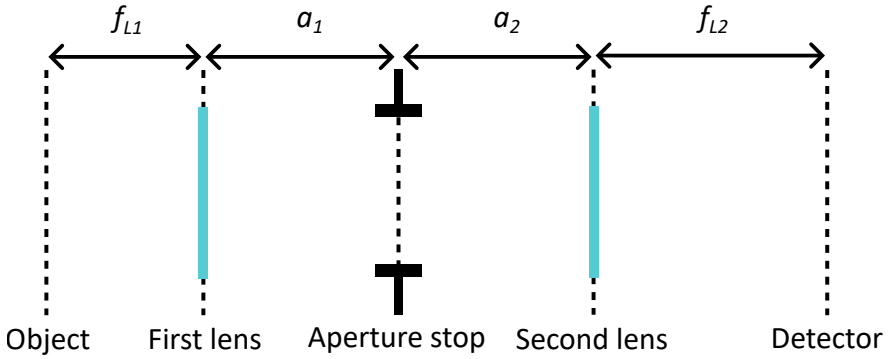

Figure 2.2.6: Illustration of a two-lens system with an arbitrarily located AS and the object and detector at the front and back focal planes of respectively the first and second lenses. In terms of the generalized lens system in Figure 2.2.2, the system may be described by the parameters $z_1 = f_{L1}$, $z_2 = f_{L2}$ while a_1 and a_2 are allowed to vary freely.

the generalized two-lens system in Figure 2.2.2 may be adapted by setting $z_1 = f_{L1}$, $z_2 = f_{L2}$. Starting out, the non-telecentric case will be analyzed, at which point the front half of the system is described by

$$U_2(x,y) = \mathcal{F}\left\{U_1(\zeta,\eta)\exp\left[\frac{ik}{2}\left(\frac{1}{f_{L1}} - \frac{a_1}{f_{L1}^2}\right)\left(\zeta^2+\eta^2\right)\right]\right\} \tag{2.41}$$

where the Fourier transform is to be evaluated at $(f_u, f_v) = (u/\lambda z_1, u/\lambda z_1)$ and the back half is described by

$$U_4(u,v) = \exp\left[\frac{ik}{2}\left(\frac{1}{f_{L2}} - \frac{a_2}{f_{L2}^2}\right)\left(u^2+v^2\right)\right]\mathcal{F}\left\{U_3(x,y)\right\} \tag{2.42}$$

where the Fourier transform is to be evaluated at $(f_u, f_v) = (u/\lambda z_2, u/\lambda z_2)$.

Combining the two above equations with Equation 2.14 and ignoring the phase at the detector yields the final result

$$U_4(u,v) = \mathcal{F}\left\{\mathcal{P}(x,y)\mathcal{F}\left\{U_1(\zeta,\eta)\exp\left[\frac{ik}{2}\left(\frac{1}{f_{L1}} - \frac{a_1}{f_{L1}^2}\right)\left(\zeta^2+\eta^2\right)\right]\right\}\right\} \tag{2.43}$$

with the inner and outer Fourier transforms evaluated at respectively $(f_x, f_y) = (x/\lambda z_1, y/\lambda z_1)$ and $(f_u, f_v) = (u/\lambda z_2, u/\lambda z_2)$.

In terms of the generalized model, the system is defined by

$$z_a = z_1 = f_{L1}, \qquad z_b = z_2 = f_{L2}, \qquad z_q = \left(\frac{1}{f_{L1}} - \frac{a_1}{f_{L1}^2}\right)^{-1} \tag{2.44}$$

yielding a non-telecentric system of magnification

$$|K| = \frac{z_2}{z_1} = \frac{f_{L2}}{f_{L1}} \tag{2.45}$$

as given by application of Equation 2.19.

Four special cases of interest are when either $a_1 = a_2 = 0$, $a_1 = f_{L1}$, $a_2 = f_{L2}$ or both $a_1 = f_{L_2}$ and $a_2 = f_{L2}$. In the first case, one may observe that the system becomes equivalent to the thin lens system considered in subsection 2.2.5. The remaining three cases will be covered in the subsequent paragraphs.

Considering the back half of the system, one may notice that upon ignoring the phase at the detector plane, the relation between U_3 and U_4 is reduced to a perfect Fourier transform as in Equation 2.37, with the only difference being that the evaluation is dependent on $z_2 = f_{L2}$ rather than on $a_2 = f_{L2}$. As such, the behavior of the system may be seen to be independent of the value of a_2 if the system is assumed to not be image-side telecentric. When used as a model system for an infinity-corrected microscope system, this independence from the value of a_2 would serve to explain why the so called infinity-space[15] is allowed to vary within reason without affecting the behavior of the imaging system. Further, in the special case where $a_2 = f_{L2}$, Equation 2.37 used for the 4f-system may be applied instead of the above equation relating U_3 and U_4, at which point the behavior of the system remains unchanged except that it additionally becomes image-side telecentric.

Considering the front half of the system, the impact of a_1 may be found in the expression for z_q. As a_1 increases from zero, the magnitude of z_q may be seen to increase from $z_q = z_1 = f_{L1}$ to $z_q = \infty$ when $a_1 = f_{L1}$, at which point the quadratic phase at the object plane may be seen to disappear. Once a_1 becomes larger than f_{L1}, z_q increases from $z_q = -\infty$ towards zero. Notably, the value of $1/z_q$, and thus the quadratic phase at the object plane, is continuous at $a_1 = f_{L1}$, while z_q shifts from positive to negative infinity. For the particular case $a_1 = f_{L1}$ when the quadratic phase disappears, the relation between U_1 and U_2 is reduced to a perfect Fourier transform, as in Equation 2.36. In this case, the derived behavior of the system may be retained under the additional assumption that it is object-side telecentric. At this point, the behavior reduces to be identical to the previously considered two-lens system considered in subsection 2.2.7, except for the fact that the system would not be image-side telecentric and that the behavior would be independent of a_2. In the case where $a_2 = f_{L2}$ as well, the system would be identical to the bi-telecentric 4f-system.

2.2.9 Summary and ray optical visualization

Summarizing the above sections, we have demonstrated the reduction of the considered single and two lens systems to the form

$$U_4(u,v) = \mathcal{F}\left\{\mathcal{P}(x,y)\mathcal{F}\left\{U_1(\zeta,\eta)Q(\zeta,\eta)\right\}\right\} \tag{2.46}$$

with

$$Q(\zeta,\eta) = \frac{1}{z_q}(\zeta^2+\eta^2)\ . \tag{2.47}$$

Importantly, in addition to the AS size R and aberrations W contained in the generalized pupil function $\mathcal{P}$, the derivations imply that the ideal behavior of an arbitrary single- or two-lens imaging system may be described fully by the distances z_a and z_b, defining the magnification and the scaling of the Fourier transforms, and the effective object to AS distance z_q, defining the quadratic phase at the object plane. Considering the fact that most microscope objectives are quite complex and essentially operate as black boxes[8, p.186-189], this generalization may prove useful when it comes to more accurately evaluating and correcting for the behavior of such unknown imaging systems. Based on the above derivations, z_q can take on any real value, depending on the distance a_1 from the lens element in the front half of the lens system and the defining AS. Particularly, a consequence of object-side telecentricity is that z_q becomes infinite. Comparatively, the value of a_2 and whether an objective is image-side telecentric, does not impact the final imaging equation due to the phase at the detector vanishing upon intensity imaging.

To further illustrate the behavior of the imaging systems covered in this section, Figure 2.2.7 and Figure 2.2.8 show how the systems behave from a ray optical perspective. To calculate the points at which the rays are transmitted through the lenses based on the known points at the object and aperture plane, the paraxial ray trace equations were used[16, p.33].

From the perspective of geometrical optics, the value of z_q appears to coincide with the axial location of the Entrance Pupil (EnP). The EnP is defined as the image of the AS formed by the front half of the system[16, p.55]. Notably, the axial location of the EnP is defined by the z value, relative to the object plane, where the chief rays would intersect the optical axis if they were not focused by the lens[16, p.46-47]. As illustrated in Figure 2.2.9, this is consistent with the value of z_q for the considered lens systems where $z_1 = f_{L1}$ is assumed. Whether this is the case for an arbitrarily defined multi-lens system should be considered further in future works.

From the figures, one may further note the relation between the value of z_q and the angle of the chief ray for off-center points. Since the zeroth diffraction order is scattered parallel to the optical axis under non-angled plane wave illumination, the angle of the chief ray may be understood as a frequency shift of the local Fourier spectrum. While the ray optical interpretation of the frequency shift will not be pursued further, a wave optical derivation explaining the relation between z_q and the frequency shift for off-axis regions will be made in subsection 2.3.2.

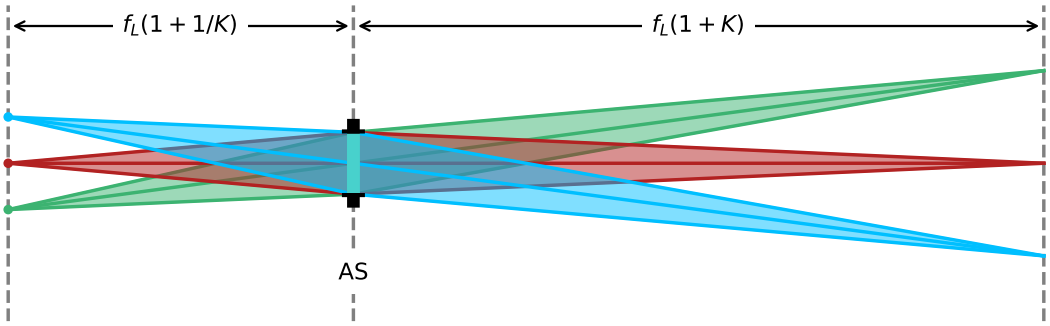

(a) Thin lens system

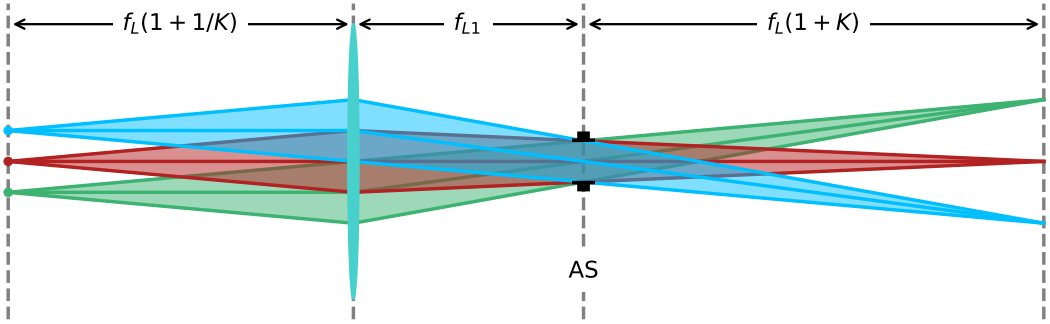

(b) Object-side telecentric single-lens system

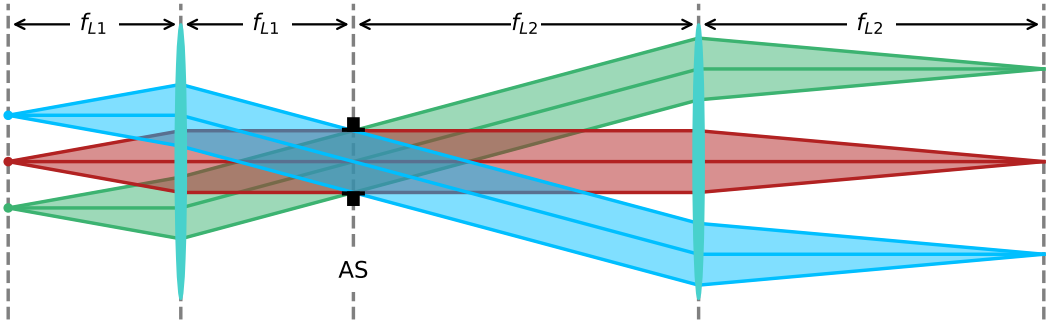

(c) Bi-telecentric 4f-system

Figure 2.2.7: Visualization of image formation based on ray tracing for the thin lens, object-side telecentric single-lens and bi-telecentric 4f lens systems. Notably, the chief rays for the telecentric system halves may be seen to be parallel to the optical axis. Conversely, the chief rays of the off-axis points are angled for the non-telecentric system halves.

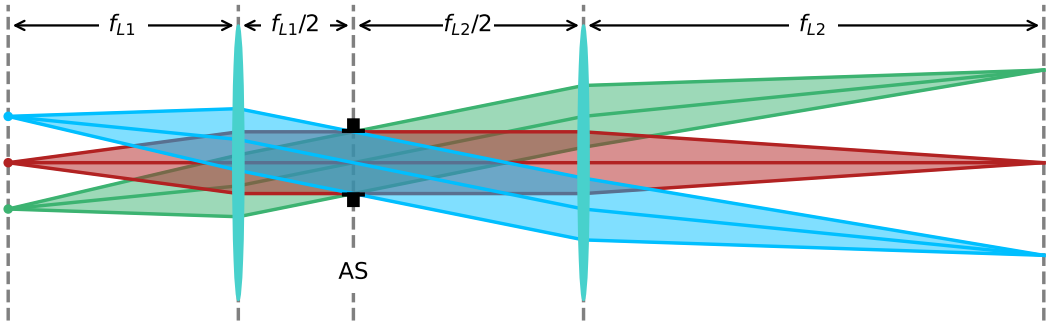

(a) Generalized two lens system ($a_1 < f_{L1}$)

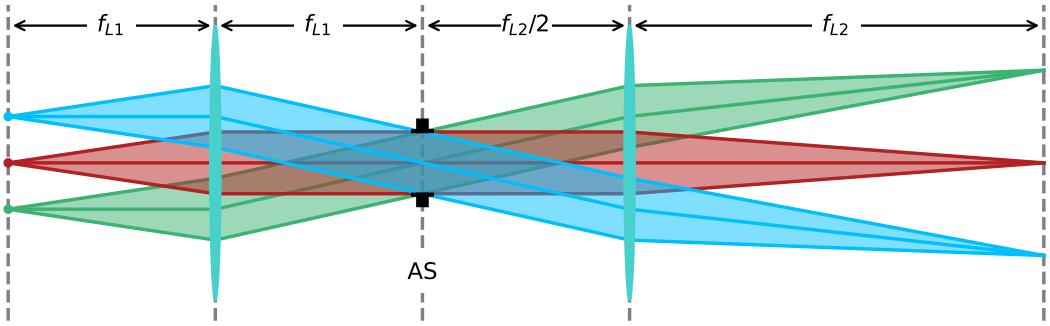

(b) Generalized two lens system ($a_1 = f_{L1}$)

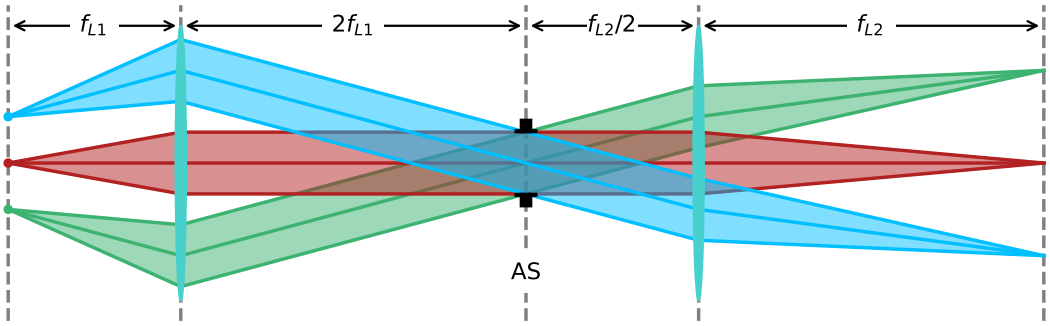

(c) Generalized two lens system ($a_1 > f_{L1}$)

Figure 2.2.8: Visualization of image formation based on ray tracing for three two-lens systems with varying AS placement. The systems are ordered by increasing values of a_1. (a) A system where $a_1 < f_{L1}$, corresponding to a finite and positive value of z_q. (b) A system where $a_1 = f_{L1}$, consistent with a object-side telecentric system with $z_q = \infty$. (c) A system where $a_1 > f_{L1}$, corresponding to a finite and negative value of z_q. Notably, the value of z_q appears to be related to the angle of the chief ray for off-axis points. While only three examples are presented here, one should note that the model allows for any AS placement at or in between the two lenses. Further, one may observe that the rays for the off-axis points for increasing values of a_1 are transmitted through the lens at increasing distances from the optical axis. As the AS to lens distance increases, or for a farther off-axis point, one would thus eventually expect vignetting to become an issue. Correspondingly, to avoid vignetting within the desired FoV, the lenses are required to be significantly larger than the defining AS. While the focus of this figure is to demonstrate the effects of changing a_1, the symmetry of the two system halves dictate that changing a_2 would yield comparable behavior for the second half of the system.

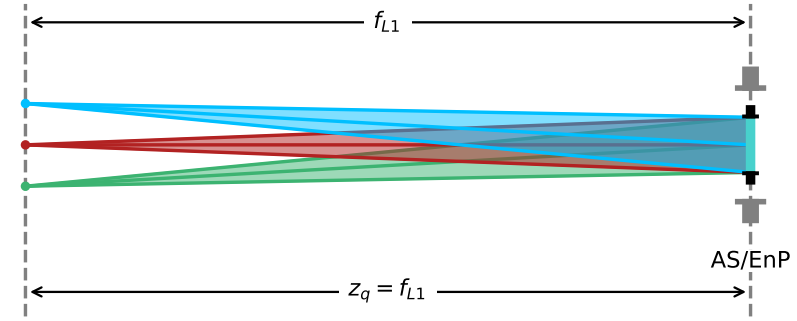

(a) $a_1 = 0$

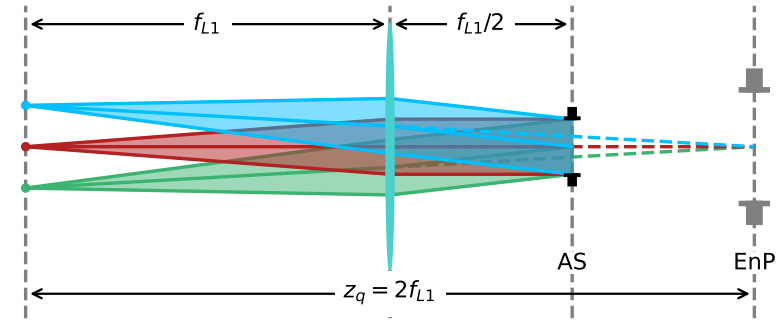

(b) $a_1 = f_{L1}/2$

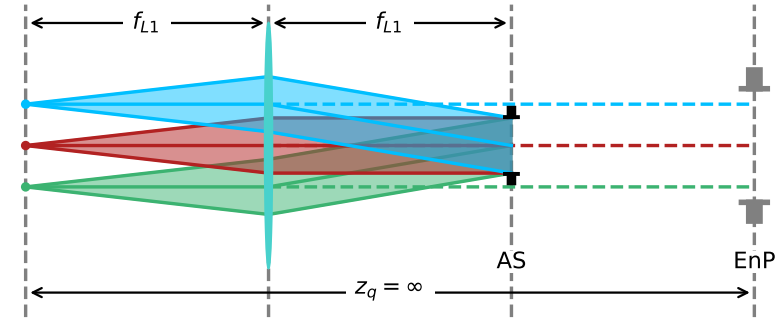

(c) $a_1 = f_{L1}$

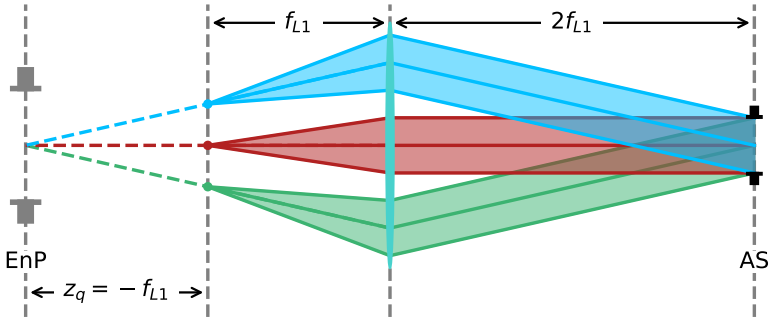

(d) $a_1 = 2f_{L1}$

Figure 2.2.9: The front half of the considered imaging system for different values of a_1. The value which has been referred to as the effective object to AS distance, z_q, coincides with where the chief rays would intersect the optical axis if they were not focused by the lens. This is consistent with the definition of the axial position of the Entrance Pupil (EnP) in geometrical optics[16, p.46-47].

2.3 LED illumination model

Another aspect of the imaging system which will be considered is how the image formation is modified by illumination from the individual LEDs of a LED array placed in the illumination plane. To this extent, the definition of two additional wavefields U_i and U_{LED} will be required in line with the illustration in Figure 2.3.1. Specifically, $U_i(\zeta, \eta)$ is defined as the complex wavefield at the object plane just before transmission through a complex object $o(\zeta, \eta)$ that is to be imaged, while U_{LED} is defined as the complex wavefield at the illumination plane directly corresponding to the LED source. These two fields are related by propagation over the distance z_0 between the illumination and object planes, while they are related to the imaging model described earlier through

$$U_1(\zeta, \eta) = o(\zeta, \eta) U_i(\zeta, \eta). \tag{2.48}$$

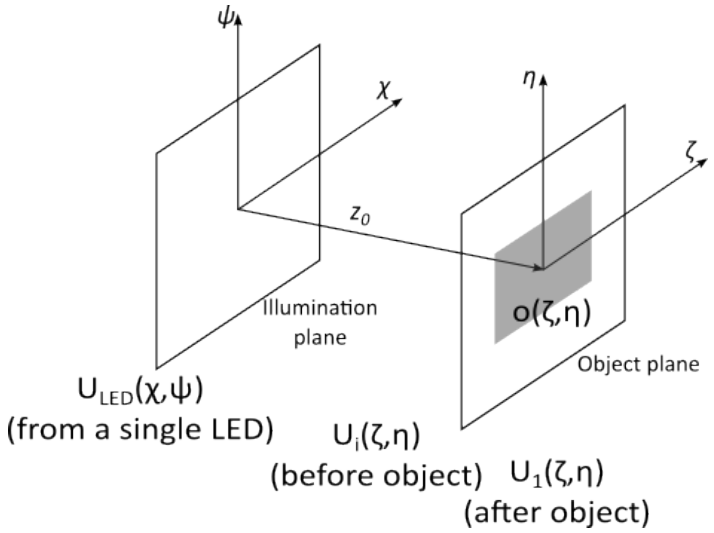

Figure 2.3.1: The planes and complex fields of interest in the illumination model. Each individual LED results in a corresponding complex field $U_{LED}(\chi, \psi)$ at the illumination plane which is propagated to the object plane. This results in complex fields $U_i(\zeta, \eta)$ and $U_1(\zeta, \eta)$ just before and just after transmission through a complex object $o(\zeta, \eta)$ at the object plane.

For a complete treatment starting at the Fresnel-Huygens principle, $U_i(\zeta, \eta)$ may be found using Equation 2.3 yielding

$$U_i(\zeta, \eta) = \iint U(\chi, \psi) \frac{\exp\{ikr\}}{r^2} d\chi d\psi \tag{2.49}$$

ignoring the constant prefactor $z_0/i\lambda$ and where the distance r is given by

$$r = \sqrt{z_0^2 + (\zeta - \chi)^2 + (\eta - \psi)^2} \tag{2.50}$$

in accordance with Equation 2.4. However, to arrive at the model commonly used in Fourier Ptychography [1, 2, 5, 6] further simplifications are necessary.

The first approximation is to model the LEDs as point sources, neglecting their finite extent[5]. For the i-th LED located at (χ_i, ψ_i) in the illumination plane, the point source approximation allows the complex field to be expressed as a delta function $U_{LED} = \delta(\chi_i, \psi_i)$, yielding

$$U_i(\zeta, \eta) = \frac{\exp\{ikr\}}{r^2} \tag{2.51}$$

with r evaluated at (χ_i, ψ_i).

The second approximation is to ignore the term $1/r^2$, which is an intensity scaling factor that varies across the field of view in the object plane and between LED sources. Recognizing that the illumination distance z_0 will commonly be substantially larger than the FOV[1, 5], one would not expect the assumption of constant illumination intensity across the whole object plane to have substantial impact. However, since the ratios χ_i/z_0 and ψ_i/z_0 may take on values approaching or surpassing unity to achieve large illumination angles, a non-negligible intensity variation between LED sources may be ignored through this approximation.

Finally, the Taylor expansion used for the Fresnel approximation as given in Equation 2.5 is used[5] while including the first two terms. This yields the final result

$$U_i(\zeta, \eta) = \exp\left[\frac{ik}{2z_0}\left(\zeta^2 + \eta^2\right) - \frac{ik}{z_0}\left(\zeta\chi_i + \eta\psi_i\right)\right] \tag{2.52}$$

where the terms ikz_0 and $ik\left(\chi_i^2 + \psi_i^2\right)/2z_0$ have been removed from the exponent as they are constant for a given LED and thus removed during intensity imaging.

2.3.1 Impact of LED illumination for an on-axis region

The impact of LED illumination may be seen most easily through examination of the wavefield U_2 at the aperture plane just before transmission through the AS. Combining the generalized model considered in section 2.2 with Equation 2.48 and Equation 2.52, U_2 may be expressed as the Fourier transform of

$$o(\zeta, \eta)Q_c(\zeta, \eta)\exp\left[-\frac{ik}{z_0}\left(\zeta\chi_i + \eta\psi_i\right)\right] \tag{2.53}$$

evaluated at $(f_x, f_y) = (x/\lambda z_a, y/\lambda z_a)$, where Q_c is a combined quadratic phase term

$$Q_c(\zeta, \eta) = \exp\left[\frac{ik}{2z_0}\left(\zeta^2 + \eta^2\right) + \frac{ik}{2z_q}\left(\zeta^2 + \eta^2\right)\right] \tag{2.54}$$

$$= \exp\left[\frac{ik}{2}\left(\frac{1}{z_0} + \frac{1}{z_q}\right)\left(\zeta^2 + \eta^2\right)\right] \tag{2.55}$$

including the terms originating from the spherical illumination and the quadratic phase term at the object plane inherent to the generalized imaging system considered throughout section 2.2.

When compared to direct illumination, the final term may be seen as a spatial shift of the wavefield at the aperture plane. Defining the Fourier transform of Equation 2.53 at direct illumination as the object spectrum S yields a relation

$$U_2(x,y) = S(f_x, f_y) = \mathcal{F}\{o(\zeta,\eta)Q_c(\zeta,\eta)\} \tag{2.56}$$

with the implicit evaluation of the Fourier transform. To observe the impact of angled illumination, one may rewrite the final term of Equation 2.53 as

$$\exp\left[-\frac{ik}{z_0}(\zeta\chi_i + \eta\psi_i)\right] = \exp\left[-\frac{i2\pi}{\lambda z_0}(\zeta\chi_i + \eta\psi_i)\right] \tag{2.57}$$

and use the Fourier shift theorem to arrive at

$$U_2(x,y) = S(f_x - f_{xi}, f_y - f_{yi}) \tag{2.58}$$

where $(f_{xi}, f_{yi}) = (-\chi_i/\lambda z_0, -\psi_i/\lambda z_0)$[5]. As the AS is centered at the optical axis, the impact of angled illumination is such that the image obtained at the detector plane corresponds to a shifted region of the object spectrum, as illustrated in Figure 2.3.2.

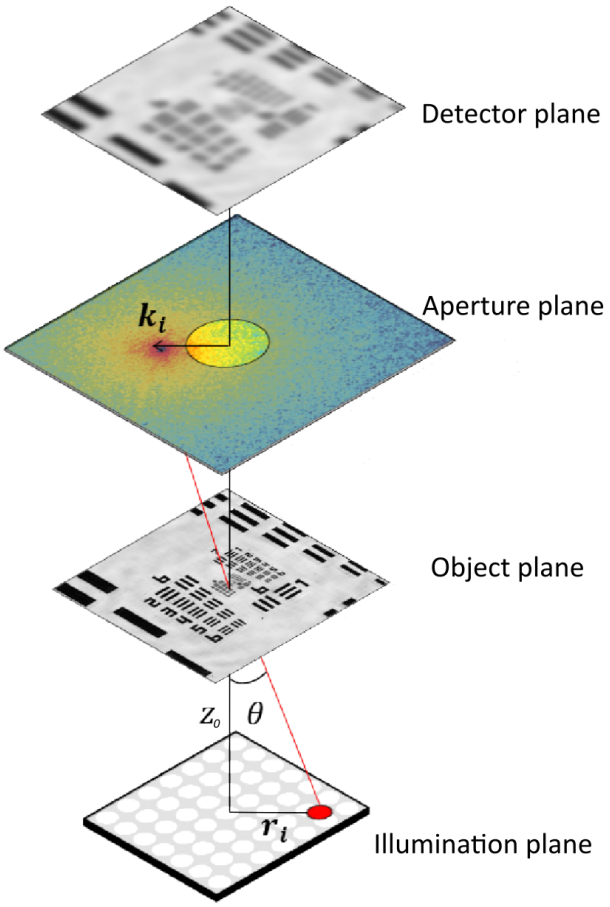

Figure 2.3.2: The impact of an illumination source at an angle θ compared to the optical axis. The angle depends on the distance z_0 and the position $\boldsymbol{r_i} = (\chi_i, \psi_i)$ of the illumination source within the illumination plane. At the aperture plane, the angled illumination results in a shift $\boldsymbol{f_i} = \boldsymbol{k_i}/2\pi$ of the object spectrum zero frequency. At the aperture plane, only the light within a region close to the optical axis passes through the AS and is propagated to the detector. At angled illumination, the image at the detector thus corresponds to a different part of the object spectrum as compared to direct illumination. Modified version of figure 1 in [5], licensed under CC BY 4.0.

2.3.2 Impact of LED illumination for an off-axis region

The above derivation assumes that the region under consideration is centered at the optical axis, a condition which is not necessarily satisfied for the purposes of FP[1]. In this section, a novel derivation of the frequency shift based on a wave-optical treatment within the Fresnel approximation will be provided.

Staying within the confines of the model considered so far, the impact of changing the center of the region of interest away from the optical axis where $(\zeta, \eta) = (0, 0)$, may be expressed through a coordinate change

$$\zeta = \zeta' + \zeta_c \tag{2.59a}$$

$$\eta = \eta' + \eta_c \tag{2.59b}$$

with (ζ', η') defining the new coordinate system based on which the Fourier transform is to be performed and (ζ_c, η_c) defining the center of the region of interest relative the optical axis. This coordinate change may be found to change the frequency shift of the object spectrum.

Starting with the impact on the frequency shift calculated in the previous section, $(f_{xi}, f_{yi}) = (-\chi_i/\lambda z_0, -\psi_i/\lambda z_0)$, one may note that the shift is independent of ζ and η. Implicitly, the contribution from the exponential term in Equation 2.53 is expected to be unchanged. For a proper derivation, one may consider the change in the exponential term in Equation 2.53 upon the aforementioned coordinate change, yielding

$$\exp\left[-\frac{ik}{z_0}\left(\zeta\chi_i + \eta\psi_i\right)\right] = \exp\left[-\frac{ik}{z_0}\left(\zeta'\chi_i + \eta'\psi_i\right)\right] \cdot \exp\left[-\frac{ik}{z_0}\left(\zeta_c\chi_i + \eta_c\psi_i\right)\right] \tag{2.60}$$

where the final exponential may be ignored as it is constant for a given center shift (x_c, y_c) and LED position (χ_i, ψ_i) and thus vanishes upon intensity imaging. Applying the Fourier shift theorem as for Equation 2.57 then yields the expected frequency shift $(f_{xi}, f_{yi}) = (-\chi_i/\lambda z_0, -\psi_i/\lambda z_0)$, which is unchanged as compared to an on-axis region.

Considering the impact on the combined quadratic phase, one may find that the coordinate change gives rise to an additional frequency shift. Applying the coordinate change to Equation 2.55 yields

$$Q_c(\zeta, \eta) = \exp\left[\frac{ik}{2}\left(\frac{1}{z_0} + \frac{1}{z_q}\right)\left(\zeta^2 + \eta^2\right)\right] \tag{2.61}$$

$$= \exp\left[\frac{ik}{2}\left(\frac{1}{z_0} + \frac{1}{z_q}\right)\left((\zeta' + \zeta_c)^2 + (\eta' + \eta_c)^2\right)\right] \tag{2.62}$$

$$= \exp\left[\frac{ik}{2}\left(\frac{1}{z_0} + \frac{1}{z_q}\right)\left(\zeta'^2 + 2\zeta'\zeta_c + \zeta_c^2 + \eta'^2 + 2\eta'\eta_c + \eta_c^2\right)\right] \tag{2.63}$$

$$= Q_c(\zeta', \eta') \cdot Q_c(\zeta_c, \eta_c) \cdot \exp\left[ik\left(\frac{1}{z_0} + \frac{1}{z_q}\right)\left(\zeta'\zeta_c + \eta'\eta_c\right)\right] \tag{2.64}$$

where the final line contains the original quadratic phase term redefined to the new coordinate system $Q_c(\zeta', \eta')$, a constant which vanishes upon intensity imaging $Q_c(\zeta_c, \eta_c)$ and an exponential

$$\exp\left[ik\left(\frac{1}{z_0}+\frac{1}{z_q}\right)(\zeta'\zeta_c+\eta'\eta_c)\right]$$

which will give rise to a frequency shift. Applying the Fourier shift theorem to the above exponential and combining the result with the shift from the position of the illumination source yields a final frequency shift expression

$$f_{xi} = \frac{1}{\lambda}\left[\frac{\zeta_c-\chi_i}{z_0}+\frac{\zeta_c}{z_q}\right] \tag{2.65a}$$

$$f_{yi} = \frac{1}{\lambda}\left[\frac{\eta_c-\psi_i}{z_0}+\frac{\eta_c}{z_q}\right] \tag{2.65b}$$

accounting for the impact of evaluating an off-center region.

2.3.3 Comparison with the literature

In the literature, two separate methods have been employed to determine the shift of the object spectrum under angled illumination. In the original article pioneering the concept of FP by Zheng et al.[1], the frequency shift was expressed as

$$f_{xi} = \frac{1}{\lambda}\frac{\zeta_c-\chi_i}{\sqrt{(\zeta_c-\chi_i)^2+(\eta_c-\psi_i)^2+z_0^2}} \tag{2.66a}$$

$$f_{yi} = \frac{1}{\lambda}\frac{\eta_c-\psi_i}{\sqrt{(\zeta_c-\chi_i)^2+(\eta_c-\psi_i)^2+z_0^2}} \tag{2.66b}$$

found by viewing the incident light as a plane wave and determining the in plane frequency components. Later, an alternative shift calculation formula[4, 6]

$$f_{xi} = \frac{1}{\lambda}\left[\frac{\zeta_c-\chi_i}{z_0}+\frac{\zeta_c}{z_1}\right] \tag{2.67a}$$

$$f_{yi} = \frac{1}{\lambda}\left[\frac{\eta_c-\psi_i}{z_0}+\frac{\eta_c}{z_1}\right] \tag{2.67b}$$

has been proposed by Konda[4] based on a geometrical analysis of the thin lens system covered in subsection 2.2.5.

Comparing the latter with Equation 2.65 as found in this work, one may note that the two expressions are highly similar, with the only difference being that z_q is substituted with z_1. This may easily be explained by the more general nature of the expression found in this work, as $z_q = z_1$ would be correct for the specific system considered by Konda according to the derivations in subsection 2.2.5. Importantly, this demonstrates that the geometric approach made by Konda and the wave-optics based approach

considered in this work are consistent with each other. Further, the derivation provided in this work demonstrates a direct connection between the presence of a quadratic phase at the object plane and the frequency shift for an off-axis patch.

Compared to the former frequency shift formula by Zheng et al., the differences are more substantial. In particular, one may note the absence of the z_q dependent term and the fact that the denominator is given by the length $\sqrt{(\zeta_c - \chi_i)^2 + (\eta_c - \psi_i)^2 + z_0^2}$ rather than only z_0. For the two formulas to coincide, the system under consideration would have to be such that $z_q = \infty$ as for the lens systems considered in subsection 2.2.6 and subsection 2.2.7 while also satisfying $(\zeta_c - \chi_i), (\eta_c - \psi_i) << z_0$ corresponding to small illumination angles. With the added z_q dependency in the formula presented in this work, the new formula may be considered more general. However, as the derivations performed in this work assumes small angles, there is an open question as to which of the two formulas are more correct at larger illumination angles given that the system under consideration satisfies $z_q \approx \infty$. If the approach made by Zheng et al. is more correct at high illumination angles, an investigation into how the model derived in this work may be modified to be more correct is warranted and desirable.

2.4 Discretization of the imaging system

For the purposes of numerical recovery through FP, it will also be necessary to consider the impact of discretization upon the lens system and illumination models considered previously. While the complex field at the detector plane as given by Equation 2.17 is continuous and defined for all $u, v \in (-\infty, \infty)$, the images captured by the detector are limited by the detector pixels. In this project, the detector will be assumed to be symmetrical in both spatial directions so that the detector is defined by an $M \times M$ matrix of pixels whose centers are separated by a distance $\delta_{detector}$. Additionally, for the purposes of the FP recovery algorithm, it is common to upscale the pixel counts on the object side of the lens by an integer factor p in each direction[17]. By also taking the magnification $|K| = z_b/z_a$ as given by Equation 2.19 into account, the object will then be defined by a $pM \times pM$ matrix with pixel size[6]

$$\delta_{object} = \frac{\delta_{detector}}{p|K|} \tag{2.68}$$

while at the aperture plane, the correct pixel size in terms of spatial values is given by

$$\delta_{aperture} = \frac{\lambda z_b}{M\delta_{detector}} = \frac{\lambda z_a}{pM\delta_{object}} \tag{2.69}$$

for both the $pM \times pM$ and $M \times M$ matrix sizes[6].

However, the convention that is prevalent in the broader literature[1, 2, 5, 14, 17, 18, 19] is to treat the aperture plane in terms of the object's spatial frequencies $(f_x, f_y) = (x/\lambda z_a, y/\lambda z_a)$ yielding a pixel size

$$\delta_{freq} = \frac{1}{pM\delta_{object}} = \frac{|K|}{M\delta_{detector}} \tag{2.70}$$

or in terms of the corresponding wavevectors. Beneficially, this removes the z_a and z_b dependency. In particular, this becomes relevant when discretizing the pupil function and the object spectrum frequency shift at angled illumination. In the case of the pupil function, the alternative definition becomes

$$P(f_x, f_y) = \begin{cases} 1, & f_x^2 + f_y^2 \leq f_c^2 \\ 0, & f_x^2 + f_y^2 > f_c^2 \end{cases} \tag{2.71}$$

where the cutoff frequency is defined by $f_c = R/\lambda z_a$ which may be rewritten in terms of a numerical aperture $NA = \sin\theta \approx \tan\theta = R/z_a$ as is valid for small angles. In terms of the frequency shifts, working with spatial frequencies allows Equation 2.65 to be applied directly. Alternatively, to express these shifts in terms of spatial coordinates of the lens plane, Equation 2.65 may be multiplied by λz_a, while a division by the pixel size as given by Equation 2.70 allows it to be expressed in terms of pixels. Notably, working in spatial frequencies means that the need to know the values of z_a, z_b and R is replaced by a need to know only the magnification $|K|$ and the Numerical Aperture (NA), both of which are more readily available for commercial microscope objectives.

2.5 Contributions and place within the current state of lens modelling for Fourier Ptychography

In this chapter, an imaging model was presented from which intensity imaging under angled illumination is summarized through

$$I_i(u,v) = I_i(-|K|\zeta, -|K|\eta) = |\mathcal{F}\{\mathcal{P}(f_x,f_y)S(f_x-f_{xi},f_y-f_{yi})\}|^2 \tag{2.72}$$

where the object spectrum is given by

$$S(f_x,f_y) = \mathcal{F}\{Q_c(\zeta,\eta)o(\zeta,\eta)\} \tag{2.73}$$

corresponding to the Fourier transform of the complex object $o(\zeta,\eta)$ multiplied with a quadratic phase factor

$$Q_c(\zeta,\eta) = \exp\left[\frac{ik}{2}\left(\frac{1}{z_0}+\frac{1}{z_q}\right)(\zeta^2+\eta^2)\right] \tag{2.74}$$

and with

$$f_{xi} = \frac{1}{\lambda}\left[\frac{\zeta_c-\chi_i}{z_0}+\frac{\zeta_c}{z_q}\right] \tag{2.75a}$$

$$f_{yi} = \frac{1}{\lambda}\left[\frac{\eta_c-\psi_i}{z_0}+\frac{\eta_c}{z_q}\right] \tag{2.75b}$$

defining the illumination frequency shifts. Of particular importance is the effective object to AS distance z_q, which may be seen to impact both the quadratic phase factor at the object plane and the illumination frequency shifts.

When considering the thin lens system in subsection 2.2.5, as has been done previously within the FP literature[4, 5, 6], the generalized expression may be adapted by setting $z_q = z_1$. Compared to the previous works, the main contribution provided by this work is the wave optical derivation of the frequency shift for an off-axis region covered in subsection 2.3.2. This derivation is consistent with the geometrical approach provided by Konda[4], while additionally establishing the connection between the quadratic phase and the frequency shift for off-axis regions. Importantly, the application of this Fresnel propagation-based model for a thin lens has been shown to be a requirement for recovery of large or off-axis regions for thin lens systems, and systems of comparative behavior[4, 5, 6].

Further, Aidukas et al.[5] state that the contribution to the quadratic phase term from the lens should vanish for a telecentric lens, citing a derivation[12, p.59-61] for the bi-telecentric 4f-system considered in subsection 2.2.7. This is consistent with $z_q = \infty$ as obtained through the derivations in section 2.2, though the results obtained in this thesis add additional nuance. Specifically, it has been shown that $z_q = \infty$ is consistent with the property of object-side telecentricity, requiring the AS to be in the back focal plane of the first lens element. Conversely, the image-side properties in general, and specifically whether the system is image-side telecentric, has been shown to not impact the imaging equation since the phase at the detector vanishes upon intensity imaging.

For an object-side telecentric lens, one may further note that the necessary simplifications to arrive at the original imaging relation considered by Zheng, Equation 1.1, would only be that of plane wave illumination. This is in contrast to the thin lens system, for which one would have to model the propagation from the object to the AS within the Fraunhofer approximation to arrive at Zheng's model. Importantly, the derivations made in this thesis show that the Fresnel-based derivation made for the thin lens system, yields an improved model for precisely a thin lens system, or any system of comparative behavior. Specifically, applying the thin lens model to an object-side telecentric lens system would expectedly degrade the recovery quality. This is both due to the differing quadratic phase terms and due to the differing frequency shifts for off-axis regions.

Finally, adding to the existing models, this work has demonstrated that it is possible to construct two-lens imaging systems with arbitrary AS placements, as covered by subsection 2.2.8. For these systems, the value of z_q becomes dependent on the distance from the first lens to the AS a_1 according to

$$z_q = \left(\frac{1}{f_{L1}} - \frac{a_1}{f_{L1}^2} \right)^{-1} \tag{2.76}$$

allowing both positive, negative and infinite values for z_q.

CHAPTER 3

RECOVERY THROUGH FOURIER PTYCHOGRAPHY

This chapter will provide an overview of how Fourier Ptychography (FP) may be used to recover a highly resolved, complex image of an object. The chapter will start with a review of the initial FP algorithm in section 3.1, followed by the coverage of several modifications considered in later works. Particularly, this includes the necessary modifications to account for a quadratic phase at the object plane and to additionally correct for lens aberrations through recovery of the generalized pupil function. Finally, experimental considerations including system alignment and calibration, noise and the sampling requirements of the system will be covered.

3.1 The original Fourier Ptychography algorithm

As covered in the introduction, the assumptions made by Zheng et al.[1] in the initial article proposing the concept of FP correspond to the intensity I_i at the detector under illumination by the i-th LED being given by the relation

$$I_i(\boldsymbol{r}) = |\mathcal{F}\{\mathcal{P}(\boldsymbol{f})S(\boldsymbol{f} - \boldsymbol{f_i})\}|^2 \tag{3.1}$$

with the object spectrum given by

$$S(\boldsymbol{f}) = \mathcal{F}\{o(\boldsymbol{r})\} \tag{3.2}$$

differing from the model considered in chapter 2 by the absence of the quadratic phase at the object plane as defined by Equation 2.55. While the necessary correction to account for the presence of a quadratic phase will be covered in section 3.3, it will be omitted from the initial coverage of the FP recovery algorithm below. Additionally, one should note that the frequency shift $\boldsymbol{f_i}$ upon angled illumination depends on the behavior of the imaging system in question, as covered in section 2.3.

The recovery algorithm proposed by Zheng et al.[1] aims to achieve the inverse of Equation 3.1 and recover the object spectrum $S(\boldsymbol{f})$ based on captured intensity images I_i^c. For this purpose, FP relies on iterative phase retrieval[1], based on the idea that for the recovered spectrum $S_r(\boldsymbol{f})$, the imaging procedure in Equation 3.1 should produce the same intensity images as those that were captured, while an overlap of the intensity images in terms of their frequency content allows for the phase to be recovered. This is achieved through the following process:

1. Initialize the recovered spectrum $S_r(\boldsymbol{f})$
2. For each illumination angle i
   (a) Calculate the complex field just after transmission through the generalized pupil function based on the current recovered spectrum
   $$U_P = \mathcal{P}S_r(\boldsymbol{f} - \boldsymbol{f_i})$$
   (b) Calculate the complex field at the detector
   $$U_D = \mathcal{F}\{U_P\}$$
   (c) Update the amplitude to coincide with the corresponding captured intensity image
   $$U_D^{new} = \sqrt{I_i^c} \cdot \arg(U_D)$$
   (d) Calculate the corresponding complex field just after transmission through the generalized pupil function
   $$U_P^{new} = \mathcal{F}^{-1}\{U_D^{new}\}$$

(e) Update the recovered spectrum S_r in accordance with the relation

$$\mathcal{P}S_r^{new}(\boldsymbol{f} - \boldsymbol{f_i}) = U_P^{new}$$

3. Repeat step 2 until convergence or for N iterations

To finalize the procedure, the recovered object $o_r(\boldsymbol{r})$ is then retrieved according to

$$o_r(\boldsymbol{r}) = \mathcal{F}^{-1}\left\{S_r(\boldsymbol{f})\right\}. \tag{3.3}$$

3.2 Update order and initialization

The order through which the images are used to update the sample spectrum and the initialization must further be defined. Barring prior information about the aberrations in the system, the initialization may be done by setting the initial guess for the generalized pupil function equal to the pupil function while the recovered object spectrum is initialized as

$$S_{init}(\boldsymbol{f}) = \mathcal{F}\left\{o_{init}(\boldsymbol{r})\right\} \tag{3.4}$$

where o_{init} is an upsampled version of the intensity image corresponding to illumination by the central LED[2]. In terms of update order, it has been shown that ordering the images in terms of decreasing intensity or increasing illumination angle provides the best results[20].

3.3 Reintroducing the quadratic phase term

While the original FP algorithm does not consider the presence of a quadratic phase term at the object plane as given by Equation 2.55, such a phase term has later been reintroduced upon consideration of the thin lens system covered in subsection 2.2.5[4, 5, 6]. Since the phase term is restricted to the object plane, its reintroduction only affects the parts of the FP algorithm where the object plane is considered, namely during initialization and the final retrieval of the recovered object from the recovered object spectrum. To account for a quadratic phase term, the initialization of the recovered object spectrum must follow

$$S_{init}(\boldsymbol{f}) = \mathcal{F}\left\{o_{init}(\boldsymbol{r})Q_c(\boldsymbol{r})\right\} \tag{3.5}$$

while the recovered object must be retrieved as

$$o_r(\boldsymbol{r}) = \mathcal{F}^{-1}\left\{S_r(\boldsymbol{f})\right\}Q_c^*(\boldsymbol{r}), \tag{3.6}$$

rather than using the relations in Equation 3.3 and Equation 3.4.

3.4 Embedded Pupil Function Recovery

In addition to recovering the spectrum $S(\boldsymbol{f})$ as described previously, Ou et al.[2] further enhanced the algorithm to also allow for recovery of an unknown generalized pupil function $\mathcal{P}$. This enhanced algorithm is called Embedded Pupil Function Recovery (EPRY) and follows the same scheme as the original algorithm, except in step 2e where both the recovered spectrum S_r and the recovered pupil $\mathcal{P}_r$ are updated rather than only S_r. This update procedure is given by

$$S_r^{new}(\boldsymbol{f}-\boldsymbol{f_i}) = S_r(\boldsymbol{f}-\boldsymbol{f_i}) + \alpha\frac{\mathcal{P}^*}{|\mathcal{P}|^2_{max}}\left[U_P^{new}-U_P\right] \tag{3.7a}$$

$$\mathcal{P}^{new} = \mathcal{P} + \beta\frac{S_r(\boldsymbol{f}-\boldsymbol{f_i})}{|S_r(\boldsymbol{f}-\boldsymbol{f_i})|^2_{max}}\left[U_P^{new}-U_P\right] \tag{3.7b}$$

where $\alpha \leq 1$ and $\beta \leq 1$ are constants used to adjust the step size. Additionally, as the above update step for the pupil allows it to take on non-zero values above the cutoff frequency, these values are suppressed through multiplication by the pupil function.

3.5 Second order update steps

Further improvement upon the algorithm has since been made by instead applying a second order update step[21, 22] originating from the adjacent field of real space Ptychography[23]. Instead of Equation 3.7, the recovered object spectrum and recovered pupil is then updated according to

$$S_r^{new}(\boldsymbol{f}-\boldsymbol{f_i}) = S_r(\boldsymbol{f}-\boldsymbol{f_i}) + \alpha\frac{|\mathcal{P}|\mathcal{P}^*}{|\mathcal{P}|_{max}(|\mathcal{P}|^2+\delta_1)}\left[U_P^{new}-U_P\right] \tag{3.8a}$$

$$\mathcal{P}^{new} = \mathcal{P} + \beta\frac{|S_r(\boldsymbol{f}-\boldsymbol{f_i})|S_r(\boldsymbol{f}-\boldsymbol{f_i})^*}{|S_r(\boldsymbol{f}-\boldsymbol{f_i})|^2_{max}}\left[U_P^{new}-U_P\right] \tag{3.8b}$$

where δ_1 and δ_2 are regularization constants included to ensure numerical stability[21]. Specific values for the regularization constants which have been used in the literature are $\delta_1 = 1$ and $\delta_2 = 1000$[14, 18], which will be used in this work.

3.6 The normalized real space error

One of the error metrics that may be used to quantify the convergence of the algorithm is the normalized real-space error[24]. The error metric is given by

$$\varepsilon = \frac{\sum_i ||\sqrt{I_i^c} - |U_D|||^2}{\sum_i ||\sqrt{I_i^c}||^2} \tag{3.9}$$

where the sums are taken across all illumination angles i and $||.||$ denotes the Euclidean norm. Additionally, for application within the FP algorithm without added computational cost, the error metric may be approximated by accumulating the sum in the numerator of Equation 3.9 incrementally during the update step of each individual illumination angle.

3.7 System alignment and calibration

For the purposes of FP, proper system alignment is an important factor for high-quality reconstruction. In the literature, the focus has been on correcting for the placements of the LED array, either before the main algorithm loop[25, 26] or within it[14, 18, 25, 27]. The multitude of specific system calibration schemes proposed in the literature will not be considered further in this work.

To describe the placements of the individual LEDs, a rigid body model for the LED array is commonly employed[14, 18, 26, 27], with the LEDs being assigned indices n and m forming a grid where $(n, m) = (0, 0)$ denotes the center LED. In the idealized model, the LED coordinates (x_i, y_i) are then described by

$$x_i = dn \tag{3.10a}$$

$$y_i = dm \tag{3.10b}$$

where d is the spacing between adjacent LEDs in the array and the center LED is presumed to lie precisely along the optical axis. In the presence of an undesired rotation θ and translation $(\Delta x, \Delta y)$ of the LED array within the illumination plane, the misaligned positions may be described by

$$x_i = d(n\cos\theta + m\sin\theta) + \Delta x \tag{3.11a}$$

$$y_i = d(-n\sin\theta + m\cos\theta) + \Delta y \tag{3.11b}$$

which together with the distance z_0 are the necessary quantities to calculate the frequency shift at angled illumination using the formula proposed by Zheng et al.[1], Equation 2.66, and the contribution to the quadratic phase from spherical illumination, assuming that the magnification, wavelength, and detector pixel size are known. When considering a thin lens system, the distance z_1 is additionally required to calculate the quadratic phase and the frequency shift using the formula proposed by Konda, Equation 2.67. However, the value of z_1 may be obtained from the focal length and magnification according to Equation 2.27a, posing no additional problems. Finally, considering the generalized model discussed throughout section 2.2 and an objective of unknown behavior, it is necessary to determine the value of z_q. Since the value of z_q is not considered within existing calibration algorithms, use of the generalized imaging model justifies the need for a novel calibration procedure, as will be proposed in chapter 5.

3.8 Noise

The presence of noise in the captured intensity images may severely degrade the quality of the recovered object and pupil[19, 24, 28, 29]. In FP, noise may originate from several sources, including but not limited to LED intensity fluctuations[14, 19], background noise[28, 30], stray light[28] and inaccuracies of the model at the transition region from BF to Dark-Field (DF)[29]. To minimize the detrimental impact of these noise sources, corresponding noise reduction steps have been proposed through image preprocessing, by disregarding the images located at the BF-DF transition region within the algorithm and by implementation of an adaptive step size.

3.8.1 Adaptive step size

Improvement of the algorithm's performance in the presence of noise has been observed through modification of the step-size constants α and β used in Equation 3.7 and Equation 3.8. In the initial articles introducing FP[1] and EPRY[2], the step-size constants were set to 1, which is sufficient for perfect reconstruction in the absence of noise[24]. However, in the presence of noise it has later been shown that smaller values of α and β result in improved convergence at the cost of convergence rate[24]. To retain the benefits in convergence rate from large values of α and β, while also improving the convergence, Zuo et al.[24] proposed an adaptive step-size defined by

$$\alpha^k = \begin{cases} \alpha^{k-1} & \frac{\varepsilon^{k-1}-\varepsilon^k}{\varepsilon^{k-1}} > \eta \\ \alpha^{k-1}/2 & else \end{cases} \tag{3.12}$$

and likewise for β^k. Here, k corresponds to the number of iterations of the algorithm, η is a constant determining how rapidly the step-size is updated and ε is the real space error defined by Equation 3.9. In terms of values, $\eta = 0.01$, $\alpha^0 = 1$ and $\beta^0 = 1/\sqrt{N}$ where N is the number of low-resolution images, have been proposed as reasonable choices[24] in combination with the first order update steps considered in section 3.4. In combination with the second order update step covered in section 3.5, it appears that setting $\beta^0 = 1$ may be more suitable[14].

3.9 Sampling requirements

For the purposes of FP, sampling must be considered in both the frequency and spatial domains.

In the frequency domain, Dong et al.[31] found that at least a 35% overlap in the frequency content of images corresponding to illumination by adjacent LEDs is required. The frequency content for a single LED corresponds to a circle of diameter $D = 2NA/\lambda$, while application of Equation 2.65 yields a difference in the frequency shift for two adjacent LEDs separated by a distance d as $\Delta f = d/(\lambda z_0)$. Considering two circles with the given diameter D and separation Δf, the overlap O may be found as[32]

$$O = \begin{cases} \frac{2}{\pi}\left\{\arccos(X) - X\sqrt{1-X^2}\right\}, & X < 1 \\ 0, & else \end{cases} \tag{3.13}$$

with $X = \Delta f/D = d/(2z_0 NA)$.

In the spatial domain, requirements are placed on both the sampling rate of the detector and on the sample rate of the recovered object[17, p.2-20]. For the detector, the Nyquist sampling theorem yields that the detector pixel size must satisfy[17, p.2-20]

$$\delta_{detector} < \frac{|K|\lambda}{2NA} \tag{3.14}$$

placing restrictions on the ratio between the magnification $|K|$ and the numerical aperture NA for a given detector. For the recovered object, the pixel size must satisfy[17, p.2-20]

$$\delta_{object} < \frac{\lambda}{4(NA + NA_{illum})} \tag{3.15}$$

to sufficiently resolve the recovered intensity, with NA_{illum} being the numerical aperture equivalent of the largest illumination frequency shift,

$$NA_{illum} = \left(\lambda\sqrt{f_{xi}^2 + f_{yi}^2}\right)_{max} . \tag{3.16}$$

In turn, this places a restriction upon the pixel scale factor

$$p > \frac{4\delta_{detector}(NA + NA_{illum})}{|K|\lambda} . \tag{3.17}$$

CHAPTER 4

INTRODUCTION TO ABERRATION THEORY

The aim of this chapter will be to give a brief introduction to the theory of monochromatic aberrations. To this extent, a description of the wavefront aberration and the first order Seidel aberrations will be provided in section 4.1, including spherical aberration, coma, astigmatism, field curvature and distortion. Additionally, the Zernike polynomials and their applications regarding the description of optical aberrations will be considered. Further, section 4.2 will provide a derivation of the expected phase change at the aperture plane upon defocus for the generalized imaging system considered in chapter 2. Finally, a review of the aberrations and other effects which may be expected to appear upon imaging through a glass window will be provided in section 4.3. In general, the following sections will be based upon the work of Welford as presented in "Aberrations of optical systems"[33]. To supplement the discussion, the works of Geary[16], Wyant and Creath[34] and Song et al.[35] will be used.

4.1 Monochromatic aberration theory

Within the context of the model developed in chapter 2 based on monochromatic wave optics, aberrations may be described through the phase

$$\phi = kW(x, y) \tag{4.1}$$

of the generalized pupil function as defined in subsection 2.1.3[8, p.205][16, p.82]. This phase is dependent on the wavevector k and the wavefront aberration W, and may be considered as a deviation of the imaging system from the ideal case where the phase would be zero. In general, the presence of aberrations results in reduced image quality, either in the form of point imaging aberrations or by affecting the image shape[33, p.92]. In the presence of a point imaging aberration, a point at the object plane would yield a distorted or blurry point at the detector, while retaining its expected location. This includes several well-known aberrations, including spherical aberrations, coma, and astigmatism. Conversely, the presence of an aberration which affects the image shape would alter the location of the image point, which is the case for the aberrations known as distortion and field curvature. Finally, one may note that there exist aberrations originating from the wavelength dependency of the refractive index[33, p.93], referred to as chromatic aberrations, as opposed to monochromatic aberrations, though these aberrations will not be considered in this work.

4.1.1 Expansion of the wavefront aberration

For a formal treatment of aberrations within the confines of wave optics, Welford considers the expansion of the wavefront aberration as a function of the coordinates (x, y) and (ζ, η) at respectively the aperture and object planes[33, p.105-108]. Requiring that the combinations of the four variables (x, y, ζ, η) present in the final expression are invariant under rotation, the four variables are reduced to three combinations $(x^2 + y^2, x\zeta + y\eta, \zeta^2 + \eta^2)$. From this point, the wavefront aberration function may be expanded directly, as is done by Song et al.[35]. However, to further simplify the expression, Welford[33, p.106] applies an argument based on the symmetry of the system to only consider an object point along the η-axis, with $\zeta = 0$, and choose to represent the system in a way such that W should be zero at the center of the aperture plane. This yields a final expansion[33, p.107]

$$\begin{aligned} W(x, y, \eta) &\equiv W(x^2 + y^2, y\eta, \eta^2) \\ &= a_1(x^2 + y^2) + a_2 y\eta \\ &\quad + b_1(x^2 + y^2)^2 + b_2 y\eta(x^2 + y^2) \\ &\quad + b_3 y^2\eta^2 + b_4\eta^2(x^2 + y^2) + b_5 y\eta^3 \\ &\quad + \text{third and higher order terms} \end{aligned} \tag{4.2}$$

with the constant and (x, y)-independent terms assumed equal to zero.

The first order terms with coefficients a_1 and a_2 are not considered to represent proper imaging aberrations[33, p.107] and will not be considered further here, though the first term may be recognized as a defocus as will be considered in section 4.2.

The second order terms are referred to as the primary aberrations or the Seidel aberrations[33, p.109.129], and constitute respectively primary spherical aberration, primary coma, primary astigmatism, field curvature and distortion.

4.1.2 Spatial dependency of the aberration modes

Disregarding the higher order modes, which may be found in [35], one may note that the different aberrations vary in their dependency on the distance from the optical axis at the object plane, as given by η. Considering only the terms in Equation 4.2, the dependency of the spherical aberration term is constant, the coma term is linear, and the astigmatism term is quadratic. Likewise, the field curvature term may be recognized as a defocus term scaling with the square of η. As emphasized by Wyant and Creath[34, p.35], this spatial dependency is lost when the wavefront aberration is considered only as a function of (x, y) as is the case for the generalized imaging model considered in chapter 2.

4.1.3 Zernike polynomials

An alternative to the expansion in Equation 4.2, is to expand the phase of the generalized pupil function as a linear combination of Zernike polynomials

$$kW(x, y) = \sum_{j=1}^{\infty} a_j Z_j(x, y) \tag{4.3}$$

with j denoting the indices of the Zernike polynomial terms Z_j and the corresponding expansion coefficients a_j, which will be referred to as the Zernike coefficients. Importantly, the Zernike polynomials are defined such that they form an orthogonal basis over a unit disk, allowing for easy numerical treatment and making them easily applicable to the wavefront aberration[36]. For further context, a short review of the Zernike polynomials is provided in Appendix C.

4.2 Consequence of an object-side defocus

It may be shown that all the systems considered in section 2.2 have the same expected behavior in terms of the phase at the aperture plane in response to an object-side defocus. Defining an object-side defocus as a change in the location of the object along the optical axis, the quadratic phase at the aperture plane due to an object-side defocus may be found by comparing the z_1 dependent contribution between a value $z_1 = z_1'$ at focus and a value $z_1 = z_1' + \Delta z_1$ with Δz_1 denoting the defocus distance. As will be shown, the necessary derivations differ depending on whether Equation 2.15 or Equation 2.16 is used for the front half of the generalized system. For the front half, the values d_1 and d_2 in the aforementioned equations become respectively z_1 and a_1.

If Equation 2.16 is used, the difference becomes

$$\begin{aligned} D(x,y) &= \exp\left[\frac{ik}{2}\left(-\frac{z_1'+\Delta z_1}{a_1^2}+\frac{z_1'}{a_1^2}\right)\left(x^2+y^2\right)\right] \\ &= \exp\left[\frac{ik}{2}\left(-\frac{\Delta z_1}{a_1^2}\right)\left(x^2+y^2\right)\right] \\ &= \exp\left[\frac{ik\lambda^2}{2}\left(-\Delta z_1\right)\left(f_x^2+f_y^2\right)\right] \\ &= \exp\left[-i\pi\lambda\Delta z_1\left(f_x^2+f_y^2\right)\right] \end{aligned} \tag{4.4}$$

with the second equality being dependent on the relation $(f_x, f_y) = (u/\lambda a_1, u/\lambda a_1)$ and the third upon the definition $k = 2\pi/\lambda$. This derivation is inspired by and may be found to be consistent with the derivation performed by Goodman[8, p.207-208].

When considering Equation 2.15, it is additionally necessary to assume that $\Delta z_1 << z_1' + \Delta z_1$ so that the Taylor expansion $1/(z_1'+\Delta z_1) = 1/z_1' - \Delta z_1/(z_1')^2$ may be applied. This yields the difference

$$\begin{aligned} D(x,y) &= \exp\left[\frac{ik}{2}\left(\frac{1}{z_1'+\Delta z_1}-\frac{1}{z_1'}\right)\left(x^2+y^2\right)\right] \\ &\approx \exp\left[\frac{ik}{2}\left(-\frac{\Delta z_1}{(z_1')^2}\right)\left(x^2+y^2\right)\right] \\ &\approx \exp\left[\frac{ik\lambda^2}{2}\left(-\Delta z_1\right)\left(f_x^2+f_y^2\right)\right] \\ &= \exp\left[-i\pi\lambda\Delta z_1\left(f_x^2+f_y^2\right)\right] \end{aligned} \tag{4.5}$$

recognizing that $(f_x, f_y) = (u/\lambda z_1, u/\lambda z_1) \approx (u/\lambda z_1', u/\lambda z_1')$ for Equation 2.16.

As shown, both the alternatives for propagation between the object and aperture planes considered in section 2.2 yield the same behavior for a small defocus $\Delta z_1 << z_1$. A similar consideration could be made regarding an image-side defocus or for the quadratic phase terms at the object plane, but will not be considered in this work.

In terms of the Zernike polynomials, the defocus aberration is primarily contained within the fourth term[36]

$$Z_4(x, y) = \sqrt{3}[2(\tilde{x}^2 + \tilde{y}^2) - 1] \tag{4.6}$$

with $(\tilde{x}, \tilde{y}) = (f_x/f_c, f_y/f_c) = (f_x\lambda/NA, f_y\lambda/NA)$ being the normalized coordinates of the aperture plane such that $(\tilde{x}^2 + \tilde{y}^2) \leq 1$ within the area defined by the AS. From this, the expected Zernike coefficient for a given Δz_1 is

$$a_4 = \frac{-\pi\Delta z_1 NA^2}{2\sqrt{3}\lambda} \tag{4.7}$$

and inversely

$$\Delta z_1 = \frac{-2\sqrt{3}\lambda a_4}{\pi NA^2} \tag{4.8}$$

given that the Zernike polynomials are used to expand the phase $kW(x, y)$ of the generalized pupil function $\mathcal{P}$ and disregarding any contribution to higher order Zernike terms on the form x^2+y^2. Notably, the Zernike coefficient for a given defocus distance scales with the square of the numerical aperture, corresponding with a decreased DoF for higher NA lenses.

4.3 Impact of imaging through a window

As the process of imaging through a window will be considered experimentally later in this work, a dedicated summary of the expected theoretical behavior will be provided here. While Welford[33, p.234-235] provides a brief review on windows, the issue is covered more in-depth by Geary[16, p.253-258] and Wyant and Creath[34, p.40-46] whose work will be considered further. For the purposes of the following sections, a window may be defined as a parallel plate of refractive index n and thickness t. Furthermore, only the case where the propagation media outside of the window is air will be considered, with any adverse effects originating from refraction at the two air-material boundaries. In particular, the following expressions describe the impact of a window upon a converging beam of half angle u.

Assuming that the window and chief ray of the incident wavefield is parallel to the optical axis, the window may be expected to introduce a defocus and spherical aberration. The expected defocus may be found such that[16, p.253-255][34, p.41]

$$\Delta z = \left(\frac{n-1}{n}\right) t \tag{4.9}$$

denotes the effective increase in the distance at which optimal focus is expected to be achieved. In terms of the spherical aberration, the corresponding wavefront aberration is expected to be given as[34, p.43]

$$\Delta W_{sph} = -\frac{Nu^4 t}{2}(\tilde{x}^2 + \tilde{y}^2)^2 \tag{4.10}$$

with $(\tilde{x}, \tilde{y})$ being the normalized coordinates of the aperture plane as in the previous section and with

$$N = \frac{n^2 - 1}{n^3} \tag{4.11}$$

containing the dependence on the refractive index. Considering only the $(\tilde{x}^2 + \tilde{y}^2)^2$ dependency of the eleventh Zernike term[36]

$$\sqrt{5}(6(\tilde{x}^2 + \tilde{y}^2)^2 - 6(\tilde{x}^2 + \tilde{y}^2) + 1) \tag{4.12}$$

the corresponding Zernike coefficient becomes

$$a_{11} = -\frac{\pi u^4 N t}{6\sqrt{5}\lambda} \tag{4.13}$$

given that the Zernike polynomials are used to expand $kW(x, y)$ as in Equation 4.3.

Following Wyant and Creath[34, p.43], one may note that N increases for $n < \sqrt{3}$, is maximized at $n = \sqrt{3}$ and decreases toward zero for $n > 3$ as $n \to \infty$.

Further effects are expected if the window, or the chief ray of the incident wavefield, has an angle $\bar{u}$ as compared to the optical axis. In both cases, additional coma, astigmatism, and distortion is expected, scaling with respectively $Nu^3\bar{u}$, $Nu^2\bar{u}^2$ and $Nu\bar{u}^3$[16, p.257][34, p.44-45]. Additionally, upon a tilt of the window, one would expect a lateral displacement of the beam approximately equal to $\bar{u}\Delta z$[34, p.42].

CHAPTER 5

NOVEL CALIBRATION PROCEDURE

As a part of this thesis, a novel parameter calibration procedure will be proposed. The procedure will be referred to as Non-linear Bright-Field Localization (NBFL), as it aims to calibrate the system from the size and location of the Bright-Field (BF) region by means of non-linear optimization. The procedure innovates upon the work of Zhang et al.[27], and consists of two main steps: the first being localization of points along the edge of the BF region and the second being the application of non-linear optimization to fit said points to a theoretical expression which will be derived in section 5.1. To account for any offset or rotation of the LED array, the LED positions will be assumed to follow the rigid body model considered in section 3.7. The procedure is intended to be applied to FP datasets obtained in the absence of a sample, and may either be used to calibrate the placement of the LED array as given by the parameters Δx, Δy, θ and z_0 or to additionally calibrate for the Numerical Aperture (NA) and the potentially unknown value of the effective object to aperture distance z_q.

5.1 Origin of the Bright-Field region

As the basis for the proposed calibration method, a theoretical derivation explaining the origin of the BF, the DF and the transition between the two regions will be made.

Within previous works on FP, the connection between a quadratic phase at the detector plane as given by Equation 2.55 and the appearance of combined BF-DF images have been covered[4, 29]. In the absence of the quadratic phase term, the images obtained at angled illumination are explicitly either BF or DF images, determined based on whether the zero-frequency of the shifted object spectrum passes through the AS of the lens system[4, p.69-72]. However, following the derivations in subsection 2.3.2, the presence of a quadratic phase term results in a spatially varying frequency shift. As such, whether a given region of the FoV is part of the BF is determined based on whether the locally defined frequency shift is such that the zero-frequency of the shifted object spectrum passes through the AS, giving rise to a BF circle and creating mixed BF-DF images[4, p.71].

For a thin lens system, Figure 5.1.1 show how the origin of the BF for each LED may be illustrated by tracing the rays passing through the AS. For the points at the object plane, the rays radiating from the LED source locally correspond to the zeroth diffraction order according to the geometrical frequency shift derivation by Konda[4, p.71]. If these rays pass through the AS, the corresponding points at the object plane may thus be expected to be a part of the BF in line with the argument presented in the previous paragraph. This ray optical approach yields the same results as the simulations based on Equation 2.17, as demonstrated by comparison of Figure 5.1.1a and Figure 5.1.1b.

For a derivation based on wave optics, the image coordinates corresponding to the coordinates (ζ, η) at the object plane are part of the BF if the magnitude of the locally defined frequency shift is less than the cutoff frequency $f_c = NA/\lambda$. That is, if

$$f_{xi}^2 + f_{yi}^2 \leq f_c^2 \,, \tag{5.1}$$

with the frequencies being given by Equation 2.65 upon the substitution $(\zeta_c, \eta_c) = (\zeta, \eta)$. This yields a relation for the edge of the BF region

$$\left[\frac{\zeta - \chi_i}{z_0} + \frac{\zeta}{z_q}\right]^2 + \left[\frac{\eta - \psi_i}{z_0} + \frac{\eta}{z_q}\right]^2 = NA^2 \,, \tag{5.2}$$

which may be recognized as a circle of center coordinates and radius

$$\zeta_{BF} = \frac{\chi_i}{1 + \frac{z_0}{z_q}} \,, \qquad \eta_{BF} = \frac{\psi_i}{1 + \frac{z_0}{z_q}} \,, \qquad R_{BF} = \left|\frac{NAz_0}{1 + \frac{z_0}{z_q}}\right| \tag{5.3}$$

according to $(\zeta - \zeta_{BF})^2 + (\eta - \eta_{BF})^2 = R_{BF}^2$.

The results of a simple simulation verifying the above expression may be found in Figure 5.1.2.

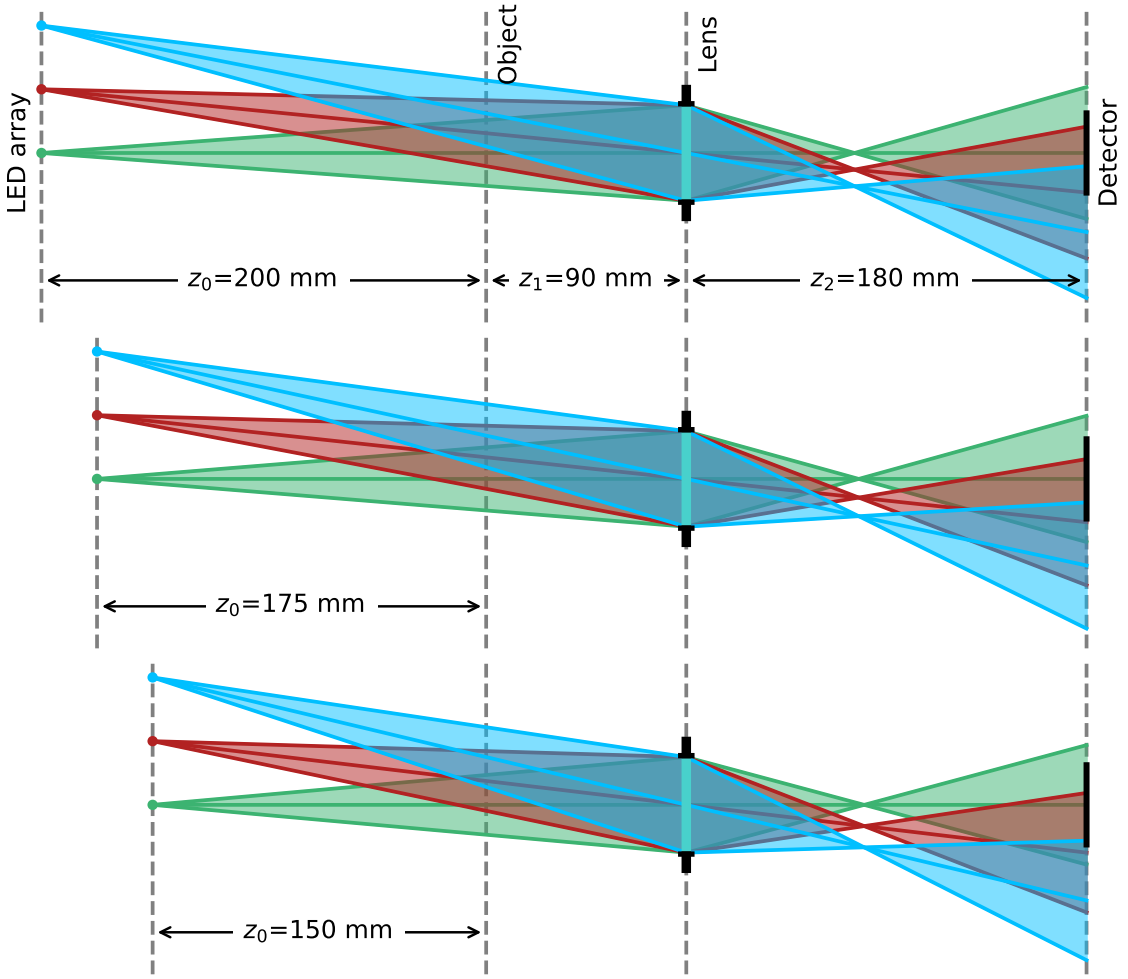

(a) Formation of the BF region for a thin lens system

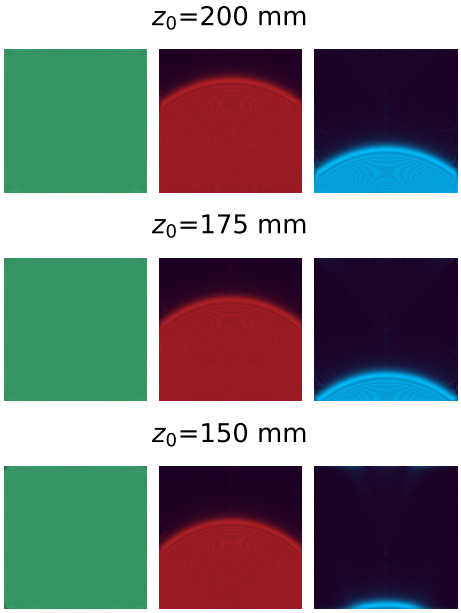

(b) Corresponding simulated BF images

Figure 5.1.1: (a) provides a ray optical illustration of the formation of the BF region for a thin lens imaging system. The drawn system corresponds to parameters $|K| = 2$, $NA = 0.05$, $f_L = 60\,\text{mm}$ and a detector FoV of $7.8\,\text{mm} \times 7.8\,\text{mm}$ illustrated by the black region at the image plane. Notably, the y- and z-axes are not to scale. The imaging system is drawn thrice, and show the BF regions formed under spherical illumination by each of three LEDs at different illumination distances z_0. The green LED is located at the optical axis, while the red and blue LEDs are respectively placed 6 and 12 mm away from the optical axis. (b) show corresponding simulations of the BF region performed according to Equation 2.17. The ray diagrams and the simulations yield consistent results.

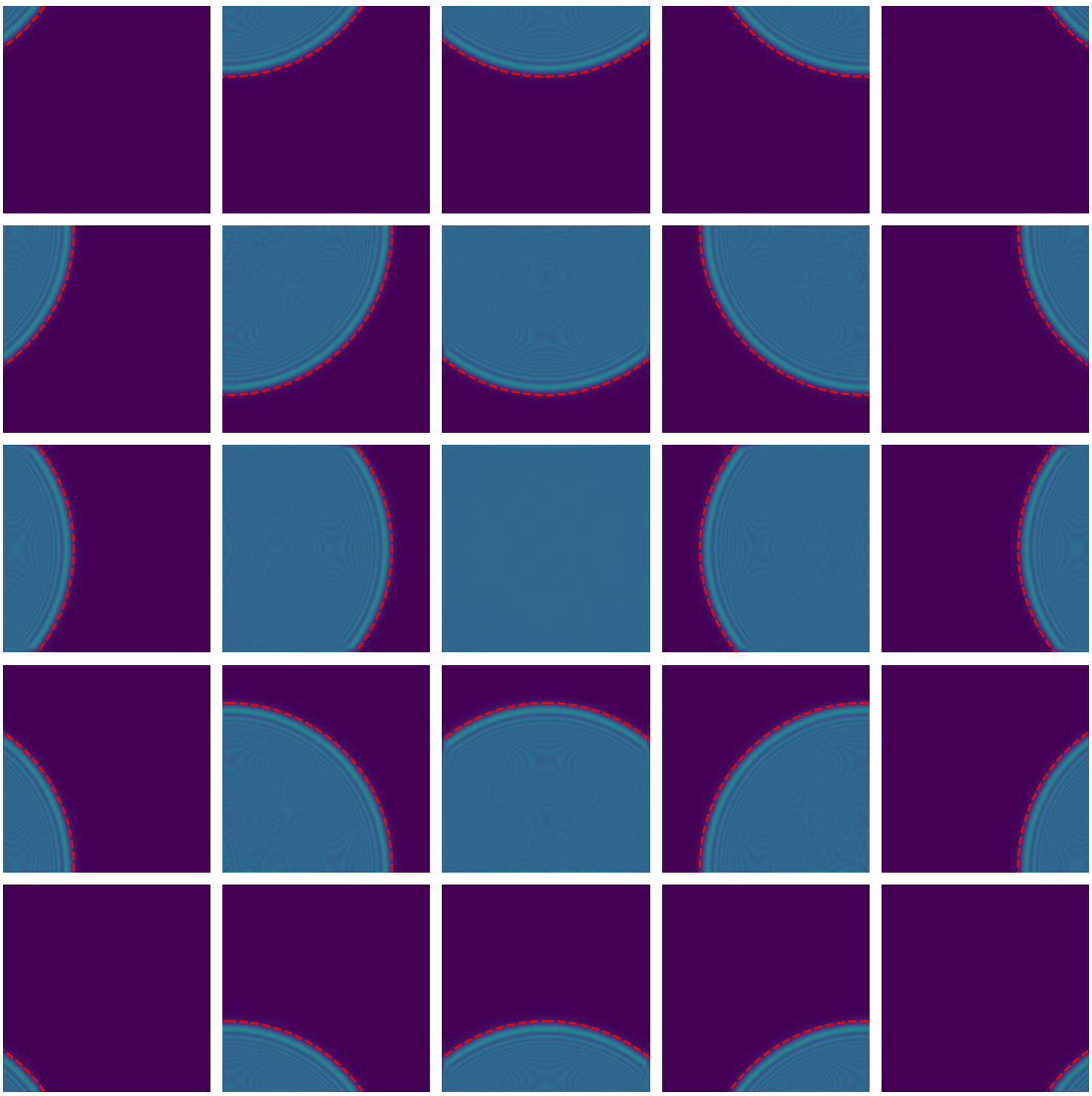

Figure 5.1.2: A simulation of the BF region in the presence of a quadratic phase with the dotted red line corresponding to the BF edge, as given by Equation 5.3. The simulation is performed according to Equation 2.17 with parameters corresponding to a lens with $|K| = 2$, $NA = 0.05$ and $z_q = 90\,\text{mm}$, and a $7.8\,\text{mm} \times 7.8\,\text{mm}$ detector FoV. This is the same system as is considered in Figure 5.1.1. The 25 images correspond to spherical illumination from LEDs in a square grid of 6 mm spacing centered at the optical axis at a distance $z_0 = 200\,\text{mm}$ from the object plane. For this particular case, the central LED may be seen to produce an image entirely inside the BF region, while a circular BF region may be observed in the remaining images. As predicted by Equation 5.3 the BF region is of constant radius, with the center moving away from the optical axis corresponding to the positions of the illumination sources.

Combining the expressions for the radius and center of the BF circle as given by Equation 5.3 with the rigid body model for calculating the LED positions as given by Equation 3.11, the equations

$$\zeta_{i,BF} = \frac{d(n\cos\theta + m\sin\theta) + \Delta x}{1 + \frac{z_0}{z_q}} \tag{5.4a}$$

$$\eta_{i,BF} = \frac{d(-n\sin\theta + m\cos\theta) + \Delta y}{1 + \frac{z_0}{z_q}} \tag{5.4b}$$

$$R_{BF} = \left| \frac{NAz_0}{1 + \frac{z_0}{z_q}} \right| \tag{5.4c}$$

are obtained, with i denoting the image in question and being assumed to map to corresponding values of n and m. Through this equation, the BF circle is defined by the intrinsic properties of the LED array through n, m and d, its placement through Δx, Δy, θ and z_0 and the properties of the imaging system through the numerical aperture NA and the value of z_q. Additionally, the magnification of the system and the pixel size of the detector is required to establish and convert between image and object space coordinates. For the purposes of the proposed calibration procedure, the magnification of the imaging system, the pixel size of the detector and the intrinsic properties of the LED array will be assumed known. Under these assumptions, the shape and size of the BF region in the captured intensity images depends solely on the values Δx, Δy, θ, z_0, NA and z_q, which the proposed calibration procedure will aim to retrieve.

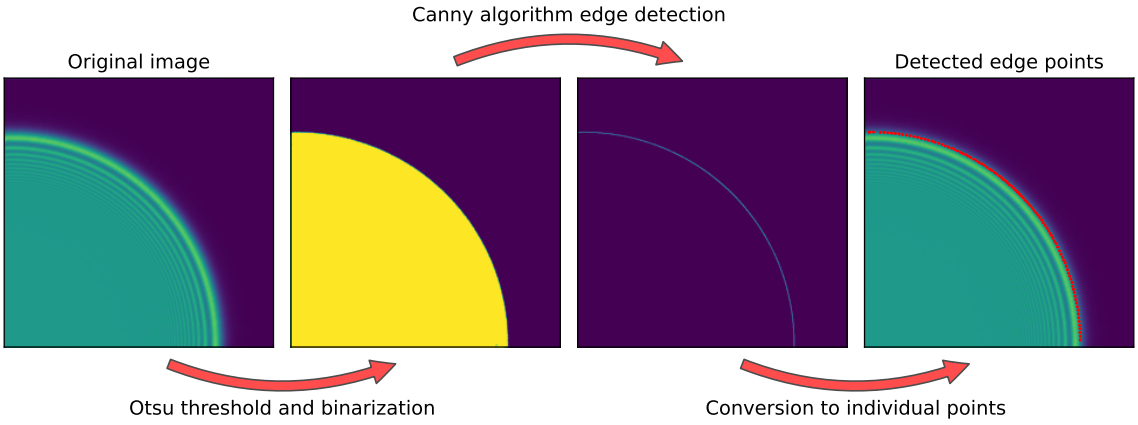

Figure 5.1.3: Figure illustrating the scheme used to localize points along the BF edge, as applied to one of the images from Figure 5.1.2. The scheme starts with a raw FP dataset obtained in the absence of a sample, leaving only the BF region. The Otsu algorithm is then applied to determine a suitable threshold, which is used to binarize the images. Using the Canny algorithm, an image corresponding to the edge between the bright and dark regions of the binarized image is found, which is then converted to an array of individual points. As illustrated, the located edge points are in agreement with the visually observed BF edge.

5.2 Localization of points along the Bright-Field edge

The first main step of the proposed calibration algorithm is the localization of the BF edge. Following Zhang et al.[27] this may be done through application of the Otsu algorithm to binarize the image, followed by edge detection by means of the Canny algorithm. The result of this procedure is displayed in Figure 5.1.3 as applied to one of the images of the simulated BF dataset shown in Figure 5.1.2.

5.3 Parameter estimation procedure by Zhang et al.

While the parameter estimation procedure which will be proposed in this work deviates substantially from the original work by Zhang et al.[27], a short review of their procedure may be of interest. The procedure aims to calibrate the placement of the LED array through the parameters Δx, Δy, θ and z_0, to which extent it applies the Particle Swarm Optimization (PSO) and Random Sample Consensus (RANSAC) algorithms. The application of PSO corresponds to an outer loop optimizing the value of θ, for each value of which the edge points are projected to a shared plane where they for the correct θ are expected to form an ideal circle. Based on this projection, an inner loop based on RANSAC optimizes Δx, Δy, and z_0. In the inner loop, guesses for the center and radius of the circle which best fits the projected edge points are found based on the circles defined by random selections of three edge points. Each guess is then assigned a score based on the number of edge points located within a certain distance from the circumference of the guessed circle, from which the optimal parameter values are found based on maximization of the score. However, in light of the generalized imaging system as presented in chapter 2 the approach by Zhang et al. becomes insufficient as it makes assumptions which equate to setting z_q as infinity.

5.4 Non-linear Bright-Field Localization

The alternative procedure proposed in this thesis approaches the issue of parameter estimation through the application of non-linear optimization. Since the edge points located from the raw images are known to be at the circumference of the BF circle, one may establish a cost function

$$C(\Delta x, \Delta y, \theta, z_0, z_q, NA) = \sum_i \sum_{e=1}^{E_i} \frac{\left| \sqrt{(\zeta_{i,e} - \zeta_{i,BF})^2 + (\eta_{i,e} - \eta_{i,BF})^2} - R_{BF} \right|^2}{E_i} \tag{5.5}$$

with i running over the BF images to which the procedure is applied, e running over the E_i edge points found for each image and $(\zeta_{i,e}, \eta_{i,e})$ being the object space coordinates corresponding to each edge point. To some extent, this cost function is an empiric

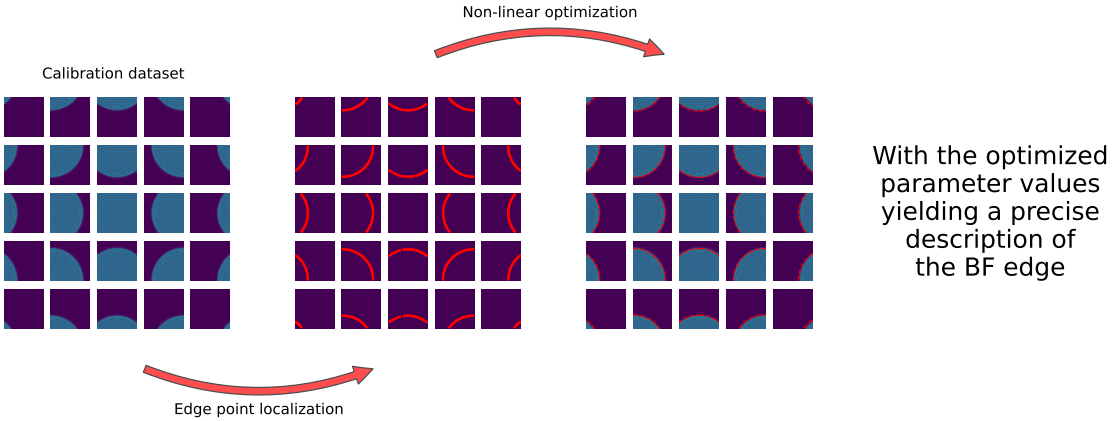

Figure 5.4.1: Overview of the proposed calibration procedure. The procedure may be used for parameter estimation based on a single calibration dataset obtained in the absence of a sample, including all the images which contain a part of the BF region. The parameter estimation is achieved by first locating the points along the BF edge, after which non-linear optimization is applied to optimize the parameters through minimization of the cost function given by Equation 5.5. If a precise estimate for the calibration parameters is obtained, the calibrated parameters should yield a precise description of the BF edge.

fabrication, both in terms of deciding to summarize the square of the distance from the circumference and the normalization by the number of edge points per image. In particular, the latter is intended to ensure that all images are weighted equally despite a large variance in the number of detected edge points based on how the FoV and the BF circle overlaps. Notably, any images where no edge points are found are not included in the summation. Combining the cost function with the edge points found through the edge point localization scheme covered in section 5.2, one may apply a non-linear optimization algorithm to determine the optimal values of the parameters in question, as illustrated in Figure 5.4.1. Additionally, it will be necessary to define the term *calibration dataset*, which will be used to refer to the complete set of images containing a part of the BF region, when imaging is performed with no sample placed in the object plane. Finally, one should note that NA, z_q and z_0 are not independent of each other in terms of how they affect the center and radius of the BF circle.

5.4.1 Calibration of LED array placement

If one assumes that NA and z_q are known, the aforementioned problem is avoided, and the non-linear optimization may be applied to optimize solely the placement of the LED array through the parameters Δx, Δy, θ and z_0. This application requires only a single calibration dataset obtained in the absence of a sample. By obtaining the calibration dataset immediately after obtaining a dataset of a sample, the calibrated parameters may be used to correct for misalignment of the LED array during recovery of the sample dataset. Through this application, the calibration procedure may be

used as an alternative to other calibration schemes, with the important distinction being that it is applicable for systems with any value of z_q, given that it is known.

5.4.2 Calibration of lens parameters

Alternatively, the procedure may be applied for calibration of the numerical aperture NA and the effective object to AS distance z_q for a given objective lens. For this application, one must address the dependency between the parameters z_0, NA and z_q in terms of how they affect Equation 5.4. One potential solution, which will be used in this work, is to combine the parameters into two dependent parameters $(z_0, z_q, NA) \rightarrow (NAz_0, z_0/z_q)$. Using the dependent parameters, the non-linear optimization may be applied to optimize the values of Δx, Δy, θ, NAz_0 and z_0/z_q for each of several calibration datasets obtained at known relative values of z_0. Since both the dependent parameters are linear with z_0, the original parameters may be retrieved from the slopes and intercepts of the dependent parameters as obtained through linear regression. Specifically, defining the unknown value of z_0 for one of several measurements as z' and assuming that each measurement corresponds to a known translation z from said measurement, the two dependent parameters are expected to follow the linear relations

$$(NAz_0) = NA(z' + z) = NA \cdot z + NA \cdot z' \tag{5.6a}$$

$$\left(\frac{1}{z_q} z_0\right) = \frac{1}{z_q}(z' + z) = \frac{1}{z_q} \cdot z + \frac{1}{z_q} \cdot z' \,, \tag{5.6b}$$

both of which are on the form

$$f(z) = az + b \tag{5.7}$$

with a being the slope and b being the intercept. Further, recognizing that either the edge detection algorithm may fail to locate the correct edge or that the non-linear optimization may fail to converge, additional filtering may be prudent before linear regression is performed. This may be done by comparing the value of the cost function between measurements, assuming that measurements where the edge detection or optimization fails would have comparatively high costs.

CHAPTER 6

EXPERIMENTAL IMPLEMENTATION

This chapter will provide a short review of the experimental implementation used to generate the results which will be covered in chapter 8, chapter 9 and chapter 10. To this extent, section 6.1 and section 6.2 will describe respectively the microscope setup and samples considered in this thesis, while section 6.3 will consider the computational implementations of a FP processing pipeline and the calibration scheme proposed in chapter 5.

6.1 Microscope setup

The microscope setup used in this project is illustrated in Figure 6.1.1, with the main components being a LED array, a camera, an objective lens and a sample holder. The objective lens was connected to the camera using an extension tube, ensuring correct alignment between the lens and the detector plane, as well as ensuring a correct value for the detector to lens distance z_2. Both the camera and the attached objective lens were placed on a translation stage, allowing manual translation orthogonal to the optical axis and motorized control along the optical axis for alignment and focusing purposes. The entire microscope setup was mounted on an optical table, allowing the LED array to object distance z_0 to be changed easily. For this project, a IDS U3-31J0CP-M-GL Rev.2.2 industrial camera[37] and a RGB LED board (SparkFun, part #14646) controlled by an Arduino Due were used, with the relevant parameters summarized in Table 6.1.1. The setup was controlled from a control computer through a LabView program, allowing for the capture of images corresponding to illumination by the individual LEDs of the LED array. Additionally, the setup allows for different acquisition times for BF and DF images in line with a prior implementation by Tian and Waller[38]. For the purposes of this thesis, the LabView program was modified to work with the camera in question.

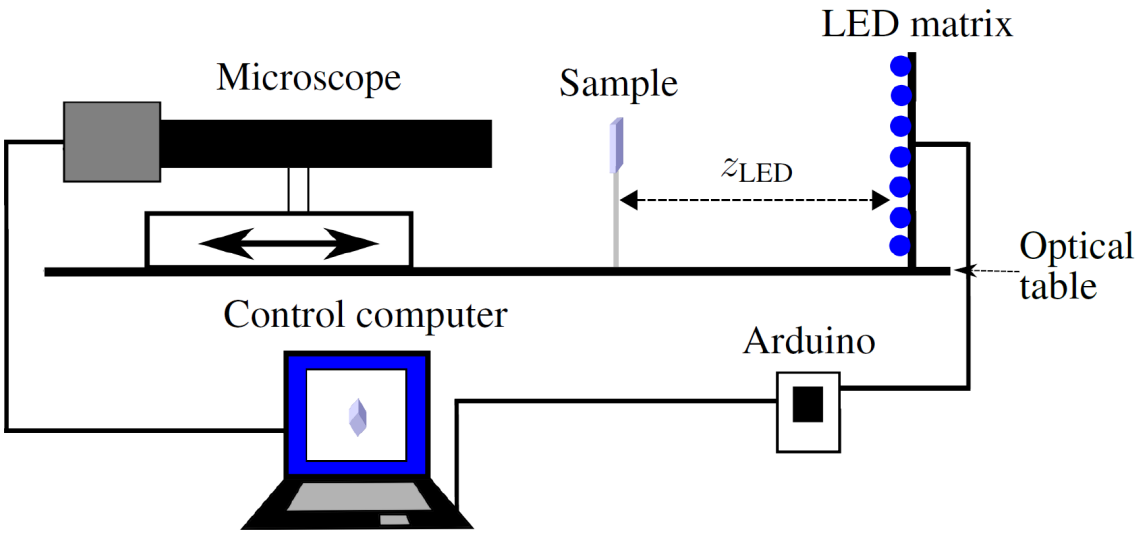

Figure 6.1.1: Illustration of the microscope setup used in this thesis. Taken from [39] with permission.

Table 6.1.1: Relevant specifications for the camera and LED array.

Parameter	Value
Camera pixel count	2856×2848
Camera pixel size	$2.74\,\mu m$
Camera detector area	$7.825\,mm \times 7.804\,mm$
LED spacing	$6\,mm$
LED wavelength (green)	$520\,nm$

Table 6.1.2: Parameters for the employed microscope objective as given by Edmund Optics[40, 41, 42]. Notably, the focal length given for the infinity corrected objective only pertains to the objective itself, and not the complete lens system including the tube lens.

Lens	Magnification	NA	WD (mm)	DoF (µm)	FL (mm)
Compact 2X	2X	0.06	92	76	60.33
Telecentric 3X	3X	0.09	77	34	58.51
Infinity Corrected 10X	10X	0.28	34	3.50	20

Table 6.1.3: Overview of the maximal detector pixel sizes for the employed microscope objectives, as given by Equation 3.14. Max DPS refers to the maximal detector pixel size, while the DPS ratio column show the ratio as compared to the pixel size of the detector used in this thesis.

Lens	Max DPS (µm)	DPS ratio
Compact 2X	8.67	3.16
Telecentric 3X	8.67	3.16
Infinity Corrected 10x	9.23	3.39

6.1.1 Physical lens systems

Throughout this thesis, four physical lens systems will be considered, including three microscope objectives and a camera objective.

The three microscope objectives which will be considered are a 2X Mitutoyo Compact Objective[40], a 3X Mitutoyo Telecentric Objective[41] and a 10X Mitutoyo Plan Apo Infinity Corrected Long WD Objective[42], which will respectively be referred to as the compact 2X, telecentric 3X and infinity corrected 10X objectives or lenses. For all three objectives, an extension tube of 152.5 mm was used in accordance with the product specifications, while the infinity corrected objective required an additional tube lens of 1X magnification and 200 mm focal length inserted between the extension tube and the objective lens. For this purpose, a MT-4 Accessory Tube Lens was used with an AS diameter of 11.2 mm. To minimize the impact of stray light, the extension tube was modified with a non-reflective inlay. Relevant parameters for the three microscope objectives may be found in Table 6.1.2. Notably, all three microscope objectives are designed for a maximum sensor format of 2/3" corresponding to the size of the camera used in this thesis. Table 6.1.3 provide a comparison between the required pixels sizes for the three objectives and the pixel size of the detector.

The camera objective is a Fujinon HF1618-12M[43] camera objective. The objective has a focal length of 16 mm, is designed to be mounted directly onto the camera with no intermediate extension tube and allows for manual adjustment of the working distance and AS size. The working distance may be adjusted between 100 mm and infinity while the AS size may be adjusted between an F-number $f_L/2R$ of 1.8 to 22. Notably, the manual adjustment results in a large amount of uncertainty in terms of the necessary model parameters, being the magnification, the numerical aperture NA and the effective object to AS distance z_q.

6.1.2 Sapphire window

For parts of this thesis, the microscope was used with a sapphire window inserted between the object and lens orthogonal to the optical axis. The sapphire window[44] has a diameter of 25.4 mm, a thickness of 5 mm and a refractive index of 1.77. Additionally, the window has an anti-reflective coating to minimize surface reflections.

6.1.3 Manual alignment and focusing

This section will cover the manual procedures used to align and focus the microscope before imaging.

The alignment procedure aimed to align the optical axis of the system to be orthogonal to the detector, lens, sample, and LED array while simultaneously placing the central LED of the LED array along said optical axis and keeping the sample in focus across the entire field of view. Since the alignment of the lens and detector was ensured through the use of an extension tube, the degrees of freedom that needed to be aligned were the placement of the sample and LED array relative to the optical axis formed by the detector and lens. To this extent, careful positioning of the sample and LED array was used to achieve a rough alignment, while fine-tuning was performed using the translation stages attached to the detector and lens, in the absence of a sample. To align the position of the central LED with the optical axis, four LEDs which individually yielded images containing the BF edge and with symmetrical offsets from the central LED were lit simultaneously. Using the fact that the obtained image should be symmetrical around the center of the FoV, the detector and lens were translated orthogonally to the optical axis using the manual translation stages until symmetry was obtained. Additionally, to verify that there was no substantial tilt of the elements with respect to the optical axis, it was observed that the illumination remained symmetrical when the detector and lens were translated along the optical axis. An illustration of the desired illumination symmetry is given in Figure 6.1.2.

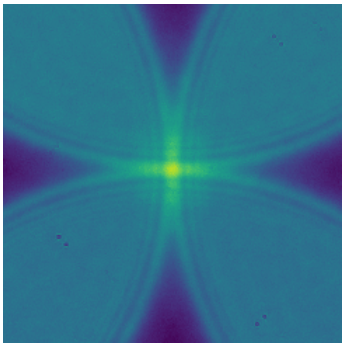

Figure 6.1.2: Illustration of symmetrical illumination for the aligned microscope. The image is taken with the compact 2X lens, under illumination by four symmetrically offset LEDs. The microscope is focused on the plane 200 mm in front of the LED array. A high level of symmetry may be observed, which would have been broken if the microscope had been translated orthogonally to the optical axis.

The focusing procedure consisted of visual inspection, aiming to optimize the sharpness of edges in the sample. Between inspections, the detector and lens were translated in steps of 1 µm to 10 µm dependent on the lens in question along the optical axis using the motorized translation stage.

6.2 Experimental samples

The two samples which were used are a 2"×2" positive USAF 1951 high-resolution target and a Fixed Frequency Grid distortion target as supplied by Edmund Optics[45, 46]. Both targets consist of chromium metal deposited on 1.5 mm thick float glass, resulting in opaque regions where the chromium is present and transparent regions elsewhere.

The USAF 1951 resolution target is illustrated in Figure 6.2.1a, and consists of vertical and horizontal line patterns of decreasing separation distances. The line patterns are denoted by a group number and an element number, with the separation distance being given as

$$2^{\left(Group\#+\frac{Element\#-1}{6}\right)}.$$

In particular, the smallest features of the USAF target used in this project correspond to group 9, element 3, yielding a maximal resolution of 654 lines/mm or 1.55 µm in terms of the separation distance between the centers of the adjacent opaque lines.

The Fixed Frequency Grid is illustrated in Figure 6.2.1b, and consists of circular dots of diameter (65 ± 2) µm forming a square lattice with lattice spacing (125 ± 2) µm. For brevity, this sample will be referred to as the dot array.

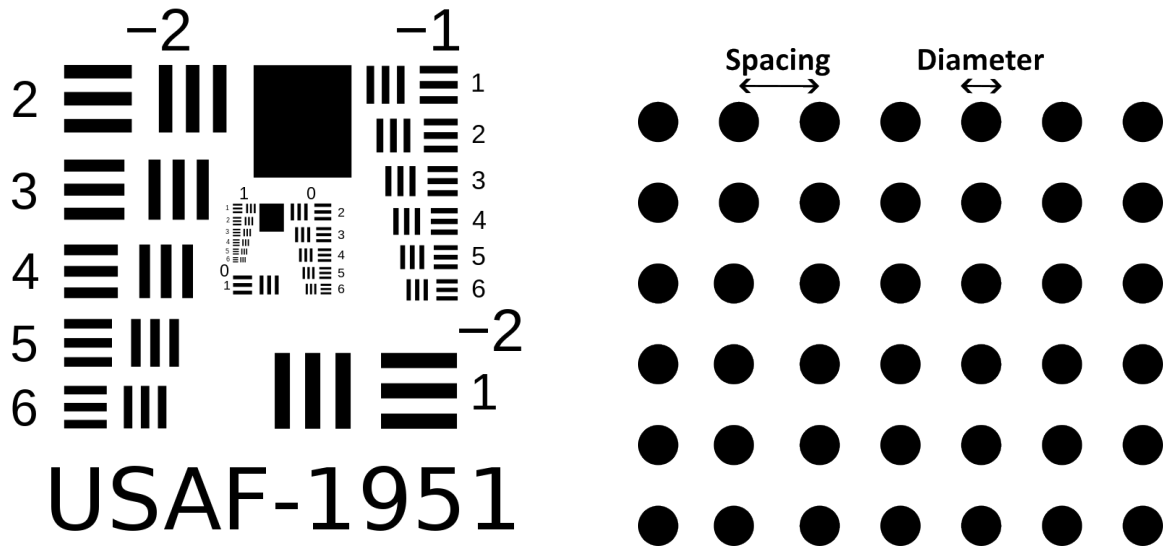

(a) USAF 1951 **(b)** Fixed Frequency Grid

Figure 6.2.1: Illustrations of the two samples that are used in this project. As compared to the illustration, the real USAF 1951 target contains a greater number of groups of decreasing size located at the center, while the real Fixed Frequency Grid contains a total of 200×200 dots. The USAF 1951 illustration is created by Itzhak Baum[47] and licensed under CC BY-SA 3.0.

6.3 Computational implementations

All computational implementations in this project were done in the Python Programming Language[48]. When not otherwise stated, the mathematical implementations make use of the libraries NumPy[49], SciPy[50] and Numba[51]. A GitHub repository containing the code developed for this thesis is available through the link in Appendix A.

6.3.1 Fourier Ptychography pipeline

A major part of this thesis, and the preceding project[7], has been the implementation of a FP processing pipeline. In addition to the FP recovery algorithm, this includes implementations dealing with the Zernike polynomials, data preprocessing and noise reduction.

6.3.1.1 Recovery algorithm

The implementation of the FP recovery algorithm is in line with the theory covered in chapter 3 as applied to the generalized imaging system described in chapter 2. This implies the use of the second order step covered section 3.5 modified with an adaptive step size as covered in subsection 3.8.1, and that the implementation accounts for the quadratic phase at the object plane as covered in section 3.3. In terms of the LED positions and the object spectrum shift, the values are calculated based on respectively the rigid body model described in section 3.7 and the frequency shift found as part of this thesis in subsection 2.3.2. Further, the generalized pupil function is initialized from the pupil function, with the added option of providing a prior estimate for the pupil phase. Finally, the object is initialized based on the lowest frequency shift image, while the LED images are used to update the object spectrum in order of ascending frequency shifts, as illustrated in Figure 6.3.1.

6.3.1.2 Zernike polynomials

The implementation of the Zernike polynomials used in this project is illustrated in Figure 6.3.2 and follows the Noll indexation scheme as described in subsection 4.1.3. Notably, the implementation is applied directly to the pupil phase $kW(x, y)$ as defined in Equation 2.11, while any potential phase wrapping is handled using the phase unwrapping function provided by scikit-image[52].

6.3.1.3 Data preprocessing and noise reduction measures

To decrease the impact of noise, three preprocessing measures are included in the implementation. The first measure is the ability to have different acquisition times for the BF and DF images. While this is initially implemented in the data acquisition software, it is necessary to compensate for this difference during preprocessing. To this extent, the image intensity values are divided by their respective, relative acquisition times. Secondly, pixel binning is implemented by combining groups of k $\times$ k adjacent pixels into larger pixels, with the values of the combined pixels determined by the means of the original pixel groups. The value of k is limited by the pixel size of the combined pixels, which must be lower than the maximal pixel size allowed by the Nyquist sampling theorem, as given by Equation 3.14. The third and final measure is a background noise reduction scheme[21, 30] based on the calculation and subtraction of an individual noise threshold from each image. As implemented, two regions of the FoV are selected, from which a noise threshold is calculated as the mean intensity across the two regions and subtracted from the corresponding image. To account for BF and mixed BF-DF images, an upper threshold is set such that if a noise threshold is found to be larger than the upper threshold, it is replaced by the noise threshold value found for a neighboring image. Finally, any negative values after the subtraction of the noise threshold are set to zero.

An additional noise reduction measure is implemented as a modification of the recovery algorithm to account for any inconsistency between the theoretical model and the captured intensity images at the BF edge. To limit the impact of any such inconsistency, a masking scheme inspired by the sparsely sampled FP algorithm by Dong et al.[31] is implemented. Based on the description of the BF-edge as found in section 5.1, a mask M_i is found for each captured intensity image as the pixels where the corresponding off-axis frequency shift as given by Equation 2.65 lies within 0.85 to 1.15 times the cutoff frequency. Within the recovery algorithm, this mask is applied when updating the amplitude of the simulated complex field at the detector during step 2c of the FP algorithm as described in section 3.1, and when calculating the normalized real space error. In both these cases, the amplitude of the captured intensity images $\sqrt{I_i^c}$ are replaced with

$$\sqrt{I_i^c} \rightarrow \sqrt{I_i^c}(1 - M_i) + |U_D|M_i \,, \tag{6.1}$$

meaning that only the unmasked pixels are updated while the masked pixels retain the amplitude of the calculated wavefield U_D. Empirically, it appears that the masking yields better results if it is not applied from the first iteration, allowing the algorithm to first converge towards the unmasked intensity. As such, the masking is enabled from the 10th iteration. Since any inconsistency near the BF edge may yield a substantial contribution to the normalized real space error, the application of the adaptive step size is similarly delayed to avoid a decrease in the step size due to error fluctuations during the initial iterations.

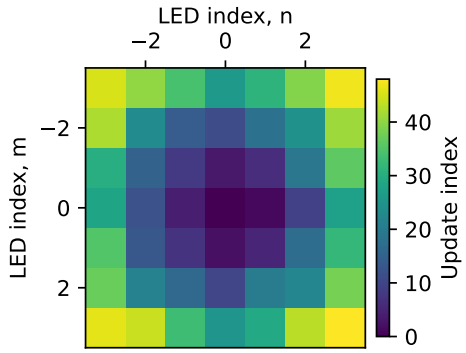

Figure 6.3.1: Illustration of the update order. The LED images are ordered by increasing values of the calculated frequency shift, yielding a radially increasing pattern. The LED indices (n, m) follow the definition given in section 3.7 with $(0, 0)$ corresponding to the central LED. For an off-center patch, the LED with the lowest frequency shift is not necessarily the central LED at $(0, 0)$, meaning that the entire pattern would be shifted.

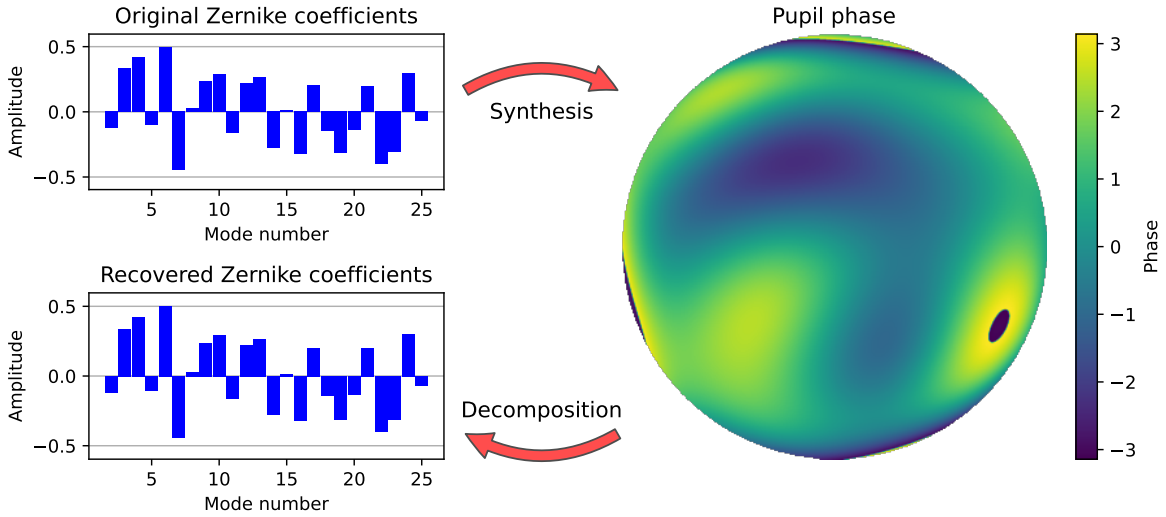

Figure 6.3.2: Example illustrating the synthesis and decomposition of a pupil function using Zernike polynomials. The pupil phase is synthesized from the original Zernike coefficients, chosen as random numbers of a sufficient magnitude to introduce phase wrapping. As can be seen from the recovered Zernike coefficients, the implementation is able to precisely recover the original Zernike coefficients. Notably, the coefficient of the first mode is only recovered down to a factor of 2π and is not included as it corresponds to a constant phase term which may be ignored for the purposes of this project. While the chosen Zernike coefficients in this example are large so as to induce phase wrapping, a similar accuracy is obtained for lower coefficient values as well. The fact that only the 25 first modes are considered in this example is an arbitrary choice, rather than a limitation of the implementation. For a practical use case, the number of included modes should be considered more carefully during decomposition, for instance by considering the degree to which the standard deviation of the aberration function is accounted for by the included modes in line with Equation C.6.

6.3.2 Calibration procedure

This section will consider the computational implementation of the NBFL calibration procedure proposed in chapter 5. This consists of two main parts, being the implementation of the edge point localization scheme through application of the Otsu and Canny algorithms, and the subsequent estimation of the parameters Δx, Δy, θ, z_0, NA and z_q based on non-linear optimization and linear regression.

When implementing the procedure for locating points at the BF edge, several practical decisions were made. Starting with the two algorithms, the implementations provided by the scikit-image python package[52] were used. Empirically, it was found that applying the Otsu threshold to the image intensities raised to some system dependent power between $0.5 - 2$ was necessary to yield a binarization of the images in line with the desired result. Similarly, the Canny algorithm as implemented by scikit-image applies a Gaussian filter as part of the algorithm, whose standard deviation may be set manually. If the default value of one pixel was used, a number of less pronounced edges elsewhere in the image were additionally found. Comparatively, setting a larger value for the standard deviation made it possible to only locate points at the desired edge. Since the Canny algorithm was observed to yield varying results near the image boundary, any points within a distance to the image boundary corresponding to the aforementioned standard deviation were additionally discarded. Furthermore, for the purposes of computational efficiency, the data was downsampled twice; initially through binning of the raw images and by downsampling the final array of located edge points. To some degree, this downsampling may be expected to impact the precision of the algorithm, though any such impact appeared to be minor if the downsampling was not too aggressive. Finally, one should note that these empiric parameters depend on each other and upon the setup in question, implying that slight modifications may be necessary if the procedure is to be applied to a new setup or lens.

For all the lenses, the standard deviation used in the Canny algorithm was set to 10 pixels and the final edges were downsampled by a factor 10. For the three microscope objectives, the pixels were binned by a factor of 4 and the Otsu threshold was found based on the squared intensity of the raw images. For the Fujinon objective, no binning was performed while the Otsu threshold was applied to the amplitude of the raw images. Additionally, the FoV was limited to the central 1400×1400 pixels for the Fujinon objective.

The parameter estimation procedure was implemented twice, corresponding to the applications covered in section 5.4. For respectively the non-linear optimization and linear regression steps, SciPy's *minimize* and *linregress* were applied.

CHAPTER 7

EXPERIMENTAL PROCEDURE

In this chapter, the experiments conducted as a part of this thesis will be described. For all the experiments, the imaging was performed using the microscope setup described in section 6.1 with the LED array placed at varying distances from the sample. Between imaging operations, the lens systems and the samples were interchanged, as specified for the individual experiments below. Before any imaging operation was performed, the setup was manually aligned and focused as described in subsection 6.1.3 and suitable exposure times were selected so that no pixels in any of the captured images reached saturation.

7.1 Calibration and lens modelling

The first experiment aimed to verify the effectiveness of the proposed NBFL calibration procedure, as applied to calibrate the NA and z_q for the compact 2X lens. For each of five separate placements of the LED array, FP datasets with no sample placed in the object plane were captured at 26 increments of 2 mm. Applying the calibration algorithm to each individual dataset with the parameters Δx, Δy, θ, NAz_0 and z_0/z_q, and utilizing linear regression in accordance with Equation 5.6, allowed five estimates for the numerical aperture and z_q to be obtained while additionally yielding the optimal values of Δx, Δy and θ for each individual dataset. No realignment was performed after movement of the LED array, though the holes of the optical table upon which the microscope was placed served as rough guides. Starting at approximately 85 mm and with approximately 25 mm between the placements of the LED array, the effective range of LED distances ranged between 85 mm to 235 mm.

The above steps were repeated once for the telecentric 3X and infinity corrected 10X lenses, with initial placements of the LED array at respectively 185 mm and 40 mm. Additionally, datasets of the BF region were captured for all three lenses with the LED array placed at 100 mm.

To verify whether use of the calibrated values yield any substantive improvement for the purposes of FP recovery, two FP datasets were captured with the USAF resolution target in the object plane using the compact 2X lens. For the two datasets, the smallest features of the USAF target were placed at the center and near the corner of the FoV. Additionally, corresponding calibration datasets with no sample were obtained, to which the NBFL algorithm was applied for calibration of z_0, Δx, Δy and θ. For comparison, recovery was performed with and without the calibrated LED array placement, and with the calibrated and uncalibrated values of the numerical aperture and z_q. The uncalibrated value of z_q was obtained by modelling the system as a single-lens system with the AS at the lens according to subsection 2.2.5.

7.2 Fujinon camera objective

The second experiment aimed to investigate whether FP would be possible with the Fujinon camera objective. For this investigation, the working distance and F-number of the camera objective were both minimized. In addition to uncertainty regarding the NA and z_q, the magnification of the objective was unknown and had to be determined. To this extent, an image of the dot array sample was captured under coherent illumination, from which the magnification was estimated by comparison between the periodicity of the image in pixels and the known periodicity of the sample in terms of physical distance. Further, for application of the NBFL procedure, FP datasets were captured at 26 increments of 2 mm with no sample placed in the object plane and with the LED array placed approximately 320 mm from the object plane of the initial

dataset. To investigate the impact of tuning the F-number of the lens, images were obtained under illumination by a single LED at F-number values of 1.8, 4, 8 and 16.

7.3 Imaging through a glass window

The third experiment aimed to investigate the impact of imaging through a sapphire window, viewed in light of the theoretical coverage in section 4.3.

As an initial investigation, images were captured with the USAF sample in the object plane for all three microscope objectives. For each objective, the captured images corresponded to the best obtainable focus without the sapphire window inserted into the beam path and the best obtainable focus after insertion of the window. Additionally, the necessary translation of the microscope along the optical axis for the refocusing procedure was noted.

Further, FP datasets of the USAF sample were obtained with $z_0 \simeq 200\,\text{mm}$ for each of the three objectives at focus with and without the sapphire window inserted into the beam path, along with corresponding calibration datasets. After calibration with the NBFL algorithm to determine z_0, Δx, Δy and θ, recovery was performed for each dataset to allow for comparison of the recovered values for the intensity, phase and pupil function.

7.4 Number of LEDs used

For all recovered datasets, 120 LEDs were used, corresponding to a circle 13 LEDs in diameter. For the NBFL procedure, the LEDs corresponding to the smallest possible squares containing all BF and partial BF images were considered.

CHAPTER 8

R&D - CALIBRATION PROCEDURE

In this chapter, the results from the experiments related to calibration and lens modelling will be displayed and discussed. This includes the results from the application of NBFL, in section 8.1, and the recovery of a central and off-center patch, with and without the calibrated parameters, in section 8.2.

8.1 Application of the calibration procedure

The experimental results from application of the NBFL calibration procedure to the compact 2X lens are shown in Figure 8.1.1, with the calibrated values of NA and z_q for each of the five datasets reported in Table 8.1.1. Only the data points where the final value of the cost function are below a set limit as shown in Figure 8.1.2 are included in the analysis.

Based on the values reported in Table 8.1.1 and the visual confirmation provided by Figure 8.1.1, one may observe that the behavior of the BF region appears consistent across the entire span of probed LED distances from 85 mm to 235 mm. From the linear regression results, the calibrated values for NA and z_q are found as $NA = 0.060$ and $z_q = (107 \pm 1)\,\text{mm}$. The values for the initial LED distances for each dataset, as found from the intercepts obtained during linear regression, are similarly consistent within 1 mm to 2 mm within each dataset, and vary between datasets in line with the LED array being moved 25 mm farther away from the object for each dataset. Notably, the calibrated value for NA corresponds precisely to the value provided by the supplier, while the expected value of z_q from modelling the objective as a thin lens would be $z_q = z_1 = 90.5\,\text{mm}$ from application of Equation 2.27a.

Figure 8.1.4 illustrates the effectiveness of the calibration procedure, showing the BF

region as well as the expected BF edge corresponding to the calibrated and thin lens values for z_q. From the figure, one may observe that the calibrated value yields a substantially better prediction of the BF edge. However, as shown in greater detail in Figure 8.1.3, one may note the presence of a region just outside the BF edge with a slightly increased illumination intensity and the presence of ripples related to the coherent nature of the system[8, p.219-220]. Considering these two features as potential sources of noise, the selected region to which the masking scheme described in subsubsection 6.3.1.3 is applied may be justified.

The obtained values for Δx, Δy and the rotation of the LED array are similarly consistent within each dataset and between datasets. For the rotation and Δy, the LED distance dependency may be observed to be near constant, with the observable shift in the average Δy between datasets being easily explained by the manual repositioning of the LED array between datasets. Further, a potential explanation for the linear dependency of Δx on the LED distance may be that the LED array is placed at a slight angle as compared to the optical axis defined by the lens and detector. As the LED distance increases by movement of the lens and detector using the motorized stage, the intercept between the optical axis and the LED array would be translated in space. While the LED array is technically stationary, this translation as observed by the detector and lens would be indiscernible from a translation of the LED array as described by Δx. Following this line of reasoning, the calibration procedure may be employed to indirectly measure the presence of a tilt along the two rotational degrees of freedom not included in the rigid body model for the LED positions considered throughout this work, as initially presented in section 3.7.

Alternatively, the rigid body model could be expanded to include the two additional rotational degrees of freedom. To achieve this, the LED positions in Equation 3.11 would instead have to be expressed as

$$\begin{bmatrix} x_i \\ y_i \\ z_i \end{bmatrix} = \mathcal{R}(\alpha, \beta, \gamma) \begin{bmatrix} nd \\ md \\ 0 \end{bmatrix} + \begin{bmatrix} \Delta x \\ \Delta y \\ z_0 \end{bmatrix} \tag{8.1}$$

with $\mathcal{R}(\alpha, \beta, \gamma)$ being a 3D rotation matrix with corresponding rotation angles α, β and γ and z_i being the distance from the object plane to the i-th LED along the optical axis. As compared to Equation 3.11 and assuming small angles, the main difference would be that each LED would have a separate distance z_i from the object plane along the optical axis, while there would be little change in the values along x and y. For the purposes of the BF region, the major consequence would be that the radius of the BF circle would differ between LEDs. These additional rotational degrees of freedom have not been included in the work conducted throughout this thesis for two main reasons. Firstly, differing values of z_i between LEDs are not accounted for by the imaging model considered in this work nor in the reintroduction of the quadratic phase for the purposes of FP as considered in section 3.3. Secondly, it would no longer be possible to combine the parameters $(z_0, z_q, NA) \rightarrow (NAz_0, z_0/z_q)$ on which the calibration of NA and z_q is based.

Table 8.1.1: Table displaying the calibrated values for the numerical aperture NA and the effective object to AS distance z_q for the compact 2X lens. Also displayed are the values z'_{NA} and z'_{z_q} corresponding to the LED distance z_0 at the first step of each dataset.

Dataset No.	NA	z'_{NA}	z_q	z'_{z_q}
1	0.060	87	107	88
2	0.060	112	107	112
3	0.060	137	106	136
4	0.060	162	107	163
5	0.060	187	108	189
Mean	0.060		107	

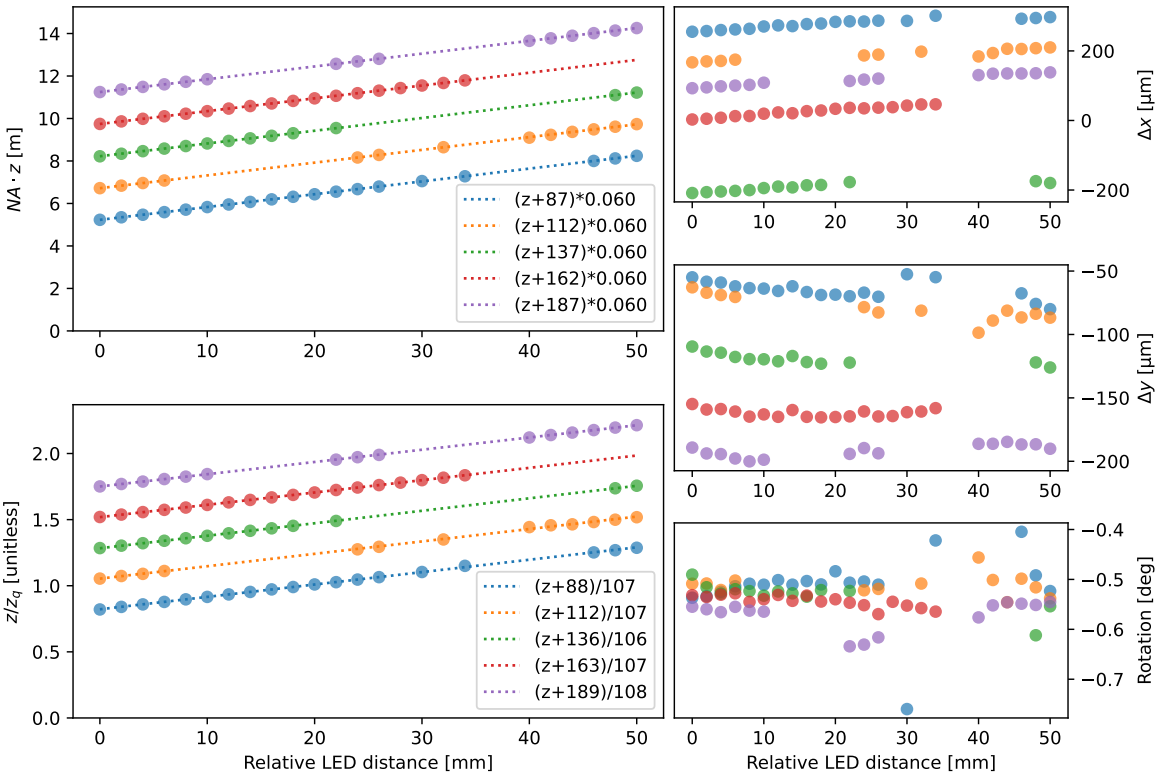

Figure 8.1.1: Calibration results for the compact 2X microscope objective. The expected linear behavior is observed for both $NA \cdot z$ and z/z_q. The found values for Δx, Δy and the rotation may be observed to be internally consistent within each dataset. Notably, the value of Δx display a seemingly linear dependency on the relative LED distance.

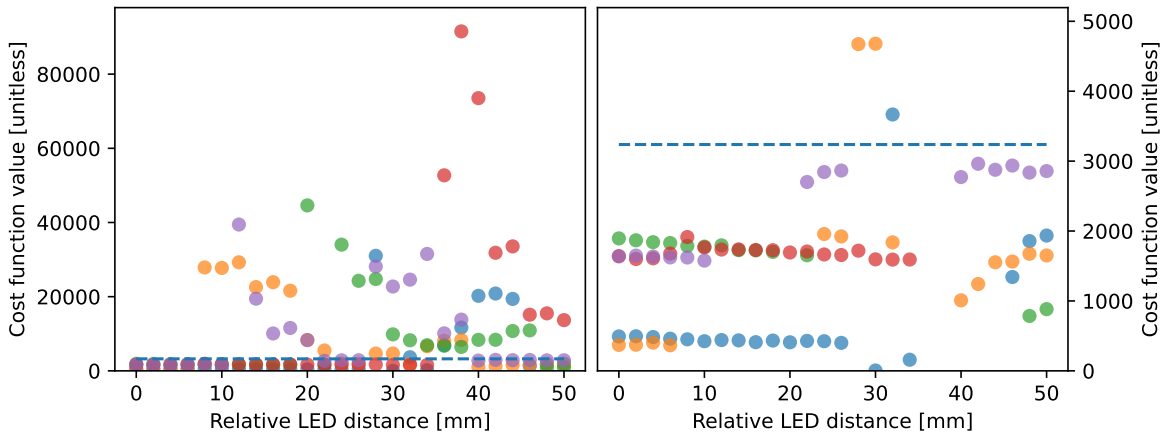

Figure 8.1.2: The cost function values for each of the datasets to which the calibration procedure was applied. All values above a set threshold indicated by the dashed line were excluded from the further analysis. These points correspond to cases where the optimization algorithm has not converged properly. For the included points, the cost function may be observed to differ between the datasets, consistent with the number of images containing a part of the BF edge.

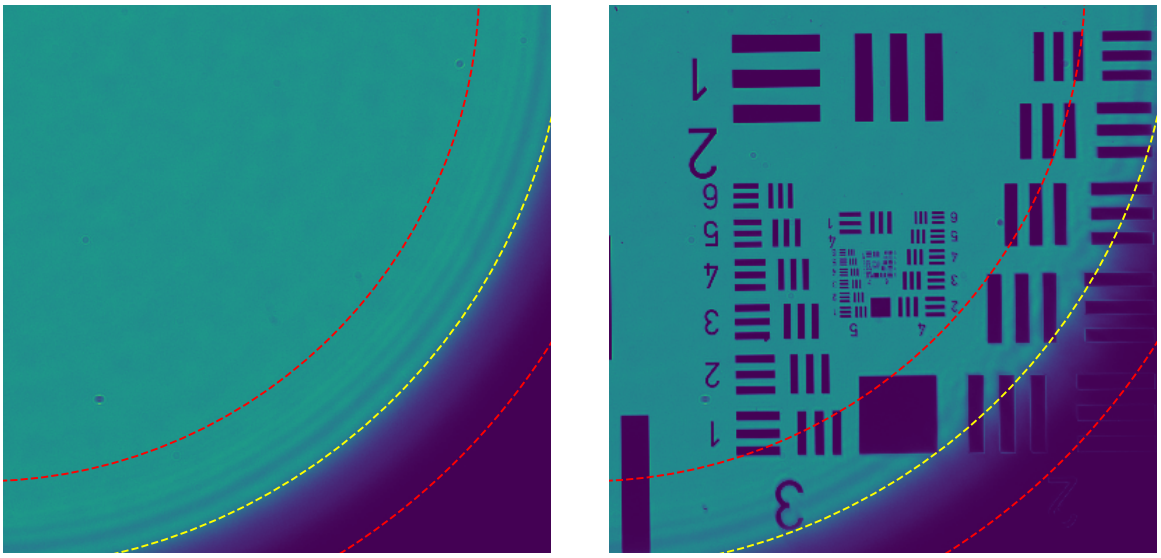

(a) BF only **(b)** USAF target

Figure 8.1.3: BF edge without and with a sample in the object plane. Without, one may observe the presence of ripples just inside the edge and a region of increased illumination intensity just outside the edge. With the USAF sample, the ripples become less well-defined. The yellow line defines the expected location of the BF edge, while the area between the two red lines corresponds to the area ignored during recovery through the masking scheme described in subsubsection 6.3.1.3.

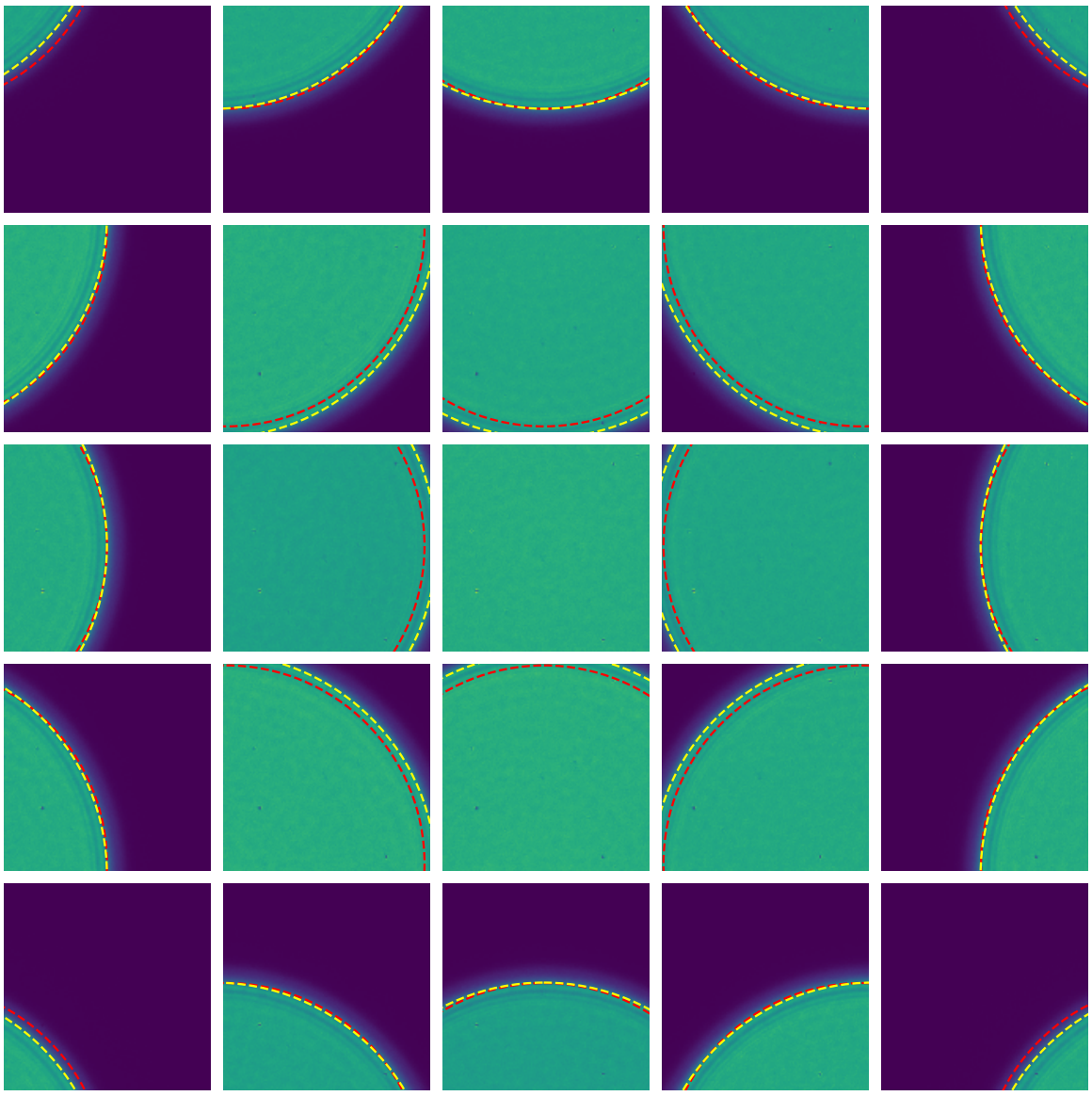

Figure 8.1.4: Images of the BF corresponding to the 5×5 central LEDs as obtained with the compact 2X lens with the LED array 200 mm behind the object. The yellow and red curves correspond to the predicted location of the BF edge based on Equation 5.4 for respectively the calibrated (yellow) and thin lens (red) values of the effective object to AS distance z_q. The calibrated value may be observed to yield an improved fit for half the images, while both values yield similar fits for the remaining images.

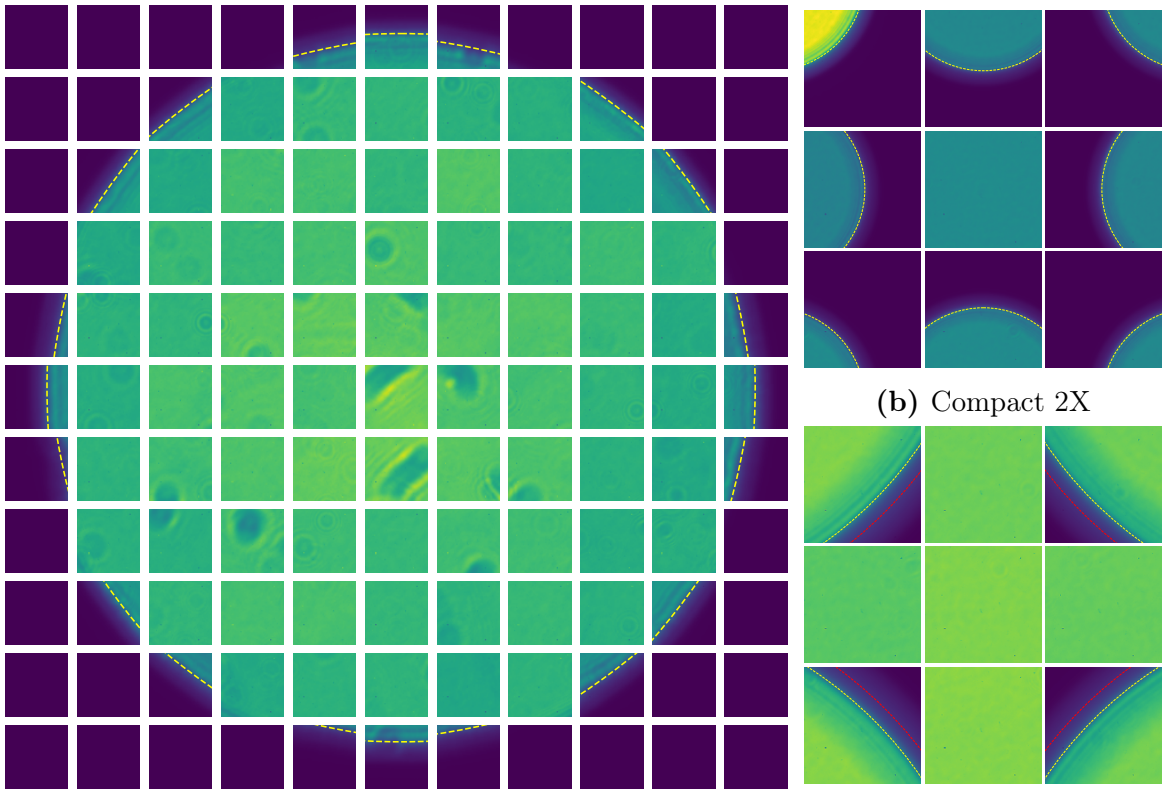

(a) Infinity corrected 10X

(b) Compact 2X

(c) Telecentric 3X

Figure 8.1.5: Images of the BF corresponding for each of the three microscope objectives with the LED array 100 mm behind the object. The yellow curves correspond to the predicted location of the BF edge based on Equation 5.4 for the calibrated values of z_q and NA. For the infinity corrected 10X and telecentric 3X lenses, the calibration was done manually, with the red curves for the telecentric 3X lens corresponding to the unmodified value of NA. Of particular note is the fact that for the infinity corrected 10X lens, the BF in the mixed BF-DF is on the opposite side of the BF edge as compared to the other two lenses. The images additionally demonstrate two challenges encountered when applying the calibration procedure for the three lenses; The first being the occasional appearance of images with significantly increased intensity, as in (b), and the second being related to the differences in how the BF region is affected by changes in the magnification $|K|$, the numerical aperture NA and the effective object to AS distance z_q.

8.1.1 Manual calibration of the telecentric 3X and infinity corrected 10X objectives

Figure 8.1.5 shows the BF region with $z_0 = 100\,\text{mm}$ for each of the three lenses. For the compact 2X lens, the expected BF edge corresponding to the calibrated value of z_q found in section 8.1 is shown. For the telecentric 3X and infinity corrected 10X lenses, the calibration procedure was not applied due to the limitations of the procedure, as will be covered in subsection 8.1.2. Instead, suitable modifications to NA and z_q were

made manually. For the telecentric 3X lens, the BF edge was found to be consistent with $NA = 0.0865$, rather than $NA = 0.09$ as stated by the supplier, retaining $z_q = \infty$ as expected for a telecentric lens. For the infinity corrected 10X lens, fitting the BF edge required a slight modification of the numerical aperture and a major modification of z_q. For the numerical aperture, an optimal value of $NA = 0.2917$ was found, as compared to the supplied value $NA = 0.28$, related by $0.2917 = \tan(\arcsin(0.28))$. This difference may be recognized as a violation of the small angle approximation, which is crucial to the derivations made in this thesis, warranting further investigation in future works. Considering the value of z_q, one may observe that the BF in the mixed BF-DF images for the infinity corrected 10X lens in Figure 8.1.5a is on the opposite side of the edge as compared to the two other lenses. For this to occur within the confines of the derived expression for the BF-edge, Equation 5.3, the requirement is a negative value of $z_0/z_q < -1$. To arrive at the BF-edge in Figure 8.1.5a, the value of z_q was found as $-23\,\text{mm}$. While a negative value of z_q may appear unexpected, it is possible within the scope of the derivations in section 2.2, requiring only that $a_1 > z_1$ for a non-telecentric configuration. Notably, this is an example of an infinity corrected lens which does not exhibit object telecentric behavior. While the assumption of object telecentricity may be valid for some infinity corrected lenses, this result suggests that it is not true in all cases.

8.1.2 Limitations

Considering the application of the calibration procedure, two main limitations will be considered.

Firstly, examination of the detected BF edge points for the discarded values revealed that the edge detection is prone to failure due to LED intensity fluctuations. Either, the intensity fluctuations may alter the threshold found by the Otsu algorithm or yield poor edge detection after application of said threshold for images with intensities far from the mean. The presence of LED intensity fluctuations may be observed in the varying shades of green present in Figure 8.1.4, though the LED intensity fluctuations present in the shown images were not large enough to be detrimental. An especially severe case of LED intensity fluctuation is present in Figure 8.1.5b, where one image has twice the BF intensity as compared to the remainder. Notably, this degree of intensity fluctuation is likely an artifact of some problem specific to the microscope used in this thesis, rather than an expected occurrence.

Secondly, the size of the FoV at the object plane as compared to the size of the BF region appears to be a limiting factor. For a smaller field of view or a comparatively larger BF region, two potentially detrimental effects may be observed, as the number of images containing a part of the BF edge is reduced and the fraction of the BF edge present in the individual images becomes smaller. The first effect is problematic due to the reduction in the unique images based on which the optimal calibration parameters may be found. The second effect may be understood through the relationship between

the curvature, radius, and center of a circle. In particular, as the fraction of the BF edge present in each image becomes smaller, and thus increasingly flat, the optimal radius and center of the circle which best fits the BF edge becomes less easily defined in the presence of measurement noise.

Once Δx, Δy and the rotation of the LED array are corrected for, the information based on which z_0/z_q and NAz_0 may be determined is limited by the fourfold rotation and mirror plane symmetry of the system. This greatly limits the effective number of images containing unique information. Considering the 25 images in Figure 8.1.4, where 24 of the images contain part of the BF edge, the symmetry of the system yields a reduction to six unique image types after accounting for fourfold rotation and a further reduction to only five unique image types after mirror plane symmetry. Considering the datasets in Figure 8.1.5, the images taken with the infinity corrected 10X, compact 2X and telecentric 3X lenses, respectively only display three, two and one unique image types. Conclusively, the effective amount of unique images based on which the values of z_0/z_q and NAz_0 may be optimized is low.

With few unique images, the curvature of the BF region becomes increasingly important as a source of information for determining z_0/z_q and NAz_0. Considering Equation 5.4 defining the BF edge, stating that both the centers and shared radius of the circles defining the BF edge for each image are inversely dependent on $(1 + z_0/z_q)$, while the radius are additionally linear with NAz_0. Implicitly, if only a single unique image type is considered, any change in z_q/z_0 may be offset by a change in NAz_0 such that the only observable impact for a small circle segment would be a change in the curvature. Under these conditions, there would be little differentiating the evaluated values of the cost function. This would be the case for the dataset obtained with the telecentric 3X lens in Figure 8.1.5c. With multiple unique images, this issue is avoided, as the value of z_q/z_0 must be the same for all the images. While the change in the radius for different values of z_q/z_0 is the same for all the LEDs, the change in the centers differ. As such, the aforementioned compensation would require different changes in NAz_0 for each unique image, disconnecting the two variables.

Another case where the curvature becomes a limiting factor for the determination of z_q/z_0 may be observed in the 12 images where the calibrated and thin lens values of z_q both yield similar fits to the BF edge in Figure 8.1.4. As shown visually in the figure, the two values of z_q yield nearly identical fits, mainly differentiated through a very slight difference in the curvature of the predicted BF edge. Particularly, the displayed similarity for different values of z_q becomes an issue when the BF edge contains a point close to the center of the FoV. Since the frequency shift at the optical axis is independent of z_q, as seen from Equation 2.57, the state of the center as either part of the BF or DF is independent of z_q. Implicitly, if the center is precisely at the edge of the BF, it is at the edge for all values of z_q. In this state, only the curvature of the edge changes with z_q, an effect which is observed to be minor.

In general, whether the aforementioned limitation is an issue depends on the size of the FoV at the object plane, the values of z_0 under consideration and the lens

in question through the values of z_q, NA, and the magnification. Considering the ratio between the size of the BF region and the FoV at the object plane, it may be found to increase for higher magnification objectives, which tend to also have higher numerical apertures. As given by Equation 5.4c, the radius of the BF region at the object plane is given by $R_{BF} = |NAz_0/(1 + z_0/z_q)|$. Conversely, the FoV at the object plane is inversely proportional to the magnification for a given detector size. For the three microscope objectives considered in this thesis, the numerical apertures increase approximately linearly with the magnification, yielding a ratio R_{BF}/FoV proportional to the magnification squared. Considering the contribution from z_q, it may be seen that the radius of the BF region decreases for larger values of $|1 + z_0/z_q|$.

The differences in the ratio R_{BF}/FoV for the three microscope objectives is observed in Figure 8.1.5. In order of magnification, the three objectives display increasingly larger ratios R_{BF}/FoV, with relative values of $1 : 4 : 14$. For the telecentric 3X and infinity corrected 10X lenses, only small, near straight parts of the BF edge are contained in each of the images to which the calibration procedure is applied, impeding its effectiveness. This ratio may be lowered by decreasing the LED array distance z_0. However, the smaller FoV at larger magnifications then becomes a greater problem as most of the images will be either fully BF or fully DF, with few images containing the edge. Considering the experimental setup used in this thesis, it appears that the above limitations are not substantial enough to hinder application of the calibration procedure to the compact 2X lens, as illustrated by the results presented at the start of this chapter. However, the small FoV as compared to the size of the BF region appears to inhibit the effectiveness of the calibration procedure if applied to the telecentric 3X and infinity corrected 10X lenses. While this will not be considered further, the implication is that a camera with a larger FoV would be required for effective calibration of the telecentric 3X and infinity corrected 10X lenses.

8.2 Recovery with calibrated parameters

To investigate whether the calibration yielded any substantial improvements in recovery quality, recovery was performed using the compact 2X lens with the USAF sample placed at the optical axis and near the corner of the FoV. For both cases, recovery was performed for a region of 512×512 pixels ($701\,\mu m \times 701\,\mu m$) centered at the finest details of the USAF sample, with the center of the corner region being located 2 mm from the center of the FoV. Considering that the calibration procedure may either be applied to calibrate the values of z_q and NA as considered in the previous section or to calibrate the placement of the LED array through Δx, Δy, θ and z_0, each dataset was recovered under four separate conditions. Either with or without calibration of the lens parameters and with or without calibration of the LED array placement. To calibrate the LED array placement, the calibration procedure was applied to calibration datasets where the sample had been removed before image acquisition, yielding the calibrated parameters in Table 8.2.1. While the recovery was performed for a larger region, only the recovered intensity for the $70\,\mu m \times 70\,\mu m$ region corresponding to the smallest details of the USAF sample will be considered further. The recovered intensity images for this region are displayed in Figure 8.2.2 and Figure 8.2.3, for respectively the central and corner placements of the USAF sample.

Figure 8.2.2 shows that the calibration procedure yields minimal improvement in resolution near the optical axis. Considering the calibration of the LED array placement, the results imply that the misalignment was not large enough to be detrimental to recovery. To explain the negligible difference between the calibrated and uncalibrated values of z_q, one must consider the impact of z_q in the imaging model covered in chapter 2. The value of z_q appears in two ways, for calculation of the quadratic phase and in calculating the frequency shift for an off-axis patch. Since the patch in question is located near the optical axis, the change in the frequency shift for off-axis patches is not expected to impact the recovery quality. Considering the quadratic phase, the impact from a slight modification of z_q may be seen to be minor, as shown in Figure 8.2.1. Additionally, the displayed region corresponds to the center of the recovered patch, where the difference in the quadratic phase is at its lowest.

Figure 8.2.3 shows that the calibration procedure yields a marginal improvement far from the optical axis. In particular, the recovery quality is visibly reduced in Figure 8.2.3b, where neither the calibrated value for z_q nor the calibrated LED placement values are used. Neglecting the impact on the quadratic phase, the expected impact of both calibrations are improvements in the calculated frequency shifts. Considering the error in the calculated frequency shift to be cumulative, the reduced recovery quality for the uncalibrated case and the similarities in quality when either or both calibrations are applied would be explained. Based on the results, one may conclude that performing either of the two calibrations individually improves recovery quality. However, the results are inconclusive in terms of illustrating that applying both calibrations simultaneously is beneficial. To properly conclude that the calibrated value of z_q yields an improvement, further experimentation would be required. In particular,

the impact of a difference in z_q would be expected to increase with the distance from the optical axis, though this would require the use of a different camera than the one used in this thesis.

Table 8.2.1: Table displaying the assumed and calibrated values for the LED array placement for the recovery performed with the compact 2X lens.

	z_0 [mm]	Δx [µm]	Δy [µm]	θ [deg]
Assumed	200.0	0	0	0
Calibrated (center)	201.5	-12.4	-12.7	-0.001
Calibrated (corner)	201.9	-27.8	-8.6	-0.008

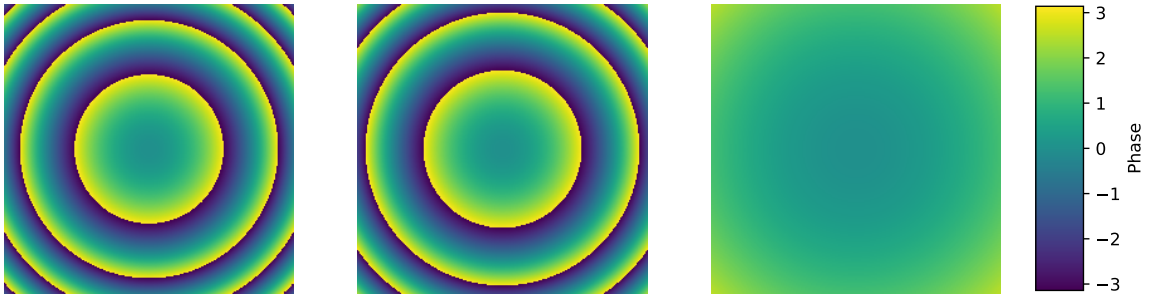

(a) Uncalibrated **(b)** Calibrated **(c)** Difference

Figure 8.2.1: Illustration of the total quadratic phase term, including contributions from spherical illumination and Fresnel propagation, for a patch of 512×512 pixels as imaged by the compact 2X lens with $z_0 = 201.5\,\text{mm}$. (a) and (b) respectively assume the uncalibrated and calibrated values of z_q, while (c) shows the difference between the two cases.

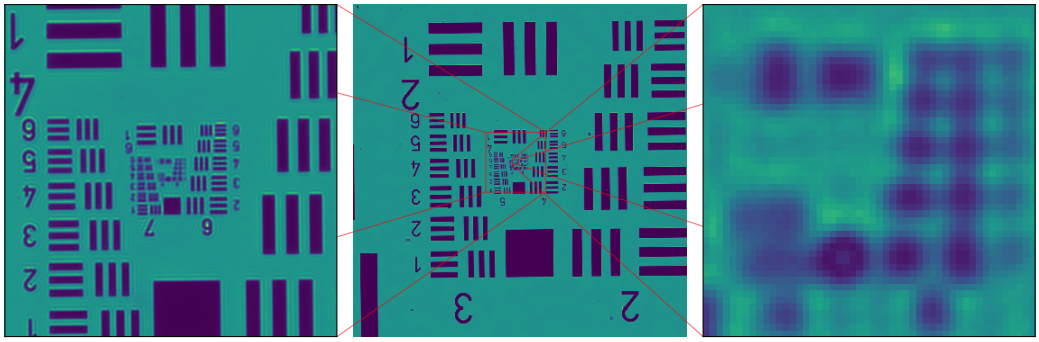

(a) Illustration of recovered and displayed region

(b) Uncalibrated

(c) Calibrated (LED only)

(d) Calibrated (Lens only)

(e) Calibrated (Both)

Figure 8.2.2: Recovered intensity for recovery of a central patch with the calibrated and uncalibrated values of z_q and the LED array placement. The recovery was performed for the larger inset in (a), while (b-e) only show the recovered intensity for the smaller inset. No substantial differences in recovery quality may be observed based on whether the calibrated values are used.

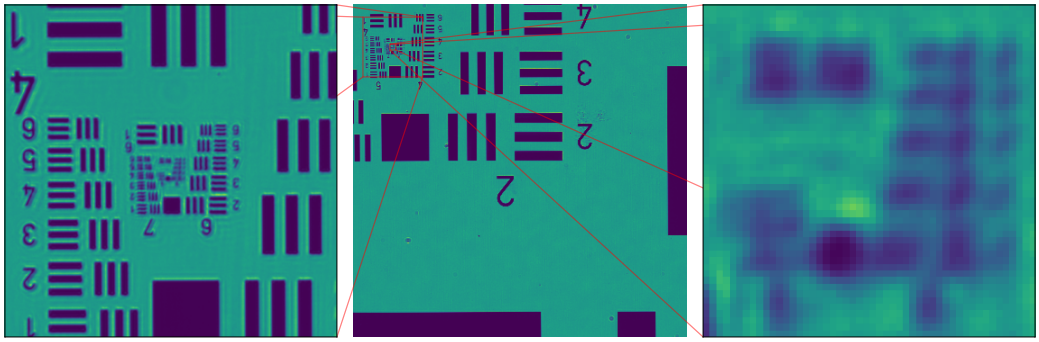

(a) Illustration of recovered and displayed region

(b) Uncalibrated

(c) Calibrated (LED only)

(d) Calibrated (Lens only)

(e) Calibrated (Both)

Figure 8.2.3: Recovered intensity for recovery for an off-axis patch with the calibrated and uncalibrated values of z_q and the LED array placement. The recovery was performed for the larger inset in (a), while (b-e) only show the recovered intensity for the smaller inset. No substantial differences in recovery quality may be observed between (c-e), while (c-e) all show a visible improvement when compared with (b) where neither calibration is applied.

CHAPTER 9

R&D - FUJINON CAMERA OBJECTIVE

In this chapter, the results from the investigation into the Fujinon camera objective will be considered.

9.1 Calibration of the Fujinon camera objective

Based on the image of the dot array sample obtained under incoherent illumination, the magnification was determined to be 0.177X when the adjustable working distance is minimized. As shown in Figure 9.2.1, this value for the magnification is consistent with the known spacing of the dot array sample. Upon increasing the working distance, a decrease in the magnification was observed, increasing the size of the FoV, though this will not be considered further. Leaving the working distance at its minimal value, the NBFL calibration procedure was applied, yielding calibrated values of $NA = 0.044$ and $z_q = 95\,\text{mm}$. These values were obtained with the AS in its most open state, maximizing NA through minimization of the adjustable F-number. Considering Figure 9.2.3, showing the size and shape of the BF region as the F-number is increased, one may note that the BF region initially only covers a small fraction of the FoV and that it becomes smaller and hexagonal as the F-number increases. Considering the BF region as a projection of the AS, the decreasing size is expected since the F-number is inversely proportional to the AS radius and thus inversely proportional to the numerical aperture. Likewise, the hexagonal shape of the BF region implies a hexagonal AS shape, implying that the AS size is controlled through a shutter with six blades. Further, one may note that the artifacts near the BF edge remain equally large regardless of the F-number, covering an increasingly large fraction of the BF region.

9.2 Challenges for the purposes of Fourier Ptychography recovery

For the purposes of FP, the objective poses several challenges. For the maximal value of the numerical aperture, $NA = 0.044$, and a magnification of 0.177X, the maximal detector pixel size according to the sampling requirement given by Equation 3.14 is 1.04 µm, a factor 0.38 as compared to the IDS U3 camera pixel size. Recovery under these conditions is not possible with the FP implementation considered in this thesis, though it may be possible by utilizing the sub-sampled FP scheme proposed by Dong et al.[31]. Alternatively, the simplest solution would be to decrease the numerical aperture by a factor of ~ 3. However, this would be equivalent to a corresponding increase in the F-number, requiring further work accounting for a non-circular pupil shape before FP recovery would be possible. Further, the small size of the BF region may also be problematic, as it is optimal to initialize the recovered object based on a BF image and due to the increasing presence of BF edge artifacts with increasing F-number. Comparatively, the BF region would increase in diameter by a factor $1 + z_0/z_q \sim 4.5$ for a telecentric lens with $z_q = \infty$. Finally, a purely practical challenge is the fact that with increasingly small values of NA, increasingly large values of z_0 are required to retain sufficient overlap in the frequency domain for a given spacing between the LEDs of the LED array.

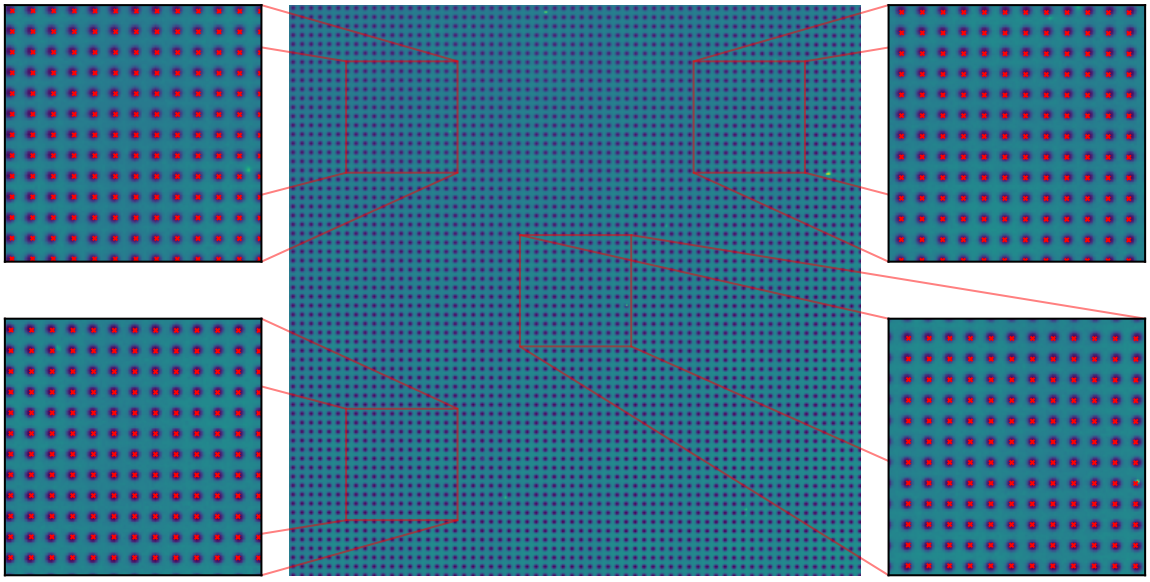

Figure 9.2.1: The magnification of the Fujinon objective is 0.177X for the given working distance. At this magnification, the imaged dot array spacing coincides with the known value (red dots). The image correspond to a 512×512 pixel ($8\,\text{mm} \times 8\,\text{mm}$) patch of the FoV.

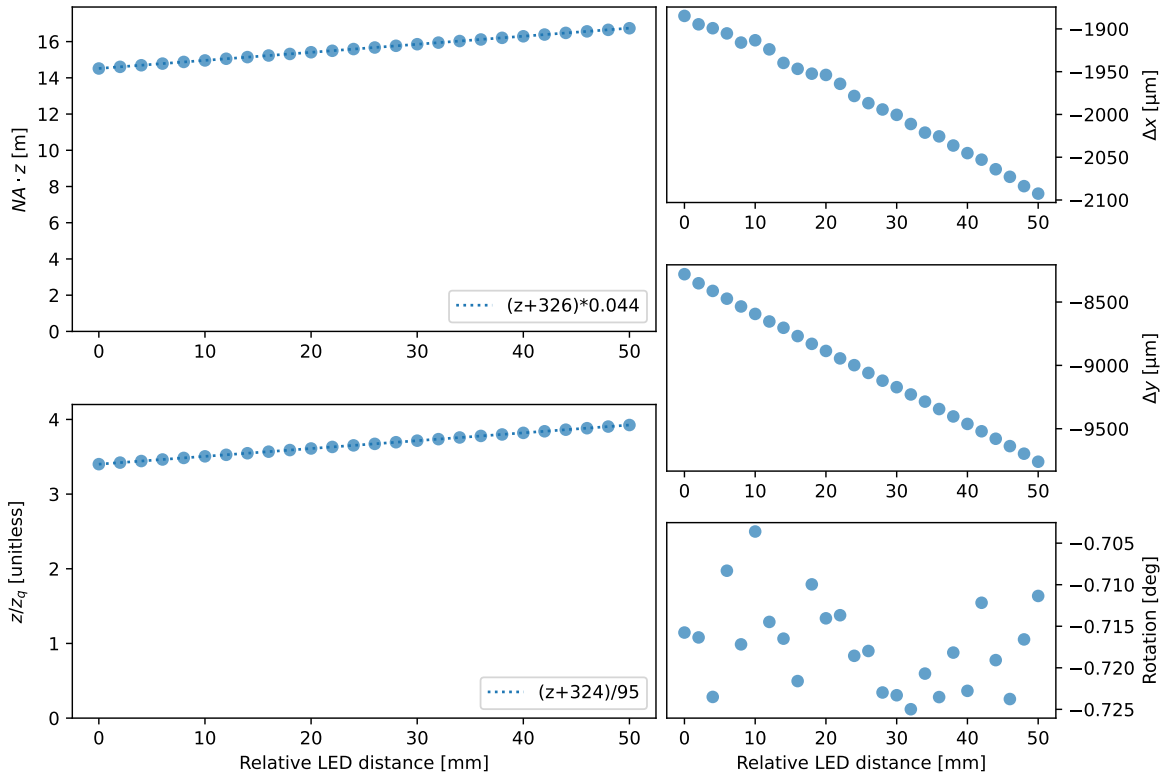

Figure 9.2.2: Calibration result for the Fujinon objective. The expected linear behavior is displayed, yielding $NA = 0.044$ and $z_q = 95\,\text{mm}$.

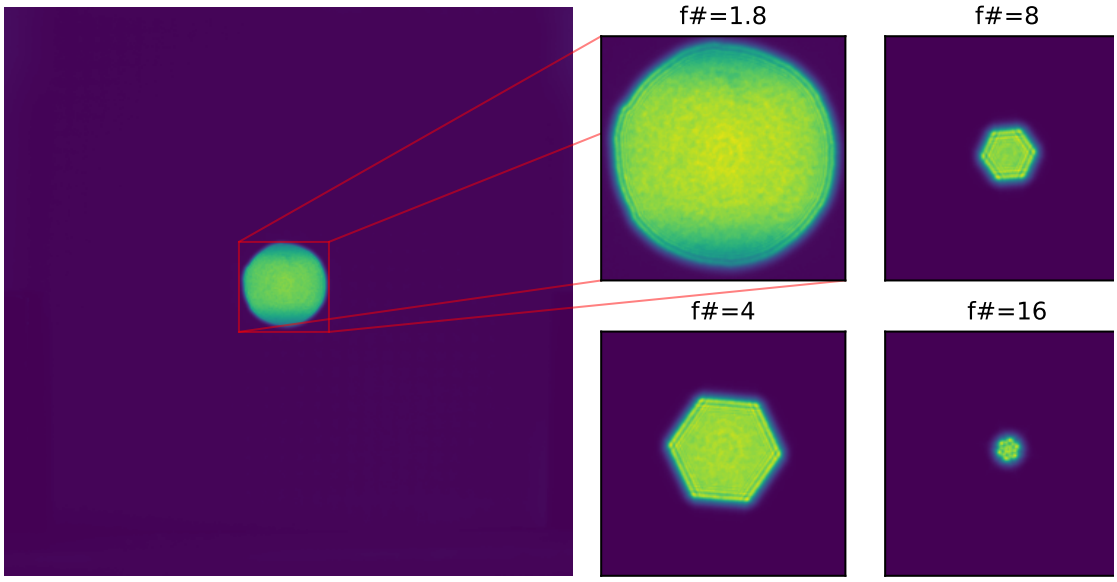

Figure 9.2.3: Image of the BF region when tuning the AS size of the Fujinon objective, under illumination by the central LED. The BF region can be seen to initially only cover a small part of the FoV, and becomes smaller and hexagonal as the F-number is increased.

CHAPTER 10

R&D - IMAGING THROUGH A SAPPHIRE WINDOW

In this chapter, the results from the experiments related to imaging through the sapphire window will be displayed and discussed.

10.1 Impact on low resolution images

Figure 10.2.1 shows the low-resolution intensity images of the USAF sample, for each of the three lenses, before and after inserting of the window between the object and the lens. For the compact 2X and telecentric 3X lenses, inserting the window had minimal impact on the resolution and image quality. For the infinity corrected 10X lens, the window may be observed to cause a significant blurring. For all three lenses, it was necessary to increase the sample to lens distance by 2.15 mm to 2.19 mm after inserting the window, compared to a value of 2.17 mm predicted by Equation 4.9. Additionally, inserting the window yielded small shifts in the FoV, corresponding either to the window being slightly tilted as compared to the optical axis or an unintended movement of the sample upon insertion of the window. While attempts were made at avoiding the latter, the possibility should not be discarded, as the window mount used in the setup was attached to the sample holder.

10.2 Impact on the recovered intensity and phase

Figure 10.2.2 and Figure 10.2.3 respectively show the recovered intensity and phase for each of the three lenses. For the compact 2X and telecentric 3X lenses, inserting the window had minimal impact on recovery quality. For the infinity corrected 10X

lens, recovery without the window yielded substantial higher quality as compared to recovery with the window. In particular, the recovered intensity became blurred after inserting the window, while the phase does not appear to have converged properly.

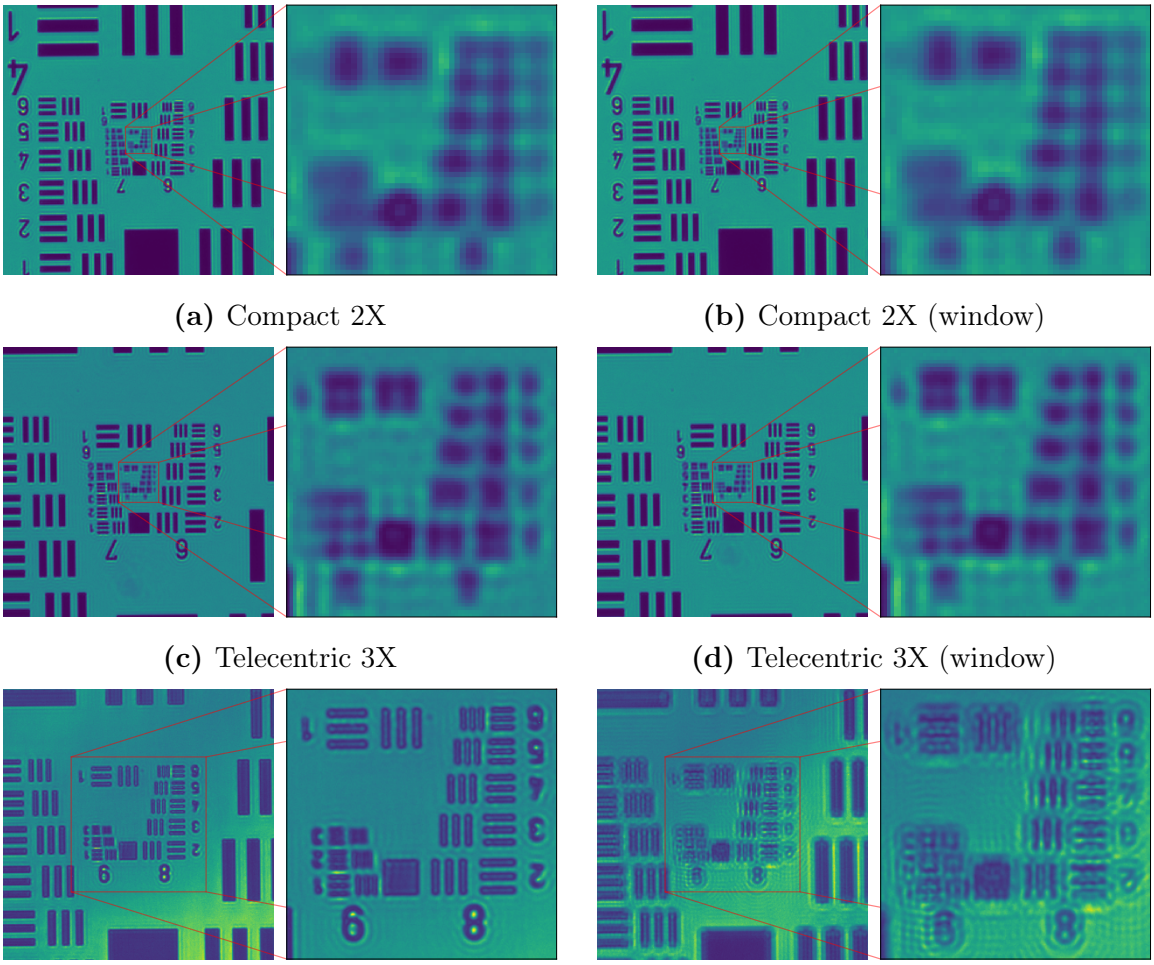

(a) Compact 2X **(b)** Compact 2X (window)

(c) Telecentric 3X **(d)** Telecentric 3X (window)

(e) Infinity corrected 10X **(f)** Infinity corrected 10X (window)

Figure 10.2.1: Low-resolution intensity images of the USAF sample for each of the three lenses, before and after inserting the window between the object and the lens. The images correspond to the 512×512 pixel patches located near the optical axis for which the recovery was performed. The insets display the $70\,\mu m \times 70\,\mu m$ regions containing the smallest features of the USAF sample, which will be considered further. (a-b) and (c-d) show that minimal differences were induced by inserting the window. Comparing (e-f), a significant blur may be observed after inserting the window.

Recovered intensity

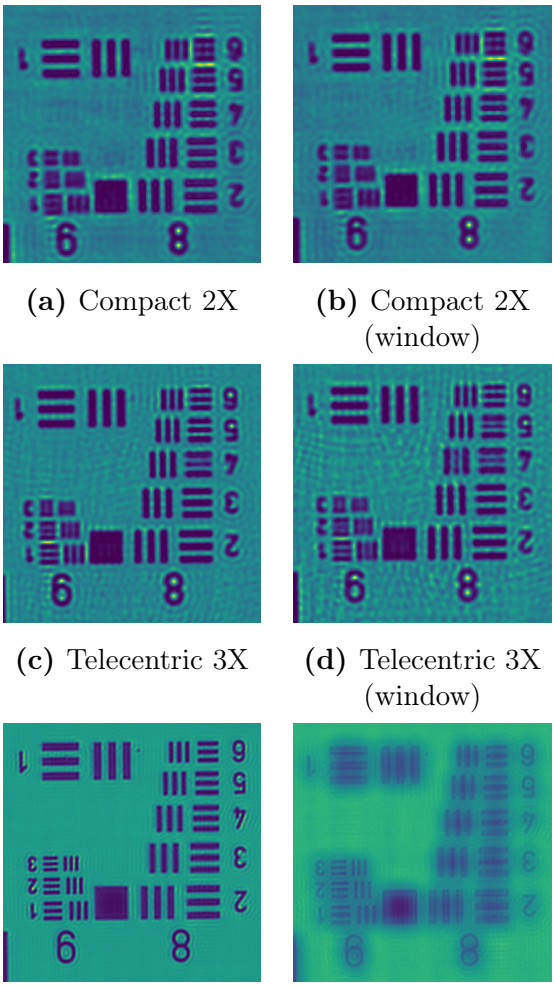

(a) Compact 2X

(b) Compact 2X (window)

(c) Telecentric 3X

(d) Telecentric 3X (window)

(e) Infinity corrected 10X

(f) Infinity corrected 10X (window)

Figure 10.2.2: Recovered intensity for the smallest features of the USAF sample for each of the three lenses under consideration, before and after inserting the window between the sample and lens. The results for the compact 2X lens in (a-b) show no noticeable impact from inserting the window. The results for the telecentric 3X lens in (c-d) show no difference in resolution, though the recovery performed after inserting the window displays a slightly less flat background. The results for the infinity-corrected 10X lens in (e-f) show no reduction in resolution, though the recovery performed after inserting of the window appears to be noticeably affected by the window's presence.

Recovered phase

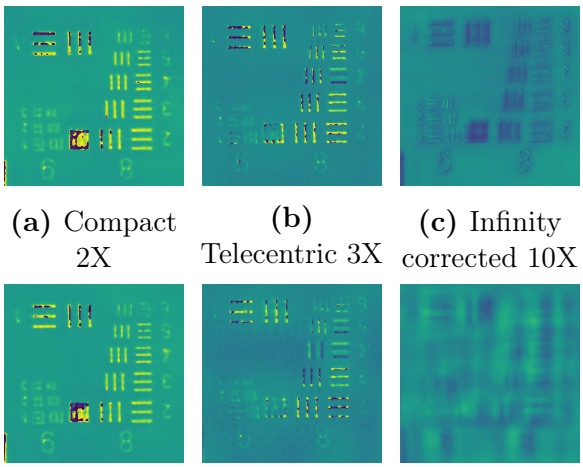

(a) Compact 2X

(b) Telecentric 3X

(c) Infinity corrected 10X

(d) Compact 2X (window)

(e) Telecentric 3X (window)

(f) Infinity corrected 10X (window)

Figure 10.2.3: Recovered phase for the smallest features of the USAF sample for each of the three lenses under consideration, before and after inserting the window between the sample and lens. While the phase is not properly defined for the opaque regions of the sample with minimal transmission, the recovered phase appears well-behaved for (a-e). For (f), the phase does not appear to have converged properly.

10.3 Impact on the recovered pupil

The impact of the window upon the recovered pupil is displayed in Figure 10.3.1. Analysis of the Zernike modes in terms of the equivalent Seidel aberrations is based on table 16 by Niu et al.[36].

For the compact 2X lens, inserting the window yielded minimal change. Considering Figure 10.3.1a, the recovered pupil amplitude and phase show no substantial visual change. Comparing the Zernike coefficients of the recovered phase, all the displayed modes show minimal change, except for mode 4 corresponding to defocus. Otherwise, the main aberrations appear to be contained in modes 7, 8, 11 and 22, corresponding to primary x and y coma and the primary and secondary spherical aberrations. Applying Equation 4.8 the recovered defocus coefficients correspond to respectively 17.5 µm and 10.5 µm defocus without and with the window.

Based on Figure 10.3.1b for the telecentric 3X lens, inserting the window yielded minimal visual change in the recovered amplitude and moderate change in the recovered phase. Comparing the Zernike coefficients of the recovered phase, non-insignificant differences may be observed in modes 4, 7 and 11 corresponding to defocus, primary y coma and primary spherical aberration. Otherwise, the main aberrations appear to be contained in modes 5, 8, and 17, corresponding to 45° primary astigmatism, primary x coma and secondary y coma. From the defocus coefficients, the defocus is found as respectively 0.3 µm and 2.4 µm without and with the window. Interestingly, the Zernike coefficient values imply that a lesser degree of aberrations is present after inserting of the window, particularly noticeable for the two largest modes. This may be interpreted in two ways, either the window is beneficial and counteracts the aberrations inherent in the lens, which would be explained by the aberrations caused by the window having opposite signs compared to the pre-existing aberrations. Alternatively, the presence of the window decreases the convergence properties of the recovery procedure, thus inhibiting the ability of the EPRY algorithm to recover the true value of the pupil phase. This could either be a consequence of an increased level of aberrations, or be caused by the dataset captured after inserting the window being less precisely aligned due to the observed shift of the FoV potentially originating from a slight tilt of the window.

Considering Figure 10.3.1b for the infinity corrected 10X lens, significant differences may be observed in both the recovered amplitude and phase before and after inserting the window. Based on the Zernike coefficients, the most significant aberrations without the window are contained in mode 4, 5, 6, 8, 11, 13 and 22, corresponding to defocus, 45° and 0° primary astigmatism, primary x coma, primary spherical aberration, 45° secondary astigmatism and secondary spherical aberration. Notably, the defocus and 45° primary astigmatism terms are significantly larger than the remaining terms, with the defocus term corresponding to a distance of 1.6 µm. Comparatively, only a defocus of 0.1 µm is corrected for in the recovered pupil after inserting the window, with the largest Zernike coefficients being in mode 8, 11 and 22, corresponding

to primary x coma and the primary and secondary spherical aberrations. For all three modes, the coefficient amplitudes differ significantly compared to before inserting the window. Concerning the recovered pupil amplitudes, they are noticeably different before and after inserting the window. Notably, one may observe that they share similar features as their phase counterparts. While this could be indicative of the true pupil amplitude, one should also consider that it could be a result of poor convergence, seeing that bleeding between the intensity and phase has been commonly observed for the recovered object in the presence of noise, misalignment and poor aberration correction[14, 19, 24, 31, 32].

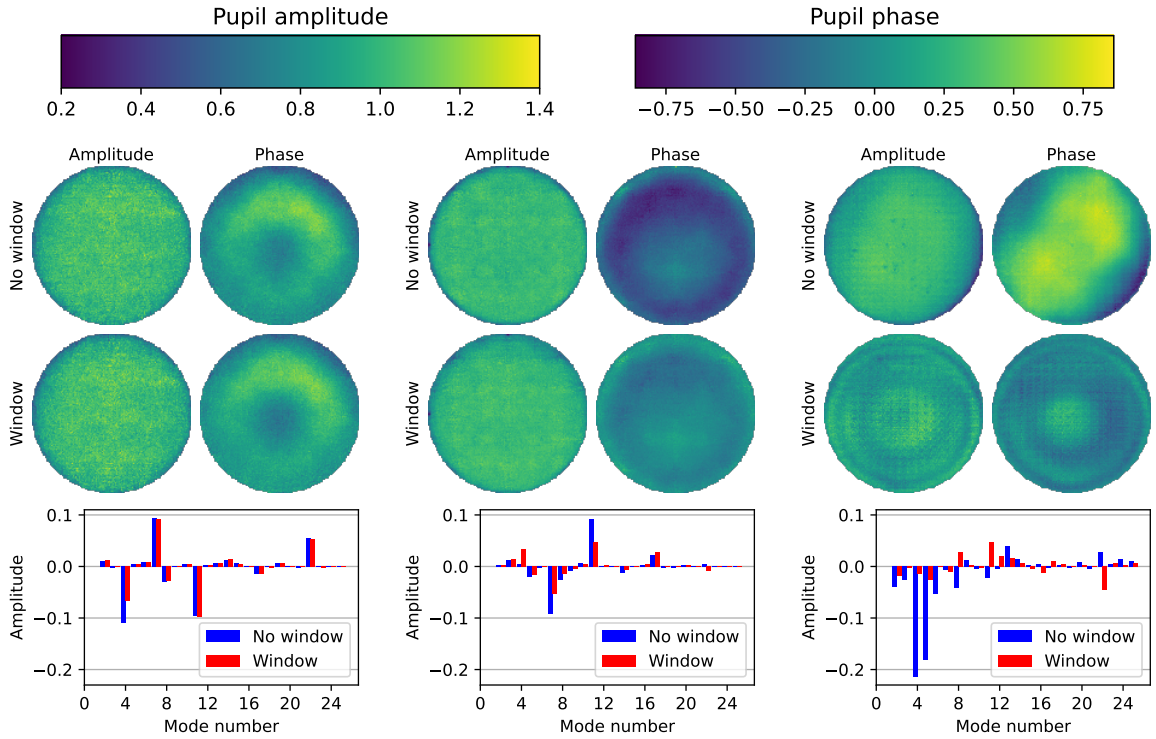

(a) Compact 2X **(b)** Telecentric 3X **(c)** Infinity corrected 10X

Figure 10.3.1: Recovered pupils for each of the three lenses under consideration, before and after inserting the window between the sample and lens. The images show the pupil amplitudes and phases, while the bar plots show the Zernike coefficients corresponding to the 25 first modes as obtained from decomposition of the pupil phase. For the compact 2X lens, the main difference before and after inserting the window is accounted for by the defocus term (mode 4). For the telecentric 3X and infinity corrected 10X lenses, more significant differences are observed. For the telecentric 3X lens, the differences are mainly present within the recovered pupil phase, while the infinity corrected 10X lens displays differences in both the recovered pupil amplitude and phase.

10.4 Implications and basis in aberration theory

The results covered in this chapter imply that FP imaging through the window is unproblematic for the compact 2X and telecentric 3X lenses, while it leads to a significant reduction in quality for the infinity corrected 10X lens. These results may be considered in light of the theoretical model presented in section 4.3. However, before further application of the model, the fact that the model derives the impact of a window on a converging beam of half angle u, as compared to the more complex case of a lens-based imaging system should not be ignored. Rather than a single converging beam, the light scattered by each point of the sample may be considered as spherically diverging waves. Assuming that this is a valid interpretation, one may expect the half angle to be given by the numerical aperture of the lens, $u = NA$. Further, the following discussion will assume that the impact of the window is similar for converging and diverging waves.

First, one may observe that Equation 4.9 accurately predicted the necessary refocusing distance after inserting the window. For all three lenses considered in this work, the defocus was observed to cause the largest immediate decrease in image quality after inserting the window. However, the defocus is easily addressed by a refocusing of the system. Notably, the refocusing distance as given by Equation 4.9 is solely a function of the refractive index and thickness of the window, meaning that it should be the same for all lens systems.

Under the assumption that $u = NA$, the theoretical model predicts a spherical aberration scaling with $Ntu^4 = NtNA^4$ upon insertion of the window. Considering the numerical apertures of the three lenses; 0.06 for the compact 2X lens, 0.09 for the telecentric 3x lens and 0.28 for the infinity corrected 10X lens, the corresponding ratios of NA^4 are $1 : 5 : 474$. Further, the numerical aperture should be reasonably larger than any unintended tilt of the window. Likewise, the same should hold for the angles of the chief rays for all points within the FoV. Thus, only the spherical aberration term should be of any significant magnitude.

Applying Equation 4.13, the expected change in the Zernike coefficients of the primary spherical aberration term (mode 11) may be calculated. For the compact 2X, telecentric 3X and infinity corrected 10X lenses, the eleventh mode is predicted to change by respectively -0.011 and -0.057 and -5.32. For the compact 2X lens, the predicted value is consistent with the minimal change observed for mode 11 in Figure 10.3.1a. Similarly, the predicted value for the telecentric 3X lens may be seen to correspond to the decrease in the eleventh mode in Figure 10.3.1b. Considering the infinity corrected 10X lens, the predicted value is several ten-fold times larger than the coefficients of the other recovered modes, and would correspond to a pupil phase containing several phase wraps. As such, the failure of the recovery algorithm to fully converge is unsurprising. However, if the recovered pupil is indicative of its true value, one should additionally note the observed changes in the secondary spherical aberration (mode 22) and in the recovered pupil amplitude. Neither of these two changes are predicted

by the theoretical model, indicating that they either are consequences of poor convergence or that the theoretical model is insufficient to fully describe the impact of imaging through a window for a high numerical aperture system.

Viable approaches to address the challenges with recovery for the infinity corrected 10X lens may be to either improve the initialization of the pupil or reduce the magnitude of the aberrations caused by imaging through the window. For the former, one should note that the improved initialization would not fully remove the impact of having severely aberrated raw images. In particular, the blurring caused by an increase in aberrations smears out the information contained in the captured images, lowering the signal-to-noise ratio. To reduce the degree of aberration, the principal avenue is to reduce the thickness t, though this is limited by the physical requirements of a given application. Theoretically, one may also aim to reduce the value of N, though this would yield minimal benefit as it lies within 5% of its maximal value for refractive index values between 1.5 to 2.1 and within 10% between 1.4 to 2.4, containing most optical glasses.

Finally, one should note the implications of the obtained results within the broader context of FP. In accordance with the theoretical model, the aberrations caused by imaging through a glass window have been observed to scale with the numerical aperture of the imaging lens. As observed when comparing Figure 10.2.1e and Figure 10.2.1f, direct application of a high numerical aperture objective results in substantial aberrations. However, as illustrated by the minimal changes in recovery quality for the compact 2X and telecentric 3X lenses after inserting the window, this challenge may be overcome through the application of FP. Due to the nature of FP as a synthetic aperture technique, the acquired images inherit the beneficial properties of having a low magnification and low numerical aperture lens. In addition to the normally elevated benefits of having a large FoV and DoF, the results presented in this thesis demonstrate an additional benefit, being the minimization of the aberrations caused by imaging through a window.

CHAPTER 11

CONCLUSIONS

This thesis has considered the modelling, calibration and aberrations of imaging systems for the purposes of Fourier Ptychography (FP). This was done through combined application of theoretical, numerical and experimental methods. The main contributions in this thesis are the derivation of a generalized imaging model based on paraxial optics, the proposal of a system calibration scheme based on the origin of the Bright-Field (BF) region within the derived imaging model and an initial investigation into the detrimental effects of imaging through a window.

In previous works, models describing single-lens systems with the Aperture Stop (AS) at the lens and object-side telecentric systems for which the AS is located in the first lens' back focal plane have been derived. In this work, these models were reviewed and placed in the context of a generalized imaging model, additionally allowing for two-lens imaging systems with arbitrary distances between the AS and the lenses. This yielded an imaging model with a variable quadratic phase at the object plane, which may either be positive, negative or vanish based on the placement of the AS. This quadratic phase was found to be dependent on an effective object to AS distance. Conversely, the distance from the AS to the image-side lens was shown to not influence the intensity imaging process. Based on the effective objective to AS distance, and accounting for spherical LED illumination, a wave optical derivation of the frequency shift for off-center regions was performed. Conclusively, it was shown that imaging systems with varying AS placements requires different treatments for the purposes of FP recovery, with the necessary considerations being summarized.

To calibrate the system parameters of an unknown or misaligned system, a calibration scheme based on the origin of the BF region was proposed. Experimentally, four lens systems were considered, including three microscope objectives and a camera objective. Application of the calibration procedure to calibrate the effective objective to AS distance and the numerical aperture for the four lens systems, was successful for the

2X compact microscope objective and for the camera objective. These results serve to demonstrate the validity of the generalized imaging model. For the calibration of the 3X telecentric and 10X infinity corrected microscope objectives, the increasing ratio between the size of the BF region and the object Field of View (FoV) for higher magnification objectives was found to be a limiting factor. When recovery was performed to illustrate whether the calibrated effective objective to AS distance yielded improved recovery quality for the compact 2X lens, minimal improvement was observed. While the camera objective was found to follow the expected imaging model, the ratio between its numerical aperture and magnification was such that the sampling requirements for FP were broken, hindering its application for FP recovery.

Finally, it was found that inserting a window into the optical path of a microscope yields aberration limited imaging for high numerical aperture objectives, while low numerical aperture objectives are minimally affected. This may be explained from a theoretical perspective by the appearance of aberrations scaling rapidly with the numerical aperture. Importantly, these aberrations may become too large to be corrected for within the recovery algorithm, as exemplified by the poor convergence results for the infinity corrected 10X lens in chapter 10.

11.1 Practical application of modelling results

The derivations made in this work demonstrate that imaging systems will exhibit varying behavior based on the placement of the AS. Within the context of FP, this behavior affects the recovery algorithm through the quadratic phase at the object plane, which in turn influences the frequency shift for off-axis regions. As such, correct calculation of these values requires the AS placement to be determined when dealing with an objective of unknown behavior. In this work, it was demonstrated that the AS placement, as defined through the effective object to AS distance, may be determined based on the edge of the BF region. While this thesis implemented an automated calibration scheme for this purpose, a manual calibration may be more easily implemented in other projects under the condition that the illumination distance is known precisely.

11.2 Lens selection

Concerning lens selection for FP systems, several considerations may be elevated based on the work performed while writing this thesis.

Starting with the AS placement, it may be seen to further affect the image formation through the size and location of the BF region and the telecentricity of the imaging system. These properties are present and should be considered, even if the effective object to AS distance is determined precisely. While the benefits of telecentricity have

not been emphasized in this work, it should still be considered during lens selection. In particular, one may expect that object-side telecentricity would be particularly important when the microscope is required to be used away from the optimal focus, such as for the multislice 3D FP scheme by Tian and Waller[38]. Considering the BF region, one may note that its size is maximized for an object-side telecentric lens. This may be beneficial under the assumption that the BF has a lower degree of noise as compared to the Dark-Field (DF), and if the region near the BF edge which does not adhere to the imaging model is of constant size. For a given illumination distance, one may further observe that it would be possible to construct a lens system such that the quadratic phases from the spherical illumination and the lens system would cancel. Such a configuration would make each captured image either entirely BF or DF, which could be beneficial from a noise perspective. However, this would also remove a major source of information about the system alignment, and would not be advised.

Further, one should consider the presence of aberrations and other imaging artifacts. Ideally, any detrimental effects caused by the presence of aberrations would be corrected for through recovery of the generalized pupil function within the recovery algorithm. However, this may not always be the case. Considering point-imaging aberrations, one should ensure that they are not too severe, in which case they may hinder the convergence of the FP algorithm, as was observed when imaging through the window with the infinity corrected 10X lens. Further, the presence of aberrations affecting the image shape, such as field curvature and distortion, should be avoided, as it has not been investigated whether the recovered pupil can correct for these aberrations. In terms of other imaging effects, the presence of stray light caused by internal reflections within the microscope and intensity variations across the FoV should be avoided. In this project, the amount of internal reflections were reduced through the insertion of a non-reflecting inlay. However, stray-light was still observed at large illumination angles, limiting the number of LEDs which could be used without introducing substantial noise. For the latter, the presence of intensity fluctuations across the FoV was particularly noticeable for the compact 2X objective, as may be observed on close inspection of Figure 8.1.4. While not covered in this thesis, these intensity fluctuations were observed to cause artifacts in the recovered phase, though only for regions where no other intensity information was present, such as between the larger features of the USAF target.

Finally, a low numerical aperture objective should be chosen for the purposes of performing FP recovery through a window. Based on the results in chapter 10, both the compact 2X and telecentric 3X objectives were minimally affected by the window. As these objectives have numerical apertures of respectively 0.06 and 0.09, microscope objectives of comparable numerical aperture values should be viable. Conversely, a numerical aperture value of 0.28, as for the 10X infinity corrected objective, appears to be too large. While the aberrations are additionally dependent on the thickness and refractive index of the window, the maximal viable numerical aperture for a given window may be assumed to be on the lower side. Importantly, the ability of FP to achieve high-resolution imaging despite the use of a low numerical aperture lens, provides a solution to this issue. This is an additional benefit provided by FP as an imaging

method not covered in prior works. In addition to the possibility of imaging into a container which motivated this investigation, this may also be a beneficial property for the application of FP to biological systems where glass cover slips are often used.

11.3 Model improvements and further verification

To further the theoretical understanding of the intensity imaging process upon which FP is based, future works may investigate the effects of moving away from the paraxial approximation and whether the derived model accounts for varying degrees of telecentricity. Additionally, the relation between the axial location of the Entrance Pupil (EnP) and the effective object to AS distance should be considered further. Finally, to further validate the generalized imaging model derived in this thesis, it would be of interest to use a larger FoV camera to recover a region farther from the optical axis. In this case, the benefits from calculating the off-axis frequency shift based on the calibrated effective objective to AS distance would be emphasized.

Considering the effects of leaving the paraxial approximation, three directions of inquiry may be considered in future works. The first direction would be to consider whether it is feasible to avoid making the Fresnel-approximation when describing the propagation between the different planes of the imaging system. This could potentially be done through application of the angular spectrum method[8, p.83-84]. The second direction would be to consider the differences between the frequency shift for off-axis regions as calculated by Zheng and as found in this work for an object telecentric system within the paraxial approximation. Finally, the third direction would be to consider the implications of the Abbe sine condition, which states that a compound lens should be designed such that its principal planes are curved, rather than plane[53].

Concerning telecentricity, the ray optical visualizations of imaging systems considered in subsection 2.2.9 suggest that the imaging systems may yield varying changes in magnification for a sample placed outside of the object plane. This may mainly be observed based on the varying angles of the chief rays. As this angle is directly related to the AS placement, through the effective object to AS distance, it would be interesting to investigate how the quadratic phase and a defocus aberration in conjunction impacts the centers and shapes of on- and off-axis object points. Notably, the preceding project[7] performed simulations of the dot array sample, which demonstrated the existence of the proposed interaction between pupil aberrations and a quadratic phase at the object plane. However, this line of inquiry was not pursued further in this thesis due to time constraints. As such, future works may consider a quantitative investigation on this topic.

REFERENCES

[1] Guoan Zheng, Roarke Horstmeyer, and Changhuei Yang. "Wide-field, high-resolution Fourier ptychographic microscopy". In: *Nature photonics* 7.9 (2013), pp. 739–745.

[2] Xiaoze Ou, Guoan Zheng, and Changhuei Yang. "Embedded pupil function recovery for Fourier ptychographic microscopy". In: *Optics express* 22.5 (2014), pp. 4960–4972.

[3] Guoan Zheng et al. "Concept, implementations and applications of Fourier ptychography". In: *Nature Reviews Physics* 3.3 (2021), pp. 207–223.

[4] Pavan Chandra Konda. "Multi-Aperture Fourier Ptychographic Microscopy: Development of a high-speed gigapixel coherent computational microscope". PhD thesis. University of Glasgow, 2018.

[5] Tomas Aidukas, Lars Loetgering, and Andrew R Harvey. "Addressing phase-curvature in Fourier ptychography". In: *Optics Express* 30.13 (2022). This work is licensed under the Creative Commons Attribution 4.0 International license. To view a copy of this license, visit `https://creativecommons.org/licenses/by/4.0/`. DOI: `10.1364/OE.458657`.

[6] Mojde Hasanzade, Dag Werner Breiby, and Muhammad Nadeem Akram. "Wide field-of-view Fourier Ptychography microscopy based on Fresnel propagation scheme". In: *Results in Optics* 8 (2022), p. 100259.

[7] Erlend Hektoen Johansen. *Examining the effects of objective lens choice for Fourier Ptychography (project thesis at NTNU)*. May be obtained from the author or supervisor Dag W. Breiby upon reasonable request. 2024.

[8] Joseph W Goodman. *Introduction to Fourier optics*. eng. 4th ed. W. H. Freeman, 2017. ISBN: 978-1319119164.

[9] Masahiro Watanabe and Shree K Nayar. "Telecentric optics for focus analysis". In: *IEEE Transactions on Pattern Analysis and Machine Intelligence* 19.12 (1997), pp. 1360–1365.

[10] Max Born and Emil Wolf. *Principles of optics: electromagnetic theory of propagation, interference and diffraction of light*. eng. 6th ed. (with corrections). Pergamon Press, 1983. ISBN: 0-08-026482-4.

[11] Jack D Gaskill. *Linear systems, Fourier transforms, and optics*. Vol. 56. John Wiley & Sons, 1978.

[12] Jerome Mertz. *Introduction to optical microscopy*. Cambridge University Press, 2019.

[13] Xiaoze Ou et al. "High numerical aperture Fourier ptychography: principle, implementation and characterization". In: *Optics express* 23.3 (2015), pp. 3472–3491.

[14] An Pan et al. "System calibration method for Fourier ptychographic microscopy". In: *Journal of biomedical optics* 22.9 (2017), pp. 096005–096005.

[15] Christoph Greb. "Infinity Optical Systems: From infinity optics to the infinity port". In: *Optik & Photonik* 11.1 (2016), pp. 34–37.

[16] Joseph M Geary. *Introduction to lens design: with practical ZEMAX examples*. Willmann-Bell Richmond, 2002.

[17] Guoan Zheng. *Fourier ptychographic imaging: a MATLAB tutorial*. Morgan & Claypool Publishers, 2016.

[18] Jiasong Sun et al. "Efficient positional misalignment correction method for Fourier ptychographic microscopy". In: *Biomedical optics express* 7.4 (2016), pp. 1336–1350.

[19] Zichao Bian, Siyuan Dong, and Guoan Zheng. "Adaptive system correction for robust Fourier ptychographic imaging". In: *Optics express* 21.26 (2013), pp. 32400–32410.

[20] Kaikai Guo et al. "Optimization of sampling pattern and the design of Fourier ptychographic illuminator". In: *Optics express* 23.5 (2015), pp. 6171–6180.

[21] Lei Tian et al. "Multiplexed coded illumination for Fourier Ptychography with an LED array microscope". In: *Biomedical optics express* 5.7 (2014), pp. 2376–2389.

[22] Li-Hao Yeh et al. "Experimental robustness of Fourier ptychography phase retrieval algorithms". In: *Optics express* 23.26 (2015), pp. 33214–33240.

[23] John M Rodenburg and Helen ML Faulkner. "A phase retrieval algorithm for shifting illumination". In: *Applied physics letters* 85.20 (2004), pp. 4795–4797.

[24] Chao Zuo, Jiasong Sun, and Qian Chen. "Adaptive step-size strategy for noise-robust Fourier ptychographic microscopy". In: *Optics express* 24.18 (2016), pp. 20724–20744.

[25] Regina Eckert, Zachary F Phillips, and Laura Waller. "Efficient illumination angle self-calibration in Fourier ptychography". In: *Applied optics* 57.19 (2018), pp. 5434–5442.

[26] Ao Zhou et al. "Fast and robust misalignment correction of Fourier ptychographic microscopy for full field of view reconstruction". In: *Optics express* 26.18 (2018), pp. 23661–23674.

[27] Jizhou Zhang et al. “Precise brightfield localization alignment for Fourier ptychographic microscopy”. In: *IEEE Photonics Journal* 10.1 (2017), pp. 1–13.

[28] Yan Zhang et al. “Data preprocessing methods for robust Fourier ptychographic microscopy”. In: *Optical Engineering* 56.12 (2017), pp. 123107–123107.

[29] An Pan et al. “Vignetting effect in Fourier ptychographic microscopy”. In: *Optics and Lasers in Engineering* 120 (2019), pp. 40–48.

[30] Lexin Hou et al. “Background-noise reduction for Fourier ptychographic microscopy based on an improved thresholding method”. In: *Current Optics and Photonics* 2.2 (2018), pp. 165–171.

[31] Siyuan Dong et al. “Sparsely sampled Fourier ptychography”. In: *Optics express* 22.5 (2014), pp. 5455–5464.

[32] Yao Fan et al. “Adaptive denoising method for Fourier ptychographic microscopy”. In: *Optics Communications* 404 (2017), pp. 23–31.

[33] Walter Thompson Welford. *Aberrations of optical systems*. Adam Hilger Ltd, 1986.

[34] James C Wyant and Katherine Creath. “Basic wavefront aberration theory for optical metrology”. In: *Applied optics and optical engineering* 11.part 2 (1992), pp. 28–39.

[35] Pengming Song et al. “Full-field Fourier ptychography (FFP): Spatially varying pupil modeling and its application for rapid field-dependent aberration metrology”. In: *APL Photonics* 4.5 (2019).

[36] Kuo Niu and Chao Tian. “Zernike polynomials and their applications”. In: *Journal of Optics* (2022). This work is licensed under the Creative Commons Attribution 4.0 International license. To view a copy of this license, visit `https://creativecommons.org/licenses/by/4.0/`. DOI: `10.1088/2040-8986/ac9e08`.

[37] IDS Imaging. *U3-31J0CP-M-GL Rev.2.2*. URL: `https://en.ids-imaging.com/store/u3-31j0cp-rev-2-2.html` (visited on 04/28/2024).

[38] Lei Tian and Laura Waller. “3D intensity and phase imaging from light field measurements in an LED array microscope”. In: *optica* 2.2 (2015), pp. 104–111.

[39] Knut-Olav Schnell. “Fourier ptychography for computationally enhanced imaging in two and three dimensions”. MA thesis. Norwegian Universtity of Science and Technology, 2019.

[40] Edmund Optics. *2X Mitutoyo Compact Objective*. URL: `https://www.edmundoptics.com/p/2x-mitutoyo-compact-objective/13957/` (visited on 04/28/2024).

[41] Edmund Optics. *3X Mitutoyo Telecentric Objective*. URL: `https://www.edmundoptics.com/p/3x-mitutoyo-telecentric-objective/13947/` (visited on 04/28/2024).

[42] Edmund Optics. *10X Mitutoyo Plan Apo Infinity Corrected Long WD Objective*. URL: `https://www.edmundoptics.com/p/10x-mitutoyo-plan-apo-infinity-corrected-long-wd-objective/6623/` (visited on 04/28/2024).

[43] Fujinon. *Fujinon HF1618-12M*. URL: `https://www.fujifilm.com/us/en/business/optical-devices/machine-vision-lens/hf-12m-series#model02` (visited on 04/28/2024).

[44] Edmund Optics. *25.4mm Dia., 5mm Thick, VIS-NIR AR Coated Sapphire Window*. URL: https://www.edmundoptics.com/p/254mm-dia-5mm-thick-vis-nir-ar-coated-sapphire-window/51035/ (visited on 04/28/2024).

[45] Edmund Optics. *2" x 2" Positive, USAF 1951 Hi-Resolution Target*. URL: https://www.edmundoptics.com/p/2-x-2-positive-1951-usaf-hi-resolution-target/15108/ (visited on 04/28/2024).

[46] Edmund Optics. *25 x 25mm, 0.125mm Spacing, Glass Distortion Target*. URL: https://www.edmundoptics.com/p/25-x-25mm-0125mm-spacing-glass-distortion-target/15362/ (visited on 04/28/2024).

[47] Itzhauk Baum. *USAF-1951*. This work is licensed under the Creative Commons Attribution-Share Alike 3.0 Unported license. To view a copy of this license, visit https://creativecommons.org/licenses/by-sa/3.0/deed.en. URL: https://en.m.wikipedia.org/wiki/File:USAF-1951.svg (visited on 11/20/2023).

[48] Guido Van Rossum and Fred L. Drake. *Python 3 Reference Manual*. Scotts Valley, CA: CreateSpace, 2009. ISBN: 1441412697.

[49] Charles R. Harris et al. "Array programming with NumPy". In: *Nature* 585 (2020), pp. 357–362. DOI: 10.1038/s41586-020-2649-2.

[50] Pauli Virtanen et al. "SciPy 1.0: Fundamental Algorithms for Scientific Computing in Python". In: *Nature Methods* 17 (2020), pp. 261–272. DOI: 10.1038/s41592-019-0686-2.

[51] Siu Kwan Lam, Antoine Pitrou, and Stanley Seibert. "Numba: A llvm-based python jit compiler". In: *Proceedings of the Second Workshop on the LLVM Compiler Infrastructure in HPC*. 2015, pp. 1–6.

[52] Stefan Van der Walt et al. "scikit-image: image processing in Python". In: *PeerJ* 2 (2014), e453.

[53] Masud Mansuripur. "Abbe's sine condition". In: *Optics and Photonics News* 9.2 (1998), pp. 56–60.

[54] Frits Zernike. "Diffraction theory of the knife-edge test and its improved form, the phase-contrast method". In: *Monthly Notices of the Royal Astronomical Society, Vol. 94, p. 377-384* 94 (1934), pp. 377–384.

[55] Virendra N Mahajan. "Zernike circle polynomials and optical aberrations of systems with circular pupils". In: *Applied optics* 33.34 (1994), pp. 8121–8124.

APPENDICES

APPENDIX A

GITHUB REPOSITORY

The following link leads to a GitHub repository containing the code developed throughout this thesis and the preceding project[7].

`https://github.com/erlenhjo/pyFPM`

APPENDIX B

PROPAGATION THROUGH A SINGLE-LENS SYSTEM BY MEANS OF A SINGLE FOURIER TRANSFORM

For the derivations performed in this thesis, it is necessary to establish how a field at a plane in front of a lens may be related to a field at a plane behind the lens by means of only a single Fourier transform. To solve this problem, the propagation from the first plane to the lens, transmission through the lens and propagation from the lens to the second plane must be considered.

The system of interest is displayed in Figure B.0.1. The goal of the following derivation will be to relate the field U_F at a distance d_1 in front of the lens to the field U_B at a distance d_2 behind the lens. To this extent, it will additionally be helpful to define the complex wavefields U_{FL} and U_{BL} just in front and just behind the lens. To differentiate the focal length of the system considered here from focal lengths elsewhere in the thesis, it will be denoted by f'_L. Since either of the two free space propagation steps may be performed either by means of Equation 2.7 or Equation 2.8, being respectively the convolution and Fourier transform formulations of the Fresnel integral, there are four equally valid approaches to relate the two fields. However, only the approaches where each propagation equation is used only once will be considered, so that the final expression contains only a single Fourier transform. Additionally, the derivations will neglect the finite extent of the lens.

While the following derivation will pertain to a more general case, it is inspired by the derivations by Goodman[8, p.164-166] performed for the explicit system where $d_2 = f'_L$ and where the propagation steps are performed in order by means of respectively the convolution and Fourier transform formulations of the Fresnel integral.

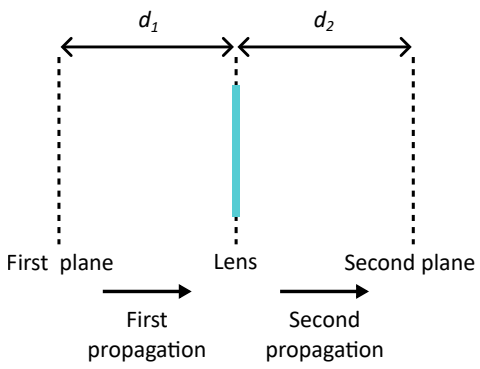

Figure B.0.1: The system of interest when evaluating propagation through a single-lens system by means of only a single Fourier transform. The field at the first plane may be related to the field at the second plane by means of free space propagation over a distance d_1, transmission through the lens and free space propagation over a distance d_2. For the fields to be related by a single Fourier transform, one of the two propagation steps must be calculated using the convolution formulation of the Fresnel integral, while the other must be calculated using the Fourier transform formulation.

B.1 Forward and inverse Fourier transform of the Fresnel integral convolution kernel

For the below derivations, it will be necessary to consider the Fourier transform and inverse Fourier transform of the kernel of the convolution formulation of Fresnel integral as defined by Equation 2.7. To reiterate Equation 2.7b, the convolution core is given as

$$h(x,y,z) = \frac{e^{ikz}}{i\lambda z}\exp\left\{\frac{ik}{2z}\left[x^2+y^2\right]\right\}. \tag{B.1}$$

In the following derivation, the Fourier transform is assumed to be evaluated at (f_u, f_v).

By means of the Fourier relation[8, p.17]

$$\mathcal{F}\left\{\exp[i\pi(a^2x^2+b^2y^2)]\right\} = \frac{1}{|ab|}\exp\left[-i\pi\left(\frac{f_u^2}{a^2}+\frac{f_v^2}{b_2}\right)\right] \tag{B.2}$$

the relation

$$\mathcal{F}\left\{h(x,y,z)\right\} = \mathcal{F}\left\{\frac{e^{ikz}}{i\lambda z}\exp\left[\frac{ik}{2z}\left[x^2+y^2\right]\right]\right\} = -ie^{ikz}\exp\left[-i\pi\lambda z\left(f_u^2+f_u^2\right)\right] \tag{B.3}$$

may be obtained by inserting $a^2 = b^2 = |ab| = 1/\lambda z$ and $k = 2\pi/\lambda$. Similarly, applying the duality property of the Fourier transform

$$\mathcal{F}\left\{g(\boldsymbol{r})\right\} = G(\boldsymbol{f}) \iff \mathcal{F}^{-1}\left\{g(\boldsymbol{f})\right\} = G(-\boldsymbol{r}) \tag{B.4}$$

yields the inverse Fourier transform of h as

$$\mathcal{F}^{-1}\left\{h(u,v,z)\right\} = \mathcal{F}^{-1}\left\{\frac{e^{ikz}}{i\lambda z}\exp\left[\frac{ik}{2z}\left[u^2+v^2\right]\right]\right\} = -ie^{ikz}\exp\left[-i\pi\lambda z\left(f_x^2+f_y^2\right)\right] \tag{B.5}$$

with (f_x, f_y) given by (f_u, f_v) evaluated at $(u,v) = (x,y)$

B.2 Convolution followed by Fourier transform

The subsequent derivation will consider the more general version of the system analyzed by Goodman[8, p.164-166], where the first propagation over a distance d_1 from the first plane to the lens is performed by means of the convolution formulation of the Fresnel integral, and the second propagation over a distance d_2 is performed by means of the Fourier transform formulation.

Using the convolution formulation of the Fresnel integral as given in Equation 2.7 and inserting the propagation distance d_1, the field just in front of the lens is given by

$$U_{FL}(x,y) = U_F(x,y) * h(x,y,d_1) \tag{B.6}$$

which after transmission through the lens becomes

$$U_{BL}(x,y) = [U_F(x,y) * h(x,y,d_1)] \cdot \exp\left[-\frac{ik}{2f'_L}\left(x^2+y^2\right)\right] \tag{B.7}$$

according to Equation 2.13. Relating the field just behind the lens to the field at the second plane by means of Equation 2.8 over a distance d_2 yields the relation

$$U_B(u,v) = \frac{e^{ikd_2}}{i\lambda d_2}\exp\left[\frac{ik}{2d_2}\left(u^2+v^2\right)\right]\mathcal{F}\left\{U_{BL}(x,y)\exp\left[\frac{ik}{2d_2}\left(x^2+y^2\right)\right]\right\} \tag{B.8}$$

with the Fourier transform evaluated at $(f_u, f_v) = (u/\lambda d_2, v/\lambda d_2)$. The complete relation then becomes

$$U_B(u,v) = \frac{e^{ikd_2}}{i\lambda d_2}\exp\left[\frac{ik}{2d_2}\left(u^2+v^2\right)\right]\cdot \mathcal{F}\left\{U_F(x,y) * h(x,y,d_1)\exp\left[\frac{ik}{2}\left(\frac{1}{d_2}-\frac{1}{f'_L}\right)\left(x^2+y^2\right)\right]\right\}, \tag{B.9}$$

which may be further simplified by removing the convolution by means of the convolution theorem and Equation B.3 according to

$$\mathcal{F}\{U * h\} = \mathcal{F}\{U\}\cdot\mathcal{F}\{h\} \tag{B.10}$$

with

$$U(x,y) = U_F(x,y)\exp\left[\frac{ik}{2}\left(\frac{1}{d_2}-\frac{1}{f'_L}\right)\left(x^2+y^2\right)\right], \tag{B.11a}$$

$$\mathcal{F}\{h\} = -ie^{ikd_1}\exp\left[-i\pi\lambda d_1\left(f_u^2+f_v^2\right)\right] = -ie^{ikd_1}\left[\frac{-ikd_1}{d_2^2}\left(u^2+v^2\right)\right] \tag{B.11b}$$

after evaluation of $\mathcal{F}\{h\}$ at $(f_u, f_v) = (u/\lambda d_2, u/\lambda d_2)$. Finally, combining the above equations and disregarding the constant prefactors yields the final equation

$$U_B(u,v) = \exp\left[\frac{ik}{2}\left(\frac{1}{d_2}-\frac{d_1}{d_2^2}\right)\left(u^2+v^2\right)\right]\cdot \mathcal{F}\left\{U_F(x,y)\exp\left[\frac{ik}{2}\left(\frac{1}{d_2}-\frac{1}{f'_L}\right)\left(x^2+y^2\right)\right]\right\} \tag{B.12}$$

where the Fourier transform is to be evaluated at $(f_u, f_v) = (u/\lambda d_2, u/\lambda d_2)$.

B.3 Fourier transform followed by convolution

For the alternative approach, the propagation over the distance d_1 from the first plane to the lens may be performed by means of the Fourier transform formulation of the Fresnel integral and the second propagation over the distance d_2 may be performed using the convolution formulation.

Performing the first propagation by means of Equation 2.8 yields the relation

$$U_{FL}(u,v) = \frac{e^{ikd_1}}{i\lambda d_1} \exp\left[\frac{ik}{2d_1}\left(u^2+v^2\right)\right] \mathcal{F}\left\{U_F(x,y)\exp\left[\frac{ik}{2d_1}\left(x^2+y^2\right)\right]\right\} \tag{B.13}$$

with the Fourier transform evaluated at $(f_u, f_v) = (u/\lambda d_1, v/\lambda d_1)$. Further, transmission through the lens by means of Equation 2.13 gives

$$U_{BL}(x,y) = U_{FL}(x,y)\exp\left[-\frac{ik}{2f'_L}\left(x^2+y^2\right)\right] \tag{B.14}$$

while the field at the second plane is obtained as

$$U_B(u,v) = U_{BL}(u,v) * h(u,v,d_2) \tag{B.15}$$

after propagation by means of the convolution formulation of the Fresnel integral. Combining the three above equations yields the complete relation

$$U_B(u,v) = \frac{e^{ikd_1}}{i\lambda d_1}\exp\left[\frac{ik}{2}\left(\frac{1}{d_1}-\frac{1}{f'_L}\right)\left(u^2+v^2\right)\right]\cdot \mathcal{F}\left\{U_F(x,y)\exp\left[\frac{ik}{2d_1}\left(x^2+y^2\right)\right]\right\} * h(u,v,d_2)\,, \tag{B.16}$$

at which point the convolution may be removed by means of the relation

$$\mathcal{F}\{U\} * h = \mathcal{F}\{U\} * \mathcal{F}\left\{\mathcal{F}^{-1}\{h\}\right\} = \mathcal{F}\left\{U\cdot\mathcal{F}^{-1}\{h\}\right\} \tag{B.17}$$

derived from the convolution theorem with

$$U(x,y) = U_F(x,y)\exp\left[\frac{ik}{2f'_L}\left(x^2+y^2\right)\right] \tag{B.18a}$$

$$\mathcal{F}^{-1}\{h\} = -ie^{ikd_2}\exp\left[-i\pi\lambda d_2\left(f_x^2+f_y^2\right)\right] = -ie^{ikd_2}\left[\frac{-ikd_2}{d_1^2}\left(x^2+y^2\right)\right] \tag{B.18b}$$

after evaluation of Equation B.5 at $(f_x, f_y) = (x/\lambda d_1, y/\lambda d_1)$. Disregarding the constant prefactors, the final equation then becomes

$$U_B(u,v) = \exp\left[\frac{ik}{2}\left(\frac{1}{d_1}-\frac{1}{f'_L}\right)\left(u^2+v^2\right)\right]\cdot \mathcal{F}\left\{U_F(x,y)\exp\left[\frac{ik}{2}\left(\frac{1}{d_1}-\frac{d_2}{d_1^2}\right)\left(x^2+y^2\right)\right]\right\} \tag{B.19}$$

where the Fourier transform is to be evaluated at $(f_u, f_v) = (u/\lambda d_1, u/\lambda d_1)$.

APPENDIX C

ZERNIKE POLYNOMIALS

The Zernike polynomials are a set of 2D polynomials that form an orthogonal basis over a unit disk. Since their introduction in 1934[54], they have seen use within the field of optics to describe the aberration function present in lens-based imaging systems[36, 55]. Notably, there exists a number of different indexing schemes[36]. To conform with the initial article introducing the Embedded Pupil Function Recovery (EPRY) algorithm[2] covered in section 3.4, the Noll indexation scheme will be considered. In this work, the Zernike polynomials will be applied to the phase of the generalized pupil function $kW(x, y)$ as defined in Equation 4.3.

In the Noll indexation scheme, the polynomials are primarily ordered with an index $j \in \mathbb{N}$ and are expressed in radial coordinates (ρ, θ) as[36]

$$Z_j(\rho,\theta) = Z_n^m(\rho,\theta) = \begin{cases} \sqrt{2(n+1)}R_n^m(\rho)\cos m\theta, & m \neq 0,\ j \text{ is even} \\ \sqrt{2(n+1)}R_n^m(\rho)\sin m\theta, & m \neq 0,\ j \text{ is odd} \\ \sqrt{n+1}R_n^m(\rho), & m = 0 \end{cases} \tag{C.1}$$

consisting of a normalization term, a radial term and an azimuthal term. The radial polynomials $R_n^m(\rho)$ are defined as

$$R_n^m(\rho) = \sum_{s=0}^{(n-m)/2} \frac{(-1)^s(n-s)!}{s!(\frac{n+m}{2}-s)!(\frac{n-m}{2}-s)!}\rho^{n-2s} \tag{C.2}$$

where the secondary indices n, representing the degree of the radial polynomials, and m, representing the azimuthal frequency, are derived from j according to the relations

$$n = \lfloor(\sqrt{2j-1}+1/2)-1\rfloor \tag{C.3a}$$

$$m = \begin{cases} 2\times\lfloor\frac{2j+1-n(n+1)}{4}\rfloor, & n \text{ is even} \\ 2\times\lfloor\frac{2j+2-n(n+1)}{4}\rfloor - 1, & n \text{ is odd.} \end{cases} \tag{C.3b}$$

For use with Cartesian coordinates (x, y) the transformations $x = \rho\cos\theta$ and $y = \rho\sin\theta$ may be applied.

Due to the Zernike polynomials forming an orthogonal basis over a unit disk, they allow for both synthesis and decomposition of any arbitrary aberration function normalized to be defined on a unit disk. Using the expansion coefficients a_j, synthesis and decomposition may be done using the respective relations

$$kW(\rho,\theta) = \sum_{j=1}^{\infty} a_j Z_j(\rho,\theta) \tag{C.4a}$$

$$a_j = \pi^{-1} \int_0^1 \int_0^{2\pi} kW(\rho,\theta) Z_j(\rho,\theta) \rho d\theta d\rho \,. \tag{C.4b}$$

Transformed to Cartesian coordinates, these relations become

$$kW(x,y) = \sum_{j=1}^{\infty} a_j Z_j(x,y) \tag{C.5a}$$

$$a_j = \pi^{-1} \iint\limits_{x^2+y^2\leq 1} kW(x,y) Z_j(x,y) dxdy \tag{C.5b}$$

assuming that the Zernike polynomials Z_j are written in their Cartesian forms. Further, one should note that the different terms of the Zernike polynomials can be related to classical aberrations such as tilt, defocus, astigmatism, coma and spherical aberrations[36, 55]. As such, the expansion coefficients a_j may be used to quantify the presence of specific aberration types. Moreover, within the Noll indexation scheme presented above, the squares of the expansion coefficients a_j^2 represents the contribution to the standard deviation of the aberration function from the j-th term starting from $j = 2$[55]. This yields a relation for the standard deviation of the the aberration function

$$\sigma_W^2 = \langle kW^2(\rho,\theta)\rangle - \langle kW(\rho,\theta)\rangle^2 = \langle kW^2(x,y)\rangle - \langle kW(x,y)\rangle^2 = \sum_{j=2}^{\infty} a_j^2. \tag{C.6}$$

Figure C.0.1 illustrates the first 36 Zernike polynomials in the Noll indexation scheme, while a list of the first 37 Zernike polynomials including indices j, n and m, their radial and Cartesian expressions as well as their related optical aberrations may be found in the work of Niu et al.[36, p.9].

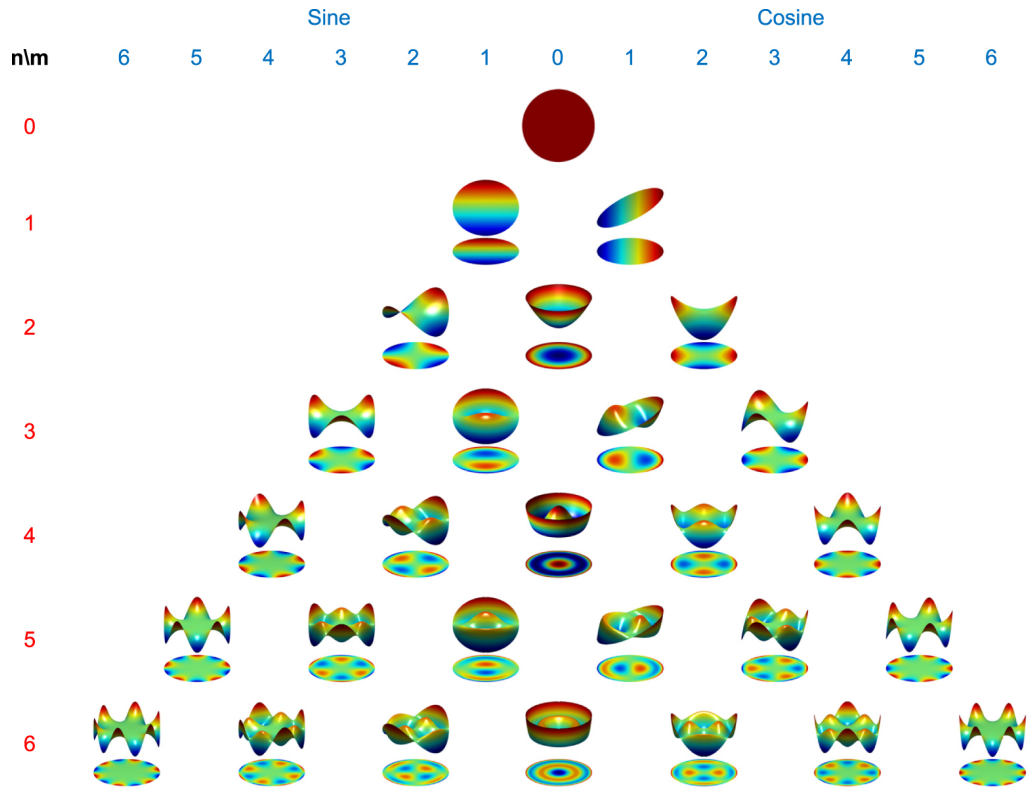

Figure C.0.1: Pyramid of the non-normalized Zernike circle polynomials up to the sixth degree under the Noll indexing scheme. Taken from [36], licensed under CC BY 4.0..

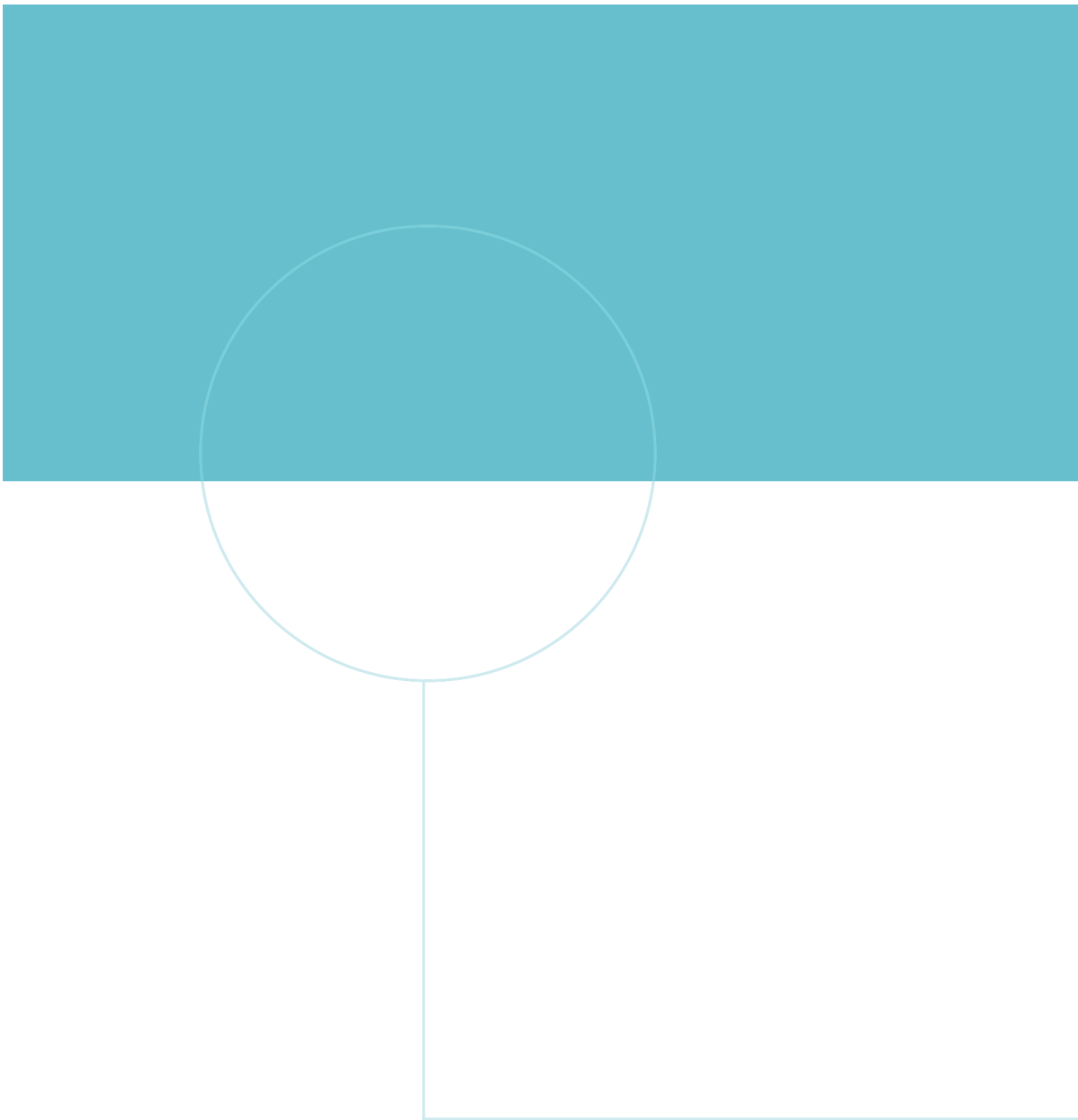

NTNU

Norwegian University of
Science and Technology